

Wireless Communications and Mobile Computing

Antenna Systems for Internet of Things

Lead Guest Editor: Hassan T. Chattha

Guest Editors: Qammer H. Abbasi, Masood Ur-Rahman, Akram Alomainy,
and Farooq A. Tahir





Antenna Systems for Internet of Things

Wireless Communications and Mobile Computing

Antenna Systems for Internet of Things

Lead Guest Editor: Hassan T. Chattha

Guest Editors: Qammer H. Abbasi, Masood Ur-Rahman,
Akram Alomainy, and Farooq A. Tahir



Copyright © 2018 Hindawi. All rights reserved.

This is a special issue published in “Wireless Communications and Mobile Computing.” All articles are open access articles distributed under the Creative Commons Attribution License, which permits unrestricted use, distribution, and reproduction in any medium, provided the original work is properly cited.

Editorial Board

- Javier Aguiar, Spain
Wessam Ajib, Canada
Muhammad Alam, China
Eva Antonino-Daviu, Spain
Shlomi Arnon, Israel
Leyre Azpilicueta, Mexico
Paolo Barsocchi, Italy
Alessandro Bazzi, Italy
Zdenek Becvar, Czech Republic
Francesco Benedetto, Italy
Olivier Berder, France
Ana M. Bernardos, Spain
Mauro Biagi, Italy
Dario Bruneo, Italy
Jun Cai, Canada
Zhipeng Cai, USA
Claudia Campolo, Italy
Gerardo Canfora, Italy
Rolando Carrasco, UK
Vicente Casares-Giner, Spain
Luis Castedo, Spain
Ioannis Chatzigiannakis, Greece
Lin Chen, France
Yu Chen, USA
Hui Cheng, UK
Ernestina Cianca, Italy
Riccardo Colella, Italy
Mario Collotta, Italy
Massimo Condoluci, Sweden
Bernard Cousin, France
Telmo Reis Cunha, Portugal
Igor Curcio, Finland
Laurie Cuthbert, Macau
Donatella Darsena, Italy
Pham Tien Dat, Japan
André de Almeida, Brazil
Antonio De Domenico, France
Antonio de la Oliva, Spain
Gianluca De Marco, Italy
Luca De Nardis, Italy
Liang Dong, USA
Mohammed El-Hajjar, UK
Oscar Esparza, Spain
Maria Fazio, Italy
- Mauro Femminella, Italy
Manuel Fernandez-Veiga, Spain
Gianluigi Ferrari, Italy
Ilario Filippini, Italy
Jesus Fontecha, Spain
Luca Foschini, Italy
A. G. Fragkiadakis, Greece
Sabrina Gaito, Italy
Óscar García, Spain
Manuel García Sánchez, Spain
L. J. García Villalba, Spain
José A. García-Naya, Spain
Miguel Garcia-Pineda, Spain
A.-J. García-Sánchez, Spain
Piedad Garrido, Spain
Vincent Gauthier, France
Carlo Giannelli, Italy
Carles Gomez, Spain
Juan A. Gomez-Pulido, Spain
Ke Guan, China
Antonio Guerrieri, Italy
Daojing He, China
Paul Honeine, France
Sergio Ilarri, Spain
Antonio Jara, Switzerland
Xiaohong Jiang, Japan
Minho Jo, Republic of Korea
Shigeru Kashiara, Japan
Dimitrios Katsaros, Greece
Minseok Kim, Japan
Mario Kolberg, UK
Nikos Komninos, UK
Juan A. L. Riquelme, Spain
Pavlos I. Lazaridis, UK
Tuan Anh Le, UK
Xianfu Lei, China
Hoa Le-Minh, UK
Jaime Lloret, Spain
Miguel López-Benítez, UK
Martín López-Nores, Spain
Javier D. S. Lorente, Spain
Tony T. Luo, Singapore
Maode Ma, Singapore
Imadeldin Mahgoub, USA
- Pietro Manzoni, Spain
Álvaro Marco, Spain
Gustavo Marfia, Italy
Francisco J. Martinez, Spain
Davide Mattera, Italy
Michael McGuire, Canada
Nathalie Mitton, France
Klaus Moessner, UK
Antonella Molinaro, Italy
Simone Morosi, Italy
Kumudu S. Munasinghe, Australia
Enrico Natalizio, France
Keivan Navaie, UK
Thomas Newe, Ireland
Wing Kwan Ng, Australia
Tuan M. Nguyen, Vietnam
Petros Nicopolitidis, Greece
Giovanni Pau, Italy
Rafael Pérez-Jiménez, Spain
Matteo Petracca, Italy
Nada Y. Philip, UK
Marco Picone, Italy
Daniele Pinchera, Italy
Giuseppe Piro, Italy
Vicent Pla, Spain
Javier Prieto, Spain
Rüdiger C. Prys, Germany
Junaid Qadir, Pakistan
Sujan Rajbhandari, UK
Rajib Rana, Australia
Luca Reggiani, Italy
Daniel G. Reina, Spain
Abusayeed Saifullah, USA
Jose Santa, Spain
Stefano Savazzi, Italy
Hans Schotten, Germany
Patrick Seeling, USA
Muhammad Z. Shakir, UK
Mohammad Shojafar, Italy
Giovanni Stea, Italy
Enrique Stevens-Navarro, Mexico
Zhou Su, Japan
Luis Suarez, Russia
Ville Syrjälä, Finland



Hwee Pink Tan, Singapore
Pierre-Martin Tardif, Canada
Mauro Tortonesi, Italy
Federico Tramarin, Italy
Reza Monir Vaghefi, USA

Juan F. Valenzuela-Valdés, Spain
Aline C. Viana, France
Enrico M. Vitucci, Italy
Honggang Wang, USA
Jie Yang, USA

Sherali Zeadally, USA
Jie Zhang, UK
Meiling Zhu, UK

Contents

Antenna Systems for Internet of Things

Hassan Tariq Chattha , Qammer H. Abbasi, Masood Ur-Rehman , Akram Alomainy, and Farooq A. Tahir 

Editorial (2 pages), Article ID 8691612, Volume 2018 (2018)

On the Capacity and Transmission Techniques of Massive MIMO Systems

Mohamed Abdul Haleem 

Research Article (9 pages), Article ID 9363515, Volume 2018 (2018)

Compact Ultra-Wide Band MIMO Antenna System for Lower 5G Bands

Haitham AL-Saif , Muhammad Usman , Muhammad Tajammal Chughtai, and Jamal Nasir 

Research Article (6 pages), Article ID 2396873, Volume 2018 (2018)

Tunable Platform Tolerant Antenna Design for RFID and IoT Applications Using Characteristic Mode Analysis

Abubakar Sharif , Jun Ouyang , Feng Yang, Rui Long, and Muhammad Kamran Ishfaq

Research Article (10 pages), Article ID 9546854, Volume 2018 (2018)

A Novel Dual Ultrawideband CPW-Fed Printed Antenna for Internet of Things (IoT) Applications

Qasim Awais, Hassan Tariq Chattha , Mohsin Jamil , Yang Jin, Farooq Ahmad Tahir , and Masood Ur Rehman 

Research Article (9 pages), Article ID 2179571, Volume 2018 (2018)

Effect of Randomness in Element Position on Performance of Communication Array Antennas in Internet of Things

Congsi Wang , Yan Wang , Xiaodong Yang , Wei Gao, Chao Jiang, Lu Wang, Yiqun Zhang, and Meng Wang 

Research Article (8 pages), Article ID 6492143, Volume 2018 (2018)

Position Tolerance Design Method for Array Antenna in Internet of Things

Congsi Wang , Shuai Yuan , Xiaodong Yang , Wei Gao, Cheng Zhu, Zhihai Wang, Shaoxi Wang , and Xuelin Peng

Research Article (6 pages), Article ID 7574041, Volume 2018 (2018)

Editorial

Antenna Systems for Internet of Things

Hassan Tariq Chattha ¹, **Qammer H. Abbasi**,² **Masood Ur-Rehman** ³,
Akram Alomainy,⁴ and **Farooq A. Tahir** ⁵

¹Department of Electrical Engineering, Faculty of Engineering, Islamic University of Madinah, Saudi Arabia

²School of Engineering, University of Glasgow, Glasgow G12 8QQ, UK

³School of Computer Science & Electronic Engineering, University of Essex, Wivenhoe Park, Colchester CO4 3SQ, UK

⁴School of Electronic Engineering and Computer Science, Queen Mary, University of London, London, E1 4NS, UK

⁵Research Institute for Microwave and Millimeter-Wave Studies, National University of Sciences and Technology (NUST), Islamabad, Pakistan

Correspondence should be addressed to Hassan Tariq Chattha; chattha43@hotmail.com

Received 2 September 2018; Accepted 2 September 2018; Published 17 September 2018

Copyright © 2018 Hassan Tariq Chattha et al. This is an open access article distributed under the Creative Commons Attribution License, which permits unrestricted use, distribution, and reproduction in any medium, provided the original work is properly cited.

Internet of Things (IoT) shall be imperative in incorporating different heterogeneous end systems including everything from smart homes to the industrial Internet of Things with smart agriculture, smart cities, and the smart grid. Apart from the sophisticated communication protocols, the choice of an antenna system will be a critical component of all these node end smart devices. Choosing the right antenna for an application imposes a key design challenge. As IoT modules continue to shrink incorporating more wireless technologies, making space for antennas is becoming an increasingly significant challenge. Thus, IoT-module antenna design faces the restrictions of ever-shrinking footprints while maintaining reasonable antenna performance under severe conditions such as noise, fading, and the need for efficiency. Enhanced techniques for multiplexing, interference mitigation, scheduling, and radio resource allocation work alongside the antenna design for the realization of efficient antenna systems for IoT.

The explosive growth of the Internet of Things and smart industrial applications creates many scientific and engineering challenges that are the main intentions of this special issue for ingenious research efforts for the development of efficient, cost-effective, scalable, and reliable antenna systems for IoT. The antenna designs for UWB and RFID tags in IoT enabled environment, MIMO antenna systems, transmission techniques of massive MIMO systems, and position tolerance design method and effects of randomness in element

positions in antenna arrays are given particular emphasis in the contributions included in this special issue.

Contributions. This special issue contains 6 scientific papers covering a range of antenna designs, techniques, and systems related to the Internet of Things.

In “A Novel Dual Ultrawideband Cpw-Fed Printed Antenna for Internet of Things (IoT) Applications” by Q. Awais et al., the authors present a printed antenna with coplanar waveguide (CPW) feeding having rectangular shaped blocks with dual-band characteristics. The antenna has compact dimensions of 35 mm × 25 mm with an FR4 used as substrate. For increasing the impedance bandwidth and gain of the antenna, a technique of rounded corners is exploited. The two ultrawidebands covered by the proposed antenna are 1.1 GHz to 2.7 GHz and 3.15 GHz to 3.65 GHz, which include 2.45 GHz Wi-Fi/Bluetooth, majority of the 3G, 4G bands, and a lower 6 GHz 5G band of 3.4 GHz to 3.6 GHz. The simulated results are compared with the measured ones which are generally in good accordance with each other. The antenna being low-profile is a suitable candidate for the 5G IoT portable applications.

In “Position Tolerance Design Method for Array Antenna in Internet of Things” by C. Wang et al., the authors discuss the position error of array antenna which is a significant factor of deteriorating the gain and sidelobe of the array, thus seriously affecting the performance of antenna array for

the Internet of Things (IoT). Using the sensitivity analysis theory, the authors derive the sensitivity of the array radiation field with respect to the position of the antenna element. The authors have also proposed a novel design method of position tolerance for array antenna and have applied it to a 20 x 20 planar array and have compared it with the antenna array designed by the traditional method. It is found that the gain loss of both of the antenna array is the same, i.e., 0.5 dB, whereas the peak side lobe level is lowered by 1.937 dB ($\phi = 0^\circ$)/1.586 dB ($\phi = 90^\circ$). In addition, the uncertainty analysis is also performed which has proved that the newly designed array has higher probability to obtain the required performance characteristics, which validates the new design method being innovative and effective.

In "On the Capacity and Transmission Techniques of Massive MIMO Systems," the author M. A. Haleem discusses the Massive-MIMO wireless system which is a multiuser system having base stations consisting of a large number of antenna elements with respect to the number of user devices with each equipped with a single antenna. The potential of the massive MIMO system is its ability to realize multiuser channels with near zero mutual coupling. In a high bit rate massive MIMO system with m base station antennas and n users, downlink capacity increases as $\log_2 m$ bps/Hz and the capacity per user decreases as $\log_2 n$ bps/Hz. This capacity can be obtained by power sharing using signal weighting vectors aligned with respective $1 \times m$ channels of the users. For a low bit-rate transmission, time sharing obtains the capacity equivalent to that of power sharing. If the channel coupling factor increases, the system capacity decreases. The probability distribution of channel coupling factor is a convenient tool to predict the number of antennas needed to qualify a system as Massive MIMO.

In "Tunable Platform Tolerant Antenna Design for RFID and IoT Applications Using Characteristic Mode Analysis" by A. Sharif et al., the authors highlight the significance of Radio Frequency Identification (RFID) as an emerging technology for sensing, identifying, tracking, and localizing different goods as being cost effective in tagging a large number of goods. The authors have proposed a platform tolerant RFID tag antenna having tuning capabilities. The Characteristic Mode Analysis (CMA) is used to design and optimize the proposed tag antenna. The proposed antenna contains a patch folded around an FR4 substrate and a loop as feeder printed on a paper substrate. Feeding loop is stacked over the folded patch thus providing impedance matching with different RFID chips. Having separate radiator and feeder, the proposed antenna exhibits the capability of getting its impedance matched with a variety of RFID chips. The frequency band covered by the proposed tag antenna is an American RFID band of 902-928 MHz and has the capability of being able to be tuned to the European RFID band of 865-868 MHz) using tunable strips. For the demonstration of platform tolerant operation, the RFID tag is mounted on different materials to measure its maximum read range, which is found to be 4.5 m in free space, on a dielectric, and a value of 6.5 m when placed above a 200 mm x 200 mm metal plate.

In "Compact Ultra-Wide Band MIMO Antenna System for Lower 5G Bands" by H. Al-Saif et al., the authors propose a

planar antenna with ultrawideband characteristics for MIMO applications. The presented antenna is simulated in the CST microwave studio and is designed to cover lower 5G bands from 2 to 12 GHz, thus covering the IEEE 802.11 a/b/g/n/ac as well. The proposed antenna has compact and miniaturized dimensions of 25 mm x 13 mm x 0.254 mm. The measured and simulated results are presented having good accordance with each other. The simulated and measured reflection coefficients S_{11} for the proposed design are below -10 dB over the frequency band in interest. The mutual coupling found between the two antennas is under -20 dB in desired frequency range. The 2D radiation patterns in E and H planes exhibit omnidirectional far fields with a peak measured gain of 4.8 dB. The fractional bandwidth of the proposed antenna is found to be around 143%, thus showing its ultrawideband characteristics.

In "Effect of Randomness in Element Position on Performance of Communication Array Antennas in Internet of Things" by C. Wang et al., the authors discuss the active phased array antennas, being a critical component of wireless communication, and face the restrictions of creating effective performance with the effect of randomness in the position of the array element, which are inevitably produced in the manufacturing and operating processes of the antenna. A new method for efficiently and effectively evaluating the statistic performance of the antenna is presented, with consideration of randomness in element position. A coupled structural-electromagnetic statistic model for array antenna is proposed from the viewpoint of electromechanical coupling. In addition, a 12 x 12 planar array is illustrated to evaluate the performance of the antenna with the saddle-shaped distortion and random position error. The results show that the presented model can obtain the antenna performance quickly and effectively, providing an advantageous guidance for structural design and performance optimization for array antennas in a wireless application.

These contributions bring a good insight of the present development activities and research happening related to antenna systems for the Internet of Things. The editors are optimistic that this special issue will contribute to the knowledge base and benefit the scientific community.

Conflicts of Interest

Authors have no conflicts of interest.

Acknowledgments

The editors would like to commend the contributions of the authors for making the special issue a success. Taking this opportunity, the editors would like to appreciate the efforts of the reviewers as well for the rigorous review process, thus enhancing the quality of the manuscripts submitted.

*Hassan Tariq Chattha
Qammer H. Abbasi
Masood Ur-Rehman
Akram Alomainy
Farooq A. Tahir*

Research Article

On the Capacity and Transmission Techniques of Massive MIMO Systems

Mohamed Abdul Haleem 

Department of Electrical Engineering, University of Hail, P.O. Box 2440, Hail 81451, Saudi Arabia

Correspondence should be addressed to Mohamed Abdul Haleem; haleems@gmail.com

Received 27 January 2018; Accepted 26 June 2018; Published 17 July 2018

Academic Editor: Masood Ur-Rahman

Copyright © 2018 Mohamed Abdul Haleem. This is an open access article distributed under the Creative Commons Attribution License, which permits unrestricted use, distribution, and reproduction in any medium, provided the original work is properly cited.

A massive MIMO wireless system is a multiuser MISO system where base stations consist of a large number of antennas with respect to number of user devices, each equipped with a single antenna. Massive MIMO is seen as the way forward in enhancing the transmission rate and user capacity in 5G wireless. The potential of massive MIMO system lies in the ability to almost always realize multiuser channels with near zero mutual coupling. Coupling factor reduces by 1/2 for each doubling of transmit antennas. In a high bit rate massive MIMO system with m base station antennas and n users, downlink capacity increases as $\log_2 m$ bps/Hz, and the capacity per user reduces as $\log_2 n$ bps/Hz. This capacity can be achieved by power sharing and using signal weighting vectors aligned to respective $1 \times m$ channels of the users. For low bit rate transmission, time sharing achieves the capacity as much as power sharing does. System capacity reduces as channel coupling factor increases. Interference avoidance or minimization strategies can be used to achieve the available capacity in such scenarios. Probability distribution of channel coupling factor is a convenient tool to predict the number of antennas needed to qualify a system as massive MIMO.

1. Introduction

Research and development activities in Multiple Input Multiple Output (MIMO) wireless systems originated more than two decades ago. Nevertheless, the potential of MIMO systems to enhance the capabilities of wireless mobile communication is still to be utilized. Initial research activities in MIMO wireless systems have been for point to point communication between transceivers equipped with comparable number of multiple antennas at both the transmitting and receiving ends. The origin of this work can be traced back to the application of the theory of random matrices in the information theory of mutually coupled random vectors [1, 2]. The term MIMO is first found in [3] where the authors derived the information capacity of certain MIMO channels with memory. The results from this work have been useful for solving the cross-talk problem in wired communication systems [4] and the cross coupling problem in wireless communications [5]. Consequently, the landmark papers on the information theory of matrix wireless channels appeared during 1990s [6, 7]. Coding methods to realize the capacity of

MIMO wireless channel also have been reported around this time period [8–10]. Published work on experimental MIMO wireless systems followed [11].

Since commercial wireless communication systems have been multiuser systems where typical user devices consist of one or two antennas, the subsequent attention has been on multiuser MIMO systems where base stations with multiple antennas serve user devices equipped with relatively fewer number of antennas. Although one can envision a system with full cooperation among base stations and user devices to form a single matrix channel in this context, theoretical and practical issues to be solved are immense and are not realistic for the state of the art in technology. It is difficult to solve issues related to channel estimation and feedback, synchronization, and precoding methods, to name a few. Somewhat simpler forms of multiuser MIMO systems were incorporated in 3G wireless standards where a base station allocates a few antennas per user and each user device comprises up to two antennas [12]. The design of such systems involves the consideration of mutual interference among different MIMO links within a cell site as well as the mutual

interference among links from different cell sites [13]. These methods are difficult to scale up as the system grows.

In recent years researchers and developers have been working on multiuser MIMO systems where the base stations have large excess of antennas relative to the numbers of users being served and each user device may have a single antenna. This particular form of MIMO system is known as massive MIMO or full-dimension MIMO system [14, 15]. Massive MIMO systems have several desirable properties. The statistical characteristics make it possible to almost always realize orthogonal or nearly orthogonal Multiple Input Single Output (MISO) channels. In this scenario, the intracell as well as intercell interferences of users become negligible. Thus, the system is scalable with ease as the operational user devices increase. Further, malfunctioning of a few antennas will not affect the performance since the serving antennas are a dynamic group (can be hot swapped) [16]. Many of the recent literature on massive MIMO focuses on implementation issues such as carrier synchronization [17] and pilot contamination [18]. Increased hardware complexity due to the requirement of an analog radio frequency (RF) chain for each antenna also has been a concern. Nevertheless, low cost implementation is possible as individual RF chains operate at significantly low power. The power per antenna reduces as inversely as the number of transmit antennas. The total transmit power increases only linearly as the number of user terminals being served. Recently published work such as [19] propose hybrid analog-digital techniques in the context of millimeter wave based massive MIMO systems. Massive MIMO systems are based on asymptotic results where the number of transmit antennas is considered large and optimal performance relies on the knowledge of channel covariance. Real-time estimation of such statistical parameters is difficult with large systems. Randomized algorithms have been studied for effective beamforming in massive MIMO systems as an alternative [20].

This paper presents a study on the achievable downlink capacity with ideally uncoupled (orthogonal) and partially coupled multiuser channels where there are multiple antennas at the base station and single antenna at user terminal. Optimal/suboptimal transmission vector design strategies to achieve the capacity are investigated. The analytical and simulation results are obtained for a single cell. It is assumed that the base station has complete knowledge of downlink channels of all users. In Section 2 to follow, expressions of Signal to Interference plus Noise Ratio (SINR) and transmission capacity are scrutinized to draw key conclusions on the trends when channel instantiations are uncoupled. This case characterises ideal massive MIMO system. It is shown that the selection of transmission vectors and multiple access techniques required to achieve the capacity in this case is trivial. Next, Section 3 addresses the necessary strategies when the channel instantiations are partially coupled. More elaborate transmission vector design methods are required to achieve the capacity in this case. Rate regions of optimal and suboptimal methods are studied and compared. Simulation results are presented to illustrate the trends in relative performances of different methods as the channel coupling factor varies. Illustrations exemplify how the performances of

various strategies converge to the performance of trivial case as the channels become uncoupled.

The coupling factors between channels of different users are random and good uncoupling is achieved only in the probabilistic sense. The probability distributions of coupling factor are examined in Section 4. The cumulative distributions of coupling factor are derived for varying number of base station antennas in this section. These curves are examined to draw important conclusions on the antenna requirements for a system to qualify as massive MIMO.

2. Transmission in Uncoupled Channels

In the system studied, there are m antennas at the base station serving n user devices each having a single antenna. Let the $1 \times m$ vector channels between the base station and the n users be $h_k, k = 1, 2, \dots, n$. Each of the m elements of h_k is the fading coefficient of the wireless channel between a transmit/receive antenna pair. The m elements in each of these vector channels can be modeled as uncorrelated zero mean circularly symmetric complex Gaussian random variables with unit variance [21, 22]. This model assumes a physical wireless environment rich in scatterers. The total available power P_{TOT} is distributed to the n users. It should be noted that P_{TOT} is the spatial average power available at a receiver when there is a single pair of transmit and receive antenna elements; i.e., the analytical framework accounts for path loss and shadow fading loss. The distribution of power among m transmit antennas for each user is determined by a weighting vector $W_k, k = 1, 2, \dots, n$. This vector can be represented in the normalized form, $W_k = \sqrt{P_k} w_k$, where P_k is the share of total power assigned to user k and w_k has unit norm, i.e., $\|w_k\| = 1$. The norm of a $1 \times m$ complex vector w_k here is $\|w_k\| = \sqrt{\sum_{l=1}^m |w_{kl}|^2}$, where $w_{kl}, l = 1, 2, \dots, m$ are the elements of w_k .

Received SINR at user k can be written as

$$\rho_k = \frac{|W_k \circ h_k|^2}{1 + \sum_{i \neq k}^n |W_i \circ h_k|^2} = \frac{P_k |w_k \circ h_k|^2}{1 + \sum_{i \neq k}^n P_i |w_i \circ h_k|^2}. \quad (1)$$

The notation \circ stands for the inner product defined as $x \circ y = x \bar{y}$, where x and y are row vectors of size $1 \times m$ and \bar{y} is the conjugate transpose of y . The notation $|\cdot|$ implies absolute value. In this expression, the numerator is the received signal power which results from the projection of the weighting vector onto the corresponding channel vector. The denominator is the interference plus noise at the receiver. The weighting vectors W_k are normalized to the noise voltages at the receiver. Therefore, P_k is normalized to noise power at the receive antenna and so is P_{TOT} . The maximum achievable bit rate (capacity) of user k in the information theoretic sense [23] is

$$R_k = \log_2 (1 + \rho_k) \quad (2)$$

and hence the maximum sum rate is

$$R_{TOT} = \sum_{k=1}^n \log_2 (1 + \rho_k). \quad (3)$$

Since the capacity R_k achieved by user k is a monotonically increasing function of ρ_k , maximization of ρ_k given by (1) maximizes R_k . Thus, it can be observed that the capacity of user k depends on the power allocations, the channels, and the weighting vectors of all n users. Power allocation and weighting vectors are under the control of signal processing algorithms, whereas the channels are decided by the propagation environment. If an instantiation of n vector channels $h_k, k = 1, \dots, n$ are mutually orthogonal (uncoupled), for a given power allocation $P_k, k = 1, \dots, n$, the weighting vectors $w_k, k = 1, \dots, n$ that are aligned to respective channels $h_k, k = 1, \dots, n$ i.e., $w_k = h_k / \|h_k\|$, maximize the numerator and null the interference term in the denominator (1), thus maximizing ρ_k and hence the transmission rate R_k . The rates achieved are the capacities of user channels for the allocated shares of power. On the other hand, it is possible to allocate the total power to each user for a fraction time frame in turn to implement time shared transmission. The capacities of time sharing and power sharing methods are further discussed in the subsections below.

2.1. Time Sharing. Let the base station sends data by sharing the time between n users and allocating total available power to a single user at a time. The user k achieves the rate R_k using a fraction λ_k of the time frame; thus, $\sum_{k=1}^n \lambda_k = 1$. From (1) and (2) the capacity achieved by user k with time sharing is $R_k = \lambda_k \log_2(1 + P_{TOT} \|h_k\|^2)$, or

$$R_k = \log_2(1 + P_{TOT} \|h_k\|^2)^{\lambda_k}. \quad (4)$$

Binomial expansion and omission of higher order terms with the assumption $P_{TOT} \|h_k\|^2 \ll 1$ results in the approximation:

$$R_k \approx \log_2(1 + \lambda_k P_{TOT} \|h_k\|^2) \quad (5)$$

and this is the rate achieved for low bit rate (low power) transmission. The results of (4) and (5) are independent of level of coupling between channels since transmission takes place for one user at a time.

2.2. Power Sharing. For uncoupled channels $h_i \circ h_k = 0$ for $i \neq k$ and the optimum weighting vectors are those in alignment with respective channels, i.e., $w_k = h_k / \|h_k\|$. From (1) and (2), these vectors lead to the capacity:

$$R_k = \log_2(1 + P_k \|h_k\|^2). \quad (6)$$

Comparison of (5) and (6) reveals that, at low bit rate transmission, the rate achieved by the user k via time sharing with a fraction λ_k of the time frame converges to the capacity of the system achievable by simultaneous transmission to all users in the entire time frame with shares of power $\lambda_k P_{TOT}$. This is an elegant and useful result showing the possibility of achieving capacity with simple time sharing, for low bit rate transmission.

Figure 1 illustrates this fact for an example case. This figure compares rate regions with time sharing and power

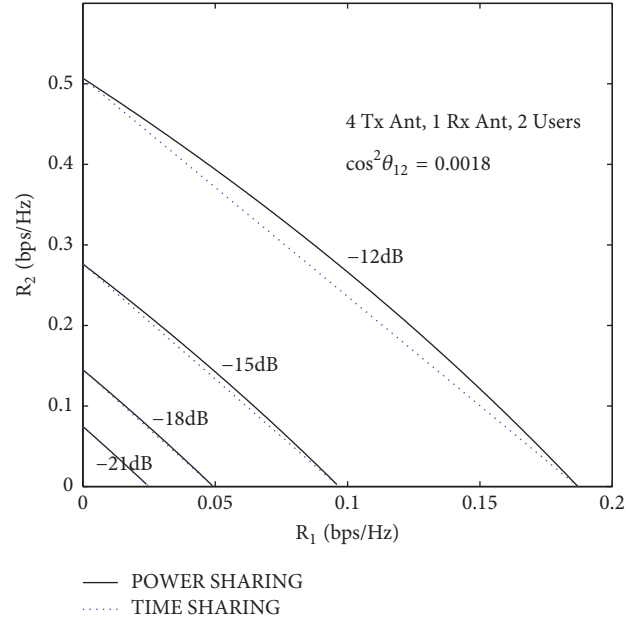


FIGURE 1: Rate regions with time sharing and power sharing at low bit rates (low power) transmission.

sharing for two users ($n = 2$) at total power levels ranging from -21dB to -12dB in steps of 3dB. These results have been obtained for the case of four base station antennas ($m = 4$) and $\cos^2 \theta_{12} = |h_i \circ h_k|^2 / \|h_i\|^2 \|h_k\|^2 = 0.0018$. Here $\cos_{12} \theta$ is the normalized coupling factor of the two channels. While the number of antennas used in this illustration may not qualify as “massive”, the pair of channels were selected by repeatedly generating channel instantiations from zero mean circularly symmetric Gaussian distribution of variance one until the coupling level was significantly small. For high bit rate (high power) transmissions, following results are obtained. Let in (6) $P_k \|h_k\|^2 \gg 1$. For sufficiently large number of base station antennas m , $\|h_k\|^2 \approx m$. Assuming equal power shares for n users (6) reduces to

$$\begin{aligned} R_k &\approx \log_2(P_k \|h_k\|^2) \approx \log_2\left(\frac{m P_{TOT}}{n}\right) \\ &= \log_2 P_{TOT} + \log_2 m - \log_2 n. \end{aligned} \quad (7)$$

Two observations are made here. First the achievable capacity of a user reduces by 1bps/Hz for each doubling of the number of users n . Second the capacity increases by 1bps/Hz for each doubling of the number of base station antennas m .

Figure 2 exemplifies these results. The curves in the figure have been obtained with $m = 4$ and $m = 16$ for a range of power settings in steps of 1dB. With $m = 4$ the power levels are in the range from 20dB to 30dB, whereas with $m = 16$ a range of 14dB to 24dB has been used. The 6dB difference has been kept so as to compensate for the factor of 4 in the number of antennas m . Channel instantiations are selected so as to have negligibly small values for coupling factor $\cos \theta_{12}$. The two sets of curves for different values of m do not coincide in this case since the number of antennas are not sufficient to satisfy the condition $\|h_k\|^2 \approx m$. It can

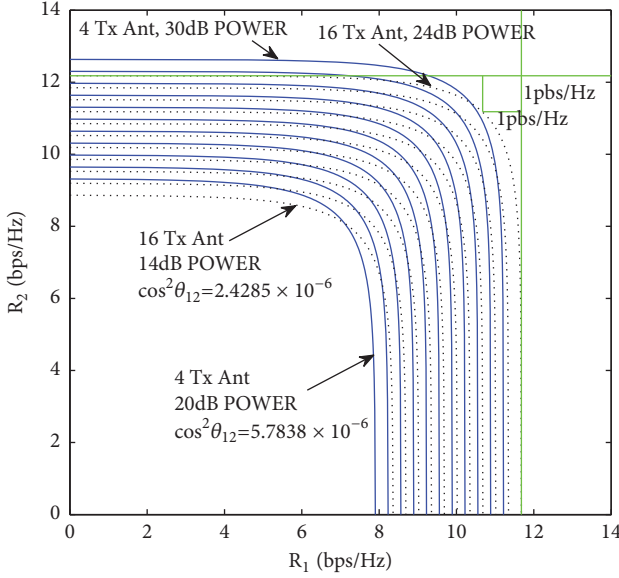


FIGURE 2: Rate regions with power sharing for high bit rate (high power) transmission. Illustration of antenna-power trade-off.

be observed that the optimal pair of rates are 1bps/Hz below that achievable by allocating total available power to a single user. It is worthwhile to mention here that in a massive MIMO system comprised of a large excess of base station antennas compared to the number of users, the $\log_2 n$ term in (7) can be neglected and the capacity of any user becomes independent of the total number of users.

This section has focused on transmission in uncoupled multiuser channel instantiations. In a massive MIMO system, most of the channel instantiations are mutually uncoupled. Nevertheless, there exists a finite probability however small, for the channels to have significant level of coupling. This probability increases as the number of active users increase with respect to the number of base station antennas. Thus, a close look at the cases of coupled channels is necessary. In this case, simple alignment of weighting vectors to respective channels is suboptimal. Alternative strategies such as zero forcing, best linear optimization, and Dirty Paper Coding are considered to achieve better performance. Section 3 presents the optimal weighting vector design techniques for coupled channels.

3. Transmission in Coupled Channels

Maximization of transmission rate implies maximization of SINR. To this end, methods such as Lagrangian based best linear optimization (BLO) and Zero Forcing (ZF) are studied and compared with Dirty Paper Coding (DPC). DPC is known to be optimal for the scenario in concern ([24] and references therein). Relative performances of these techniques are studied considering two users each equipped with a single antenna and m transmit antennas at the base station.

In the discussion to follow, the two $1 \times m$ vector channels are denoted by g and h . The primary optimization problem

here is to maximize the sum capacity of two users for the available channel instantiations as the fractions of total power P_{TOT} assigned to two users varies. The solution can be obtained by first evaluating the surface of minimum total power required to achieve pairs of rates in the $R_h - R_g$ rate plane. The intersection of the surface of minimum total power and the plane at P_{TOT} parallel to $R_h - R_g$ plane gives the curve of achievable capacities for the available total power.

3.1. Best Linear Optimization(BLO). For two users with channels g and h , the SINR expression of (1) reduces to

$$\rho_g = \frac{P_g |\omega_g \circ g|^2}{1 + P_h |\omega_h \circ g|^2}, \quad (8)$$

$$\rho_h = \frac{P_h |\omega_h \circ h|^2}{1 + P_g |\omega_g \circ h|^2}$$

and the total power is $P_{TOT}^{BL} = |W_g|^2 + |W_h|^2 = P_g + P_h$. The optimum weighting vectors and power values can be found by solving the Lagrange optimization problem given by

$$\begin{aligned} [W_g, W_h] = \arg \min_{\{W_g, W_h\}} & \left\{ \|W_g\|^2 + \|W_h\|^2 \right. \\ & + \lambda_g \left[|W_g \circ g|^2 - \rho_g (1 + |W_h \circ g|^2) \right] \\ & \left. + \lambda_h \left[|W_h \circ h|^2 - \rho_h (1 + |W_g \circ h|^2) \right] \right\} \end{aligned} \quad (9)$$

The objective function given by this equation is minimum when the partial derivatives with respect to the conjugate transposes \bar{w}_g and \bar{w}_h become zero. The optimum Lagrange multipliers λ_g and λ_h are the solutions to the set of hyperbolic equations (10) and (11).

$$s \lambda_g \lambda_h + a \sqrt{s} \lambda_h - bc \sqrt{s} \lambda_g - b = 0 \quad (10)$$

$$s \lambda_g \lambda_h + c \sqrt{s} \lambda_g - ad \sqrt{s} \lambda_h - d = 0. \quad (11)$$

In these equations, $s = \|g\|^2 \|h\|^2 - |g \circ h|^2$ (Schwartz's identity), $a = \|h\|^2 / \sqrt{s}$, $b = 1/\rho_h$, $c = \|g\|^2 / \sqrt{s}$, and $d = 1/\rho_g$. The solution is two valued and one of the solutions leads to a feasible set of power levels. Accordingly, the minimum total power is achieved for the weighting vectors given by

$$\omega_g = \frac{\left((1 - \lambda_h \rho_h \|h\|^2) g + \lambda_h \rho_h (g \circ h) h \right)}{\left(\|g\|^2 + s \lambda_h \rho_h (\lambda_h \rho_h \|h\|^2 - 2) \right)^{1/2}} \quad (12)$$

and

$$\omega_h = \frac{\left((1 - \lambda_g \rho_g \|g\|^2) h + \lambda_g \rho_g (h \circ g) g \right)}{\left(\|h\|^2 + s \lambda_g \rho_g (\lambda_g \rho_g \|g\|^2 - 2) \right)^{1/2}} \quad (13)$$

Thus, the minimum power P_g is given by (14). The expression for power P_h can be easily written by replacing each parameter in the numerator by its dual, i.e., g by h , h by g , etc. Hence, the total minimum power to achieve the pair of rates (R_g, R_h) is given by (15).

$$P_g = \frac{\left((\|g\|^2 - \lambda_h \rho_h s)^2 + |g \circ h|^2 \rho_g \right) (\|h\|^2 + s \lambda_g \rho_g (\lambda_g \rho_g \|g\|^2 - 2)) \rho_h}{(\|g\|^2 - \lambda_h \rho_h s)^2 (\|h\|^2 - \lambda_g \rho_g s)^2 - |h \circ g|^4 \rho_g \rho_h} \quad (14)$$

$$P_{TOT}^{BL} = \frac{\left\{ \begin{array}{l} [(\|h\|^2 - s \lambda_g \rho_g)^2 + |g \circ h|^2 \rho_h] [\|g\|^2 + s \lambda_h \rho_h (\lambda_h \rho_h \|h\|^2 - 2)] \rho_g \\ + [|g \circ h|^2 \rho_g + (\|g\|^2 - s \lambda_h \rho_h)^2] [\|h\|^2 + s \lambda_g \rho_g (\lambda_g \rho_g \|g\|^2 - 2)] \rho_h \end{array} \right\}}{(\|g\|^2 - s \lambda_h \rho_h)^2 (\|h\|^2 - s \lambda_g \rho_g)^2 - |g \circ h|^4 \rho_g \rho_h} \quad (15)$$

3.2. *Dirty Paper Coding (DPC)*. In the BLO of Section 3.1, the transmission to the two users mutually interferes. It is possible to eliminate interference to one of the users by making the other user ‘phantom’ via precoding techniques [25], Dirty Paper Coding (DPC) [26] in particular. Assume that the user of channel h is made phantom by precoding the symbol transmitted to privileged user with channel g with respect to the symbol transmitted to phantom user of channel h . The privileged user of channel g does not experience interference from the phantom user of channel h and hence (8) reduces to

$$\begin{aligned} \rho_g &= P_g |\omega_g \circ g|^2, \\ \rho_h &= \frac{P_h |\omega_h \circ h|^2}{(1 + P_g |\omega_g \circ h|^2)}. \end{aligned} \quad (16)$$

The phantom user of channel h experiences interference from privileged user of channel g . If the power available to phantom user is significantly large compared to the power available to privileged user, then the interference experienced by the phantom user will not significantly degrade the SINR, ρ_h . With such a precoding, the choice of weighting vector ω_h of the phantom user has no effect on the privileged user. Thus, ω_h can be selected to maximize phantom user’s rate. The choice $\omega_h = h/\|h\|$ achieves maximum rate. In this context, there is a freedom of choice for the weighting vector ω_g . It can be computed based on one of three different criteria leading to *polite*, *aggressive*, and *objective* versions of DPC discussed below.

3.2.1. *Polite DPC*. In this approach, the privileged user’s weighting vector is selected such that the interference to phantom user is avoided. The term ‘polite’ emphasizes the fact that the privileged user utilizing precoding to achieve interference free reception from the phantom user chooses the weighting vector to eliminate the interference to the phantom user by zero forcing i.e., by choosing ω_g such that $\omega_g \circ h = 0$. Gram-Schmidt ortho-normalization [27] provides $\omega_g = (1/\|g\| \sin \theta)(g - (g \circ h)(h/\|h\|^2))$, where $\cos \theta = |g \circ h|/\|g\|\|h\|$ is the channel coupling factor. Thus, total power is

$$P_{TOT}^{PDPC} = \frac{2^{R_g} - 1}{\|g\|^2 \sin^2 \theta} + \frac{2^{R_h} - 1}{\|h\|^2}. \quad (17)$$

3.2.2. *Aggressive DPC*. The rate of privileged user can be maximized by aligning the weighting vector to the channel i.e., with $\omega_g = g/\|g\|$ and this approach is dubbed *aggressive* DPC. Here the privileged user achieves the best possible rate leaving the phantom user to achieve the best rate with interference. The total power in aggressive DPC is

$$\begin{aligned} P_{TOT}^{ADPC} &= \frac{2^{R_g} - 1}{\|g\|^2} + \frac{2^{R_h} - 1}{\|h\|^2} \\ &+ \frac{(2^{R_g} - 1)(2^{R_h} - 1)}{\|g\|^2} \cos^2 \theta \end{aligned} \quad (18)$$

3.2.3. *Objective DPC*. In the objective mode of DPC, the weighting vectors are selected to maximize the sum rate for the available total power. The choice of weighting vector of the phantom user is similar to the previous two forms of DPC, i.e., $\omega_h = h/\|h\|$. The choice of weighting vector ω_g of the privileged user is so that to minimize the total power required to achieve the specified pair of rates. The power minimization process is as follows. Substitution of $\omega_h = h/\|h\|$ in (16) leads to $P_{TOT} = P_g + P_h = \rho_g/|\omega_g \circ g|^2 + (\rho_h/\|h\|^2)(1 + \rho_g(|\omega_g \circ h|^2/|\omega_g \circ g|^2))$. Algebraic manipulations lead to $P_{TOT} = \rho_h/\|h\|^2 + \rho_g(|\xi|^2/\xi Q^{-1/2} \bar{g} g Q^{-1/2} \bar{\xi})$, where $Q = I + \rho_h(\bar{h}h/\|h\|^2)$ and $\xi = \omega_g Q^{1/2}$. Minimization of P_{TOT} amounts to maximization of $\Delta = \xi Q^{-1/2} \bar{g} g Q^{-1/2} \bar{\xi}/|\xi|^2$ and is achieved with $\xi = g Q^{-1/2}$. Hence, the optimal weighting vector is $\omega_g = g Q^{-1}$ and the corresponding $\Delta = g Q^{-1} \bar{g}$. It can be shown that $Q^{-1} = I - \rho_h \bar{h}h/\|h\|^2(1 + \rho_h)$. Thus, the total power is

$$P_{TOT}^{ODPC} = \frac{(2^{R_h} - 1)}{\|h\|^2} + \frac{(2^{R_g} - 1)}{\|g\|^2} \frac{2^{R_h}}{1 + (2^{R_h} - 1) \sin^2 \theta} \quad (19)$$

It can be observed that if the channels g and h are mutually orthogonal, i.e., $\sin \theta = 1$, the total power requirements for all three cases of (17)–(19) reduce to (20). This also is the minimum total power to achieve the pair of rates in the case of uncoupled channels discussed in Section 2.

$$P_{TOT}^{UC} = \frac{2^{R_g} - 1}{\|h_g\|^2} + \frac{2^{R_h} - 1}{\|h_h\|^2} \quad (20)$$

On the other extreme when channels g and h are highly coupled, $\sin \theta \rightarrow 0$ and $\cos \theta \rightarrow 1$. Total power

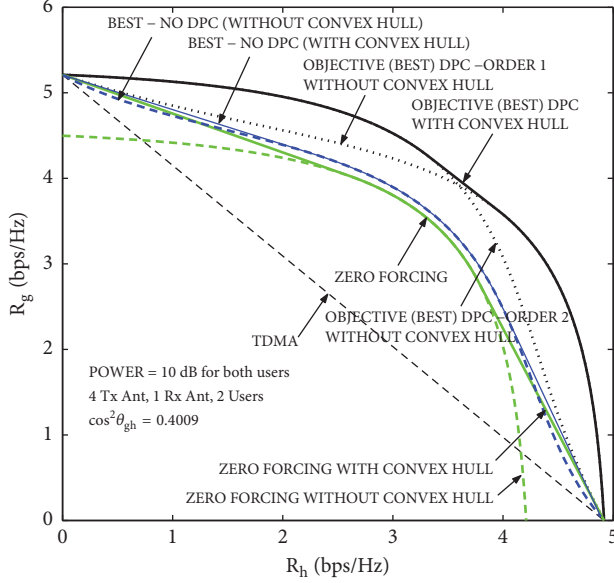


FIGURE 3: Comparison of rate regions with significantly high channel coupling.

requirement for Polite DPC of (17) grows without bound in this case deeming it an unsuitable strategy. However, the total power expressions of aggressive DPC of (18) and Objective DPC of (19) converge to a unique form given by

$$P_{TOT}^{ODPC} = \frac{(2^{R_g} - 1)}{\|g\|^2} + \frac{2^{R_h} (2^{R_h} - 1)}{\|h\|^2} \quad (21)$$

3.3. Zero Forcing Beam Forming. The approach here is to null out mutual interferences to both users. Graham Schmidt orthogonalization process leads to $\omega_g = (1/\|g\| \sin \theta)(g - (g \circ h)(h/\|h\|^2))$ and $\omega_h = (1/\|h\| \sin \theta)(h - (h \circ g)(g/\|g\|^2))$. Total power requirement for such a zero forcing approach becomes

$$P_{TOT}^{ZF} = \frac{1}{\sin^2 \theta} \left(\frac{(2^{R_h} - 1)}{\|h\|^2} + \frac{(2^{R_g} - 1)}{\|g\|^2} \right) \quad (22)$$

When g and h are mutually orthogonal, (22) reduces to (20) as in the case of uncoupled channel discussed in Section 2. This convergence is similar to that of DPC in all three forms. However, for highly coupled channels, i.e., when $\sin \theta = 0$, the total power required to achieve any given rate pair grows without bound as with Polite DPC.

Figure 3 shows a comparison of achievable rate regions with transmission techniques discussed above when the channels g and h are coupled, i.e., $\cos \theta \gg 0$. Rate region of time sharing is included in this figure (labeled TDMA) as a reference.

As can be observed in this figure, DPC (objective type) achieves the best rate region. Curve labeled DPC-order 1 is the rate region when the user with channel h is made phantom. This order provides better performance when power available to user with channel h is relatively larger compared to that of user with channel g . The curve obtained with alternative

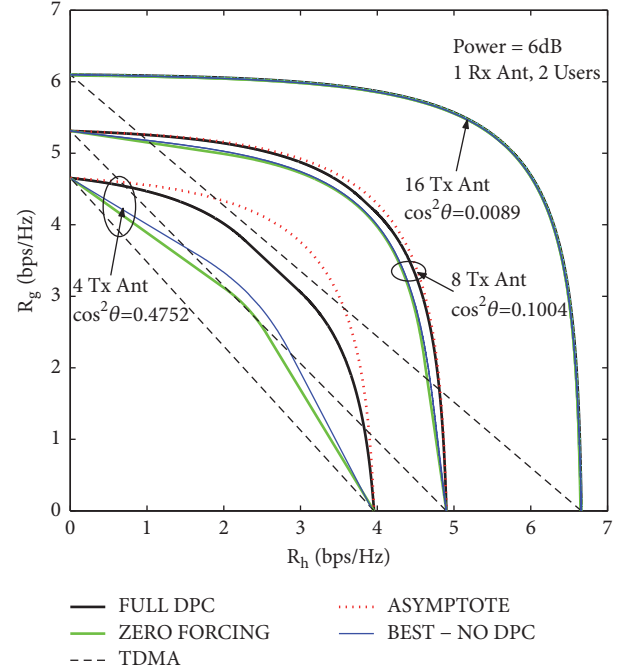


FIGURE 4: Convergence of rate regions as coupling factor is reduced.

order (DPC-order 2) performs better when the power available to user with channel g increases beyond certain share of total power. Further, there is a range of power sharing, in which adherence to only one order of DPC is not optimal. In this range, optimal sum rate is achieved by time sharing between two specific optimal powers sharing, each with the corresponding optimal DPC order. The solid curve labeled “DPC with Convex Hull” shows the combined optimal rate region achieved by switching between two DPC orders as well by including time sharing whenever appropriate.

BLO (labeled best no DPC) results in the second best performance. It is seen that there are two ranges of power sharing; when the asymmetry in power levels of two users is high, time sharing between single user transmission and an optimal power shared simultaneous transmission is better than BLO alone. ZF yields the third best performance. Here too, time sharing is beneficial to achieve better performance. Convex hulls of optimal rate regions are included for BLO and ZF.

Figure 4 illustrates the trends in the rate regions of objective DPC (labeled full DPC), BLO (labeled best, no DPC), and ZF as the coupling level between channels g and h reduces. The three sets of curves have been obtained, respectively, for number of base station antennas $m = 4, 8$ and 16. Nevertheless, the convergence depends only on the coupling factor $\cos \theta$ as concluded from (17)–(22). As the value of $\cos^2 \theta$ changes from 0.4752 to 0.1004, the rate regions of different weighting vector design strategies get closer to each other. At a value of 0.0089, the rate regions converge to one and the same region. At such a level of coupling, transmitting using simple power sharing without paying attention to mutual interference would perform as good as any other method, if it is a high bit rate transmission. For

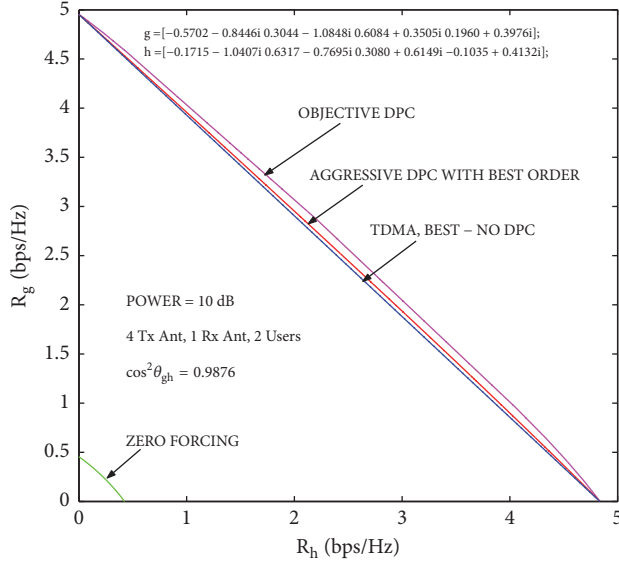


FIGURE 5: Rate regions with high channel coupling.

low bit transmission, simple time shared transmission is sufficient to achieve rates close to capacity, as discussed in Section 2.

Figure 5 exemplifies the performance trends of objective DPC, aggressive DPC, ZF, and time sharing (labeled TDMA) in highly coupled channels, i.e., $\cos \theta \rightarrow 1$. Since the power level in this example is high, it corresponds to high bit rate transmission. It can be seen that the rate region of time sharing approaches DPC rate region. As can be concluded from this figure as well as (17) and (22), performances of DPC in polite mode and ZF become far inferior to all other approaches because $\sin \theta \rightarrow 0$ as channels become highly coupled leading to large minimum total power requirements to achieve any pair of rates.

Intuitively and as evident from the above example, time sharing is the best approach when channels are highly coupled regardless the power levels (transmission rates). Previously it was concluded in Section 2 that time sharing is the best approach for low bit rate (low power) transmissions in uncoupled channels.

4. Channel Coupling Statistics

In the previous sections, performances of time sharing, power sharing, and several interference minimization techniques were studied using instantiations of channels drawn from complex Gaussian probability distribution. The instantiations were selected with channel coupling factor ($\cos \theta$) values to represent low, medium, and high levels of channel coupling so that to investigate the relative performances of signal weighting vector design strategies for channels of different levels of coupling. In this juncture, it is important to explore the probability distribution of channel coupling factor in multiuser wireless channel for different number of antennas at base station. This provides insight on the requirements of massive MIMO system.

TABLE 1: 99% orthogonality level.

99% ile coupling factor		
No. of Tx. Ant.	$10 \log_{10} \cos^2 \theta$	$\cos^2 \theta$
4	-1.01	0.7925
16	-5.55	0.2786
64	-11.44	0.0718
256	-17.23	0.0189
1024	-23.31	0.0046

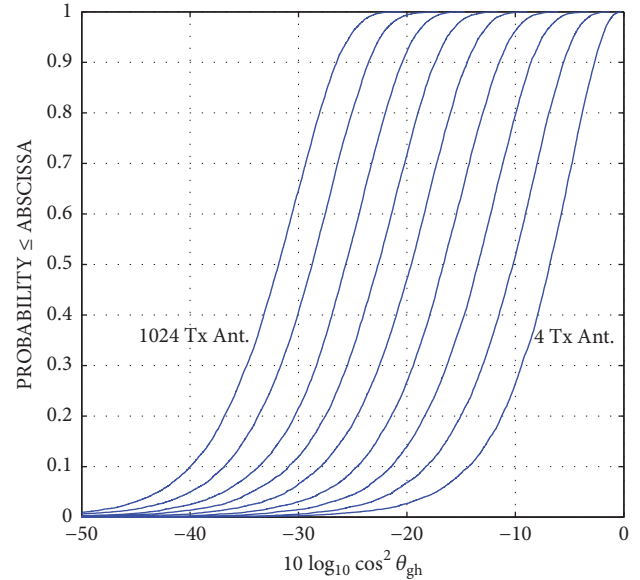
FIGURE 6: Cumulative distribution of $1 \times m$ channel orthogonality factor.

Figure 6 shows the cumulative distribution of $\cos \theta$ in dB scale. The set of curves has been obtained for number of base station antennas from 4 to 1024, doubling the number of antennas each time. It is observed that, at any given cumulative probability in the range 0-1, the coupling factor reduces by approximately 3dB, i.e., the coupling factor halves, for each doubling of antennas. Table 1 summarizes the variation of 99% coupling factor for quadrupling of the number of antennas. Observing the results in this table and Figure 4, it can be concluded that number of base station antennas in the order of 256 may ensure sufficiently low coupling factors among pairs of channels for 99% of the channel realizations such that a multiuser transmission with simple power shared simultaneous transmission can achieve throughput close to capacity.

5. Conclusion

This paper presented key results on the downlink transmission capacity of massive MIMO wireless system in terms of the number of base station antennas and number of user devices. The capacity and the simplicity of transmission techniques in achieving the capacity are attributed to the ability of massive MIMO system to naturally uncouple

TABLE 2: Optimal transmission strategy.

Transmission Rate	Coupling Factor		
	Low	Medium	High
High	Power Sharing (Massive MIMO)	DPC BLO ZF	Time Sharing
Low	Time Sharing		

multiuser MISO channels. However, when in a multiuser MISO channel, the ratio of the number of base station antennas to number of users is not sufficiently large, channel instantiations with medium to high levels of coupling can occur with significant probability. In such scenarios, transmission vector can be optimized by selecting the best design technique to match the prevailing channel coupling level. In other words, a hybrid approach with flexibility to switch between several weighting vector design methods is useful. Interference minimization strategies are efficient in achieving the available capacity when the channel coupling factor is significantly large.

Table 2 summarizes signal vector design strategies appropriate for different channel coupling levels and transmission rates. For low bit rate transmission, time sharing with full power can achieve throughput close to system capacity, which is independent of the channel coupling level. However, the coupling factor plays a major role in deciding the capacity for high bit rate transmission. When coupling factor is high, time sharing is the best approach even for high bit rate transmission. When the coupling factor is not so high but not negligible, interference minimization or avoidance methods such as DPC, BLO, and ZF is necessary to achieve optimal performance. With negligibly small coupling factors, simple alignment of the signal transmission vector to respective channels of users is the best approach for high bit rate transmission. A massive MIMO system is one that can almost always realize channels with negligible channel coupling factors due to the excessive number of base station antennas compared to the number of users to be served. This ability simplifies many of the design and implementation tasks.

As highlighted in this paper, massive MIMO system increases the capacity and simplifies signal transmission vector design process to achieve throughput reaching the capacity. Massive MIMO system boasts many other merits which are not addressed in this paper. Examples are robustness, reliability, and use of low cost hardware. Among the challenges faced in realizing the full potential of massive MIMO are computational complexity, efficient distributed processing algorithms, and synchronization of the antenna units.

Data Availability

The studies and conclusions of this paper are supported by MATLAB simulation results and are included within the article.

Conflicts of Interest

The author declares that there are no conflicts of interest regarding the publication of this paper.

Acknowledgments

Author's research has been supported by the Deanship of Scientific Research, University of Hail, Saudi Arabia.

References

- [1] M. S. Pinsker, *Information and information stability of random variables and processes*, Translated and edited by Amiel Feinstein, Holden-Day, Inc., San Francisco, Calif.-London-Amsterdam, 1964.
- [2] R. Balian, "Random matrices in information theory," *Il Nuovo Cimento*, p. 183, 1968.
- [3] L. H. Brandenburg and A. D. Wyner, "Capacity of the Gaussian channel with memory: the multivariate case," *Bell Labs Technical Journal*, vol. 53, pp. 745–778, 1974.
- [4] H. S. Witsenhausen, "A determinant maximization problem occurring in the theory of data communication," *SIAM Journal on Applied Mathematics*, vol. 29, no. 3, pp. 515–522, 1975.
- [5] J. Salz, "Digital transmission over cross-coupled linear channels," *AT&T Technical Journal*, pp. 1147–1159, 1985.
- [6] G. J. Foschini and M. J. Gans, "On limits of wireless communications in a fading environment when using multiple antennas," *Wireless Personal Communications*, vol. 6, no. 3, pp. 311–335, 1998.
- [7] E. Telatar, "Capacity of multi-antenna Gaussian channels," *European Transactions on Telecommunications*, vol. 10, no. 6, pp. 585–595, 1999.
- [8] G. J. Foschini, "Layered space-time architecture for wireless communication in a fading environment when using multiple antennas," *Bell Labs Technical Journal*, vol. 1, no. 2, pp. 41–59, 1996.
- [9] S. M. Alamouti, "A simple transmit diversity technique for wireless communications," *IEEE Journal on Selected Areas in Communications*, vol. 16, no. 8, pp. 1451–1458, 1998.
- [10] G. G. Raleigh and J. M. Cioffi, "Spatio-temporal coding for wireless communication," *IEEE Transactions on Communications*, vol. 46, no. 3, pp. 357–366, 1998.
- [11] G. D. Golden, C. J. Foschini, R. A. Valenzuela, and P. W. Wolniansky, "Detection algorithm and initial laboratory results using V-BLAST space-time communication architecture," *IEEE Electronics Letters*, vol. 35, no. 1, pp. 14–15, 1999.
- [12] H. Huang, H. Viswanathan, A. Blanksby, and M. Haleem, "Multiple antenna enhancements for a high rate cdma packet data system," in *J. of very large scale integration (VLSI) signal processing*, vol. 30, pp. 55–69, Kluwer Academic Publishers, 2002.
- [13] E. G. Larsson, "MIMO detection methods: How they work," *IEEE Signal Process. Mag.*, vol. 26, no. 3, p. 91, May 2009.
- [14] T. L. Marzetta, "Noncooperative cellular wireless with unlimited numbers of base station antennas," *IEEE Transactions on Wireless Communications*, vol. 9, no. 11, pp. 3590–3600, 2010.
- [15] E. G. Larsson, O. Edfors, F. Tufvesson, and T. L. Marzetta, "Massive MIMO for next generation wireless systems," *IEEE Communications Magazine*, vol. 52, no. 2, pp. 186–195, 2014.

- [16] F. Rusek, D. Persson, B. K. Lau et al., “Scaling up MIMO: opportunities and challenges with very large arrays,” *IEEE Signal Processing Magazine*, vol. 30, no. 1, pp. 40–60, 2013.
- [17] D. J. Jorg, A. Pollakis, L. Wetzel et al., “Synchronization of mutually coupled digital PLLs in massive MIMO systems,” in *Proceedings of the 2015 IEEE International Conference on Signal Processing for Communications (ICC)*, pp. 1716–1721, London, June 2015.
- [18] A. S. Alwakeel, A. H. Mehana, and A. Ghoneim, “Pilot hopping in multi-cell massive MIMO systems: Pilot assignment and new results,” in *Proceedings of the 2017 International Conference on Computing, Networking and Communications, ICNC 2017*, pp. 460–464, USA, January 2017.
- [19] T. Kuehe and G. Caire, “An Analog Module for Hybrid Massive MIMO Testbeds Demonstrating Beam Alignment Algorithms,” in *Proceedings of the 22nd International ITG Workshop on Smart Antennas, WSA*, 2018.
- [20] M. N. Boroujerdi, S. Haghighatshoar, and G. Caire, “Low-complexity and Statistically Robust Beamformer Design for Massive MIMO Systems , 22nd International ITG Workshop on Smart Antennas,” in *Proceedings of the Low-complexity and Statistically Robust Beamformer Design for Massive MIMO Systems , 22nd International ITG Workshop on Smart Antennas*, 2018.
- [21] R. H. Clarke, “A statistical theory of mobile-radio reception,” *Bell Labs Technical Journal*, vol. 47, no. 6, pp. 957–1000, 1968.
- [22] W. C. Jakes, *Microwave Mobile Communications*, Wiley-IEEE Press, Piscataway, NJ, USA, 1994.
- [23] T. M. Cover and J. A. Thomas, *Elements of Information Theory*, John Wiley & Sons, 2012.
- [24] S. Luo, J. Xu, T. J. Lim, and R. Zhang, “Capacity region of MISO broadcast channel for simultaneous wireless information and power transfer,” *IEEE Transactions on Communications*, vol. 63, no. 10, pp. 3856–3868, 2015.
- [25] S. A. Jafar, G. J. Foschini, and A. J. Goldsmith, “PhantomNet: Exploring optimal multicellular multiple antenna systems,” *EURASIP Journal on Applied Signal Processing*, vol. 2004, no. 5, pp. 591–604, 2004.
- [26] M. H. M. Costa, “Writing on dirty paper,” *IEEE Transactions on Information Theory*, vol. 29, no. 3, pp. 439–441, 1983.
- [27] L. N. Trefethen and D. Bau, *Numerical Linear Algebra*, SIAM, Philadelphia, Pa, USA, 1997.

Research Article

Compact Ultra-Wide Band MIMO Antenna System for Lower 5G Bands

Haitham AL-Saif ¹, **Muhammad Usman** ¹,
Muhammad Tajammal Chughtai¹ and **Jamal Nasir** ²

¹Electrical Engineering Department, College of Engineering, University of Hail, Saudi Arabia

²Department of Electrical Engineering, COMSATS Institute of Information Technology, Abbottabad, KPK, Pakistan

Correspondence should be addressed to Muhammad Usman; m.usman@uoh.edu.sa

Received 1 February 2018; Revised 6 April 2018; Accepted 6 May 2018; Published 4 June 2018

Academic Editor: Hassan T. Chattha

Copyright © 2018 Haitham AL-Saif et al. This is an open access article distributed under the Creative Commons Attribution License, which permits unrestricted use, distribution, and reproduction in any medium, provided the original work is properly cited.

This paper presents a novel compact 2×2 planar MIMO antenna system with ultra-wide band capability. Antenna system is specifically designed to target lower 5th generation operating bands ranging from 2 GHz to 12 GHz. This band also covers the IEEE 802.11 a/b/g/n/ac. The antenna array geometry has been simulated using CST MWS. The design is extremely miniaturized with total structure size of $13 \times 25 \times 0.254$ mm³. The simulated and measured results have been presented. Measured and simulated return loss values for designed antenna are less than -10 dB over the operating band and lowest values of -35 dB and -32.5 dB can be seen at 5.2 GHz and 9.2 GHz, respectively, whereas at the center frequency the return loss is -25.2 dB. The mutual coupling between both elements is less than -20 dB over the transmission bandwidth. Simulated and measured radiation patterns in E and H planes at center frequency show nearly isotropic far fields. The maximum gain is measured as 4.8 dB. Promising results of Envelope Correlation Coefficient and gain diversity of the design have been achieved. Simulated and measured results are found in good agreement. The fractional bandwidth of antenna is measured as 143.2% which satisfies its ultra-wide band response.

1. Introduction

In the coming years, the global mobile data traffic is likely to be projected by 45%; this means a ten times increase between the years 2016 and 2022 [1]. This massive increase is mainly due to mobile video streaming and implementation of Internet of Things (IoT). This will result in approximately 18 billion IoT out of total 29 billion devices [2]. Due to this reason, the future 5th generation networks would need to overcome the demand of wider spectrum in high frequency range. The key constraint to implement and deploy 5G networks before 2020 is the availability of frequency spectrum; hence both the higher and lower frequency bands are needed for 5G.

Lower 5G bands are ideal for early deployment, due to their advantageous properties including wave propagation and available bandwidth. The main spectrum bands between 2 GHz and 6 GHz are in the ranges from 3.3 GHz to 4.2 GHz and from 4.4 GHz to 4.990 GHz. These bands are presently being considered for initial trials of 5G networks in a number

of countries. Table 1 illustrates the operative regions and their respective lower 5G bands [3].

In order to meet this challenge and according to the current demands, a novel ultra-wide band (UWB) 2×2 Multiple Input Multiple Output (MIMO) antenna system has been designed and simulated. This antenna system covers the frequency band ranging from 2 GHz to 12 GHz, which covers all the lower 5G frequency bands. Its array is an ideal candidate for 5G enabled, handheld devices including mobile phones and tablets. Furthermore, this band also satisfies operating regulations of the UWB according to Federal Communication Commission (FCC) [4]. Also, the designed antenna covers the IEEE 802.11 a/b/g/n/ac standards for Wi-Fi operation in mobile devices.

By Using the UWB technology, wireless communication devices can transmit over a very wide range of frequency band while consuming lower powers [4]. Also the UWB technology based devices have several other merits including high data-rates, increased bandwidth, and being low in cost

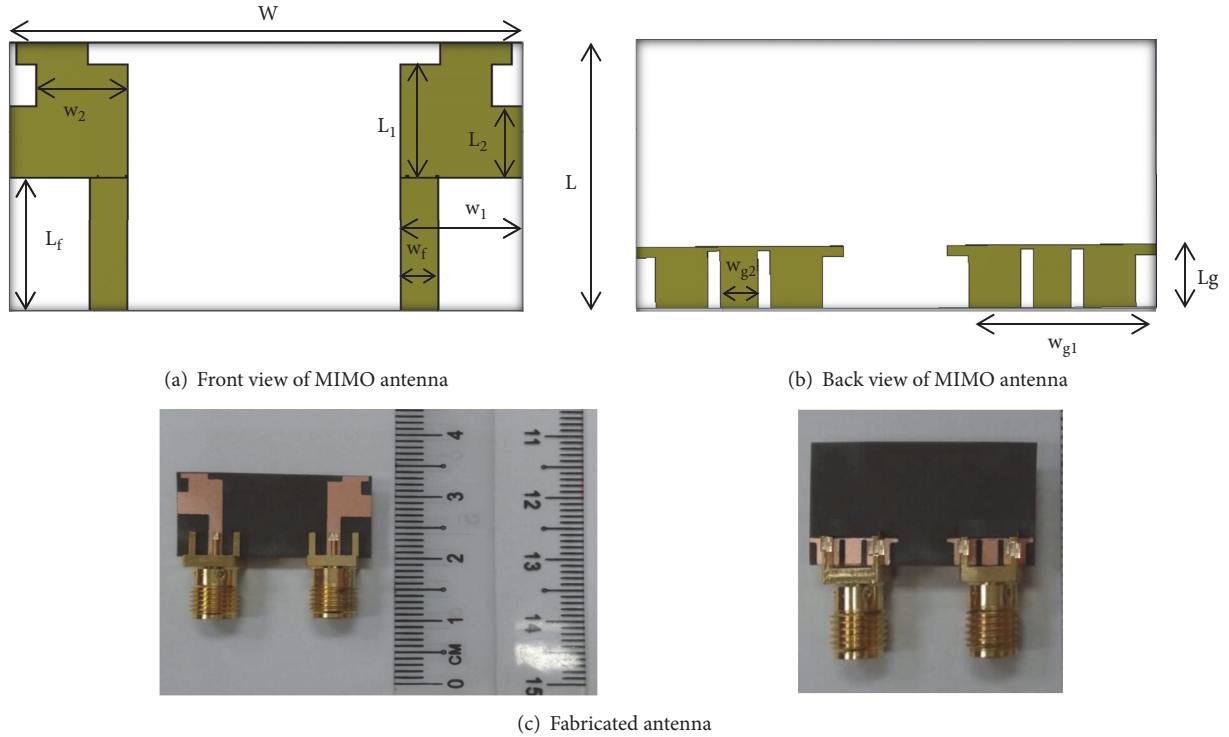


FIGURE 1

TABLE 1: Regions and lower 5G frequency bands.

Region	Frequency range (GHz)
Europe	3.4–3.8
China	3.4–3.8, 4.4–4.5, 4.8–4.99
Japan	3.6–4.2, 4.4–4.9
Korea	3.4–3.7
USA	3.1–3.55, 3.7–4.2

[5]. In the UWB communication devices, front-end antenna plays very important role. Thus, a lot of work and research [6] has been done to design the UWB antennas for mobile devices. Planar antennas are considered as promising solution for the UWB applications due to their simple design, lower cost, and performance [7].

MIMO antenna systems are vastly implemented in wireless devices to enhance the channel capacity and multipath propagation [8]. In recent times, the UWB and MIMO technologies have been integrated in wireless systems for enhanced performance in terms of high data-rates [9]. The main challenge in designing these kinds of antenna systems are to reduce the mutual coupling between the radiating elements within smaller volumes of small handheld devices. This can be achieved by polarization diversity or by increasing the space between the antennas [8]. Cross-polarized antenna geometries are usually complicated in design, whereas increasing the space between the antennas results in larger volumes [10]. For implementation of the UWB MIMO systems, some good methods are radiation pattern diversity, space diversity, and polarization diversity.

In this paper, space diversity is achieved by using two asymmetric “F” type structures with a very compact fractured ground plane [11].

2. Antenna Design Methodology and Configuration

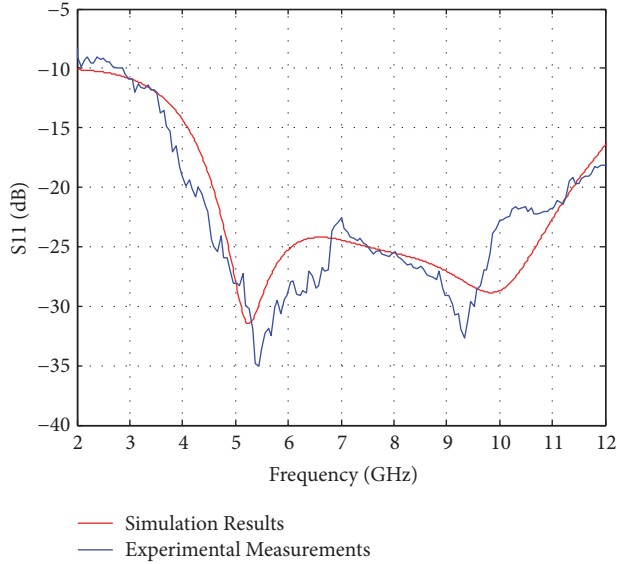
The designed antenna is an extremely compact 2×2 UWB MIMO antenna system. The antenna consists of two asymmetric “F” type structures with a very compact fractured ground plane. The overall volume of the antenna geometry is $25 \times 13 \times 0.254 \text{ mm}^3$. The proposed antenna system has been fabricated on Rogers substrate (5880) with relative permittivity, dielectric loss tangent, and height values of 2.2, 0.0009, and 0.254 mm, respectively. The front and rear views of the designed antenna system are shown in Figures 1(a), 1(b), and 1(c).

To start with a single antenna element which has been designed, a detailed parametric study has been done using CST microwave studio. The final values of all geometric variables are presented in Table 2.

The “F” shaped patched monopole design is selected due to its wide band characteristics and enhanced performance in S, C, and X bands [12–16]. The overall dimensions of the single F shaped patch have been optimized to achieve the UWB characteristics. In order to incorporate a 2×2 MIMO antenna array, a second F shaped patch has been reciprocated on the same plane. Both antenna ports are resonated at an input impedance of 50Ω . To reduce the coupling between the two radiating elements, a distance of 13.9 mm has been carefully

TABLE 2: Antenna design geometric variables.

Variables	L	W	H	W_f	L_f	W_1	W_2	W_3	W_{g1}	W_{g2}	L_g	L_1	L_2	L_s	W_s
Dimensions in mm	13	25	0.9	1.6	6.5	5.9	4.9	1.6	10	1.8	3	3.5	2	3	0.6

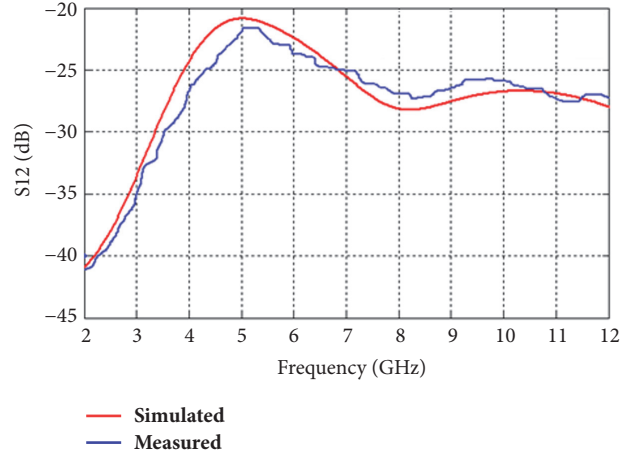
FIGURE 2: Simulated and measured reflection coefficients (S_{11} , S_{22}).

selected, where this value corresponds to a half wavelength at the upper frequency of operation. Furthermore, compact fractured ground plane has been incorporated; the size of the ground plane is very compact having dimensions of $10 \times 3 \text{ mm}^2$. Fractured ground plane helped in achieving the target port impedance at the resonant frequency band.

3. Results and Discussion

The presented ultra-wide band 2×2 coplanar MIMO array antenna comprised two “F” shaped monopoles. The geometry has been further modified to achieve the targeted bandwidth and reflection coefficient for 50Ω input port impedance. Both antenna elements exhibited identical reflection coefficients (S_{11} , S_{22}). The simulated and measured reflection coefficients are shown in Figure 2.

As it can be seen from Figure 2, the antenna geometry is resonant at wide range of frequency band starting from 2 GHz to 12 GHz. The lowest values of reflection coefficients are observed as -35 dB and -32.5 dB at 5.2 GHz and 9.2 GHz, respectively. The return loss is well under -10 dB for overall band, whereas at center frequency of 8 GHz the return loss has been measured as -25.2 dB . While designing MIMO antenna systems, the main effort achieved lower value of transmission coefficient between the ports and this is regarded as a key factor in design. It can be seen in Figure 3 that both monopoles are well decoupled; also the mutual coupling between both elements in operating band is well under -20 dB . In case of the operation of UWB, usually the

FIGURE 3: Simulated and measured transmission coefficient (S_{12}).

fractional bandwidth should remain above 50% [17], whereas for the antenna system under consideration the fractional bandwidth is measured as 143.2% which satisfies ultra-wide band operation.

The normalized graphs of simulated and measured radiation patterns for the designed antenna system are shown in Figure 4.

For both antenna elements, the radiation patterns are investigated in E and H planes at center frequency of 8 GHz. The center frequency has been selected to measure the radiation patterns at which the return loss is -25.2 dB . The measurement has been done by exciting each port at a time, while the other port is connected to a matched load of 50Ω . It can be observed in Figure 4 that both simulated and measured far fields are in agreement to each other. Also, both elements show near omnidirectional pattern. However, as it is a patch antenna, therefore, maximum diversity can be seen along z-axis. Furthermore, minor changes can be noticed in measured patterns that are due to the absorption errors inside the anechoic chamber. Still the results are very substantial.

Figure 5 shows the measured overall gain of the designed antenna system over the band of frequencies ranging from 2 to 12 GHz. A gain of 2.8 dB has been observed at center frequency.

The gain diversity (G_{app}) is considered as most important parameter in MIMO antenna system. This can be calculated by measuring the Envelope Correlation Coefficient (ECC) between the antenna elements of the MIMO system. There are two mechanisms for calculating the values of gain diversity, either using the S-parameters of the antenna elements or using the radiation patterns. In this paper, the gain diversity has been calculated using S-parameters of the ports. As an assumption, uniform multipath environment has been

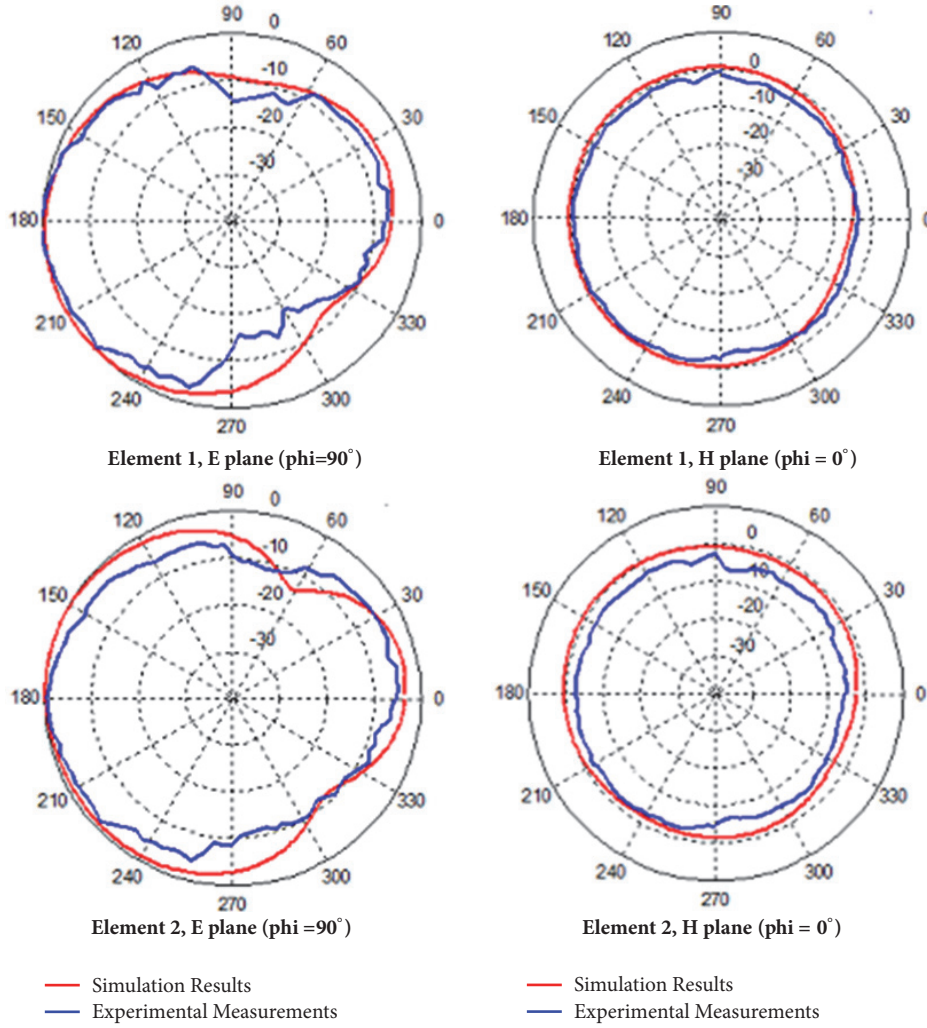


FIGURE 4: Simulated and measured radiation patterns.

considered, and the ECC and G_{app} can be calculated by using the equations given as [18, 19].

$$\text{ECC, } \rho_e = \frac{|S_{11}^* S_{12} + S_{21}^* S_{22}|^2}{(1 - (|S_{11}|^2 + |S_{21}|^2))(1 - (|S_{22}|^2 + |S_{12}|^2))} \quad (1)$$

$$G_{\text{app}} = 10\sqrt{1 - |\rho|}, \quad |\rho| = \rho_e$$

Figures 6 and 7 represent the measured and simulated results of ECC and gain diversity, respectively. The simulated and measured results for both parameters are very much comparable.

Ideally, the ECC of fully decoupled MIMO antenna system should be zero. As it can be seen from Figure 7, over most of the band the value remains zero. There are few variations present in the measured result at 2 GHz, 5 GHz, and 12 GHz; this is due to the reflections which are usually caused by the certain components that are present in the anechoic chamber.

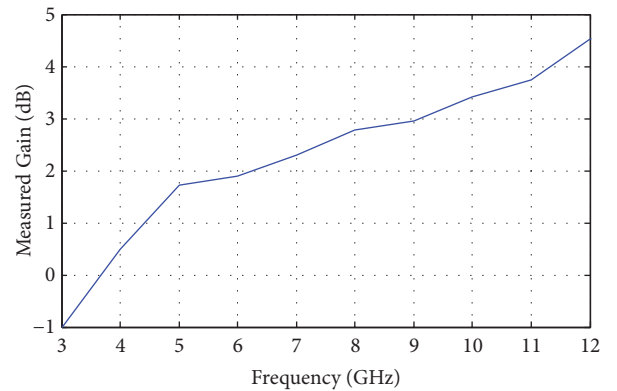


FIGURE 5: Measured gain of the proposed antenna.

Figure 7 shows the simulated and measured values of gain diversity. As it can be seen from the results, the gain diversity reaches up to 10 dB over the band of frequencies

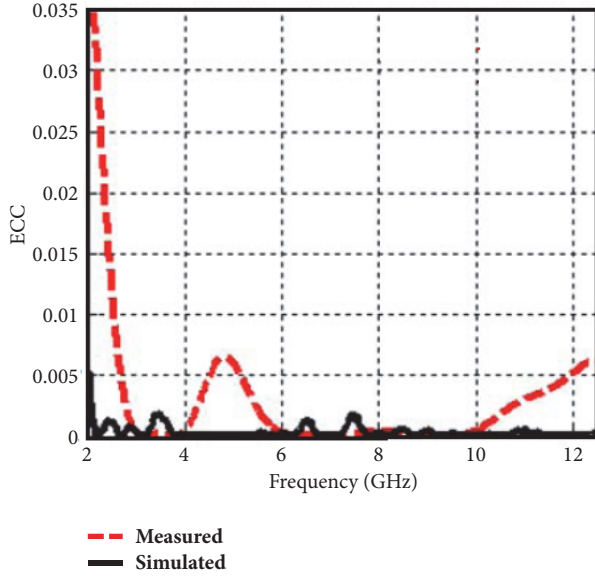


FIGURE 6: Simulated and measured ECC.

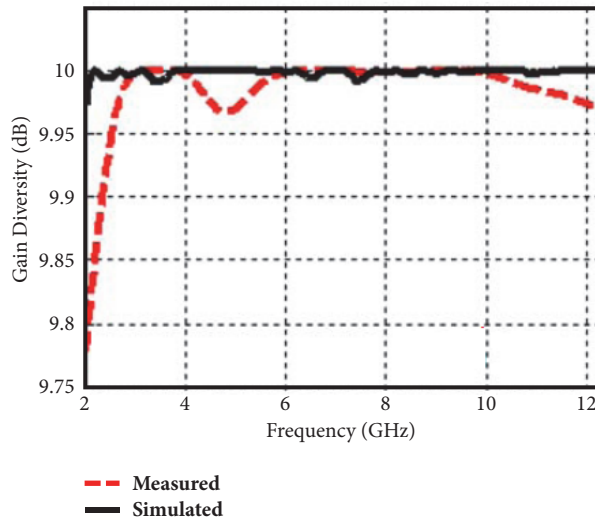


FIGURE 7: Simulated and measured gain diversity.

under consideration. Certain variation can be observed in measured results due to reflections.

A comparison of performance of the proposed antenna with similar antennas available in literature is given in Table 3. This table clearly indicates that the proposed antenna is very compact with high isolation and good MIMO and diversity performance as compared to similar antennas available.

4. Conclusion

A novel compact UWB MIMO antenna system has been presented in this paper. The 2×2 MIMO antenna systems consisted of two asymmetric “F” type structures with a very compact fractured ground plane. The presented MIMO antenna system has very compact size; the overall volume is

TABLE 3: Performance Comparison of the proposed antenna with previously published work.

Reference	Size (mm ²)	Bandwidth (GHz)	Isolation (dB)	ECC	DG (dB)
[20]	35 × 40	3.1–10.6	−16	0.01	-
[21]	27 × 28	3–10.6	−16	0.02	-
[22]	32 × 32	3.1–10.6	−15	0.04	-
[23]	50 × 30	2.5–14.5	−20	0.04	7.4
Proposed work	13 × 25	2–12	−20	0.009	9.8

$13 \times 25 \times 0.254 \text{ mm}^3$. The distance between two elements of the antenna system is 13.2 mm and the coupling between both elements over the total transmission bandwidth is less than -20 dB with peak minimum values reaching up to -35 dB . The maximum gain of 4.8 dB has been observed, whereas the gain at the center frequency was measured as 2.8 dB. Furthermore, the radiation patterns are observed isotropic. Good agreement has been achieved between the results of designed prototype of the MIMO antenna system and its simulated model.

Data Availability

The data used to support the findings of this study are available from the corresponding author upon request.

Conflicts of Interest

The authors declare that there are no conflicts of interest regarding the publication of this paper.

Acknowledgments

This work has been supported by Grant no. BA-1512, awarded by University of Hail, Kingdom of Saudi Arabia.

References

- [1] T. Dateki, H. Seki, and M. Minowa, “From LTE-advanced to 5G: Mobile access system in progress,” *Fujitsu scientific & technical journal*, vol. 52, no. 2, pp. 97–102, 2016.
- [2] W. OBILE, “Ericsson mobility report,” ed: Nov, 2016.
- [3] G. Association, “5G Spectrum–Public Policy Position,” *White Paper*, Nov 2016.
- [4] W. FCC, “DC, Federal Communications Commission revision of Part 15 of the Commissions rules regarding ultra-wideband transmission systems,” *First Report Order FCC*, vol. 2, p. V48, 2002.
- [5] F. E. Tubbal, R. Raad, and K.-W. Chin, “A wideband F-shaped patch antenna for S-band CubeSats communications,” in *Proceedings of the 10th International Conference on Signal Processing and Communication Systems, ICSPCS 2016*, aus, December 2016.
- [6] Y. Li, B. Yu, H. Shen, L. Zhu, and G. Yang, “An 8-port planar UWB MIMO antenna for future 5G micro wireless access point applications,” in *Proceedings of the 2017 International Applied Computational Electromagnetics Society Symposium in China, ACES-China 2017*, chn, August 2017.

- [7] J. Xu, M. Zhao, R. Zhang et al., "A Wideband F-Shaped Microstrip Antenna," *IEEE Antennas and Wireless Propagation Letters*, vol. 16, pp. 829–832, 2017.
- [8] M. Usman, R. A. Abd-Alhameed, and P. S. Excell, "Design considerations of MIMO antennas for mobile phones," in *Proceedings of the Progress in Electromagnetics Research Symposium 2008, PIERS 2008 Hangzhou*, pp. 718–722, chn, March 2008.
- [9] M. Welborn and J. McCorkle, "The importance of fractional bandwidth in ultra-wideband pulse design," *IEEE International Conference on Communications*, vol. 2, pp. 753–757, 2002.
- [10] S. S. Jehangir and M. S. Sharawi, "A Miniaturized UWB Biplanar Yagi-Like MIMO Antenna System," *IEEE Antennas and Wireless Propagation Letters*, vol. 16, pp. 2320–2323, 2017.
- [11] L. Chen, Y.-F. Liu, and P.-C. Wu, "Design of compact asymmetric coplanar strip-fed UWB antenna with dual band-notched characteristics," *Progress in Electromagnetics Research Letters*, vol. 47, pp. 103–109, 2014.
- [12] B. Kul, G. Kirman, P. Ergul, Z. B. Kartal, and T. Imeci, "L, U, T and F-shaped slots in patch antenna," in *Proceedings of the 2017 International Applied Computational Electromagnetics Society Symposium - Italy, ACES 2017*, ita, March 2017.
- [13] R. Ramasamyraja, M. Pandiguru, and V. Arun, "Design of ultra wide band antenna for tactical communication in electronic warfare," in *Proceedings of the 3rd International Conference on Communication and Signal Processing, ICCSP 2014*, pp. 1256–1259, ind, April 2014.
- [14] A. A. Omar, "Design of ultrawideband coplanar waveguide-fed Koch-fractal triangular antenna," *International Journal of RF and Microwave Computer-Aided Engineering*, vol. 23, no. 2, pp. 200–207, 2013.
- [15] S. Adnan, R. A. Abd-Alhameed, H. I. Hraga, Z. Z. Abidan, M. Usman, and S. M. R. Jones, "Design studies of ultra-wideband microstrip antenna for ultra-wideband communication," in *Proceedings of the Loughborough Antennas and Propagation Conference, LAPC 2009*, pp. 365–368, gbr, November 2009.
- [16] M. Y. Elsalamouny and R. M. Shubair, "Novel design of compact low-profile multi-band microstrip antennas for medical applications," in *Proceedings of the Loughborough Antennas and Propagation Conference, LAPC 2015*, gbr, November 2015.
- [17] Y. Rahayu, T. A. Rahman, R. Ngah, and P. Hall, "Ultra wideband technology and its applications," in *Proceedings of the 2008 IFIP International Conference on Wireless and Optical Communications Networks - (WOCN)*, pp. 1–5, Surabaya, Indonesia, May 2008.
- [18] S. Blanch, J. Romeu, and I. Corbella, "Exact representation of antenna system diversity performance from input parameter description," *IEEE Electronics Letters*, vol. 39, no. 9, pp. 705–707, 2003.
- [19] K. Rosengren and P.-S. Kildal, "Radiation efficiency, correlation, diversity gain and capacity of a six-monopole antenna array for a MIMO system: Theory, simulation and measurement in reverberation chamber," pp. 7–16.
- [20] S. Zhang, Z. Ying, J. Xiong, and S. He, "Ultrawideband MIMO/diversity antennas with a tree-like structure to enhance wideband isolation," *IEEE Antennas and Wireless Propagation Letters*, vol. 8, pp. 1279–1282, 2009.
- [21] G. Srivastava and A. Mohan, "Compact dual-polarized UWB diversity antenna," *Microwave and Optical Technology Letters*, vol. 57, no. 12, pp. 2951–2955, 2015.
- [22] J. Ren, W. Hu, Y. Yin, and R. Fan, "Compact printed MIMO antenna for UWB applications," *IEEE Antennas and Wireless Propagation Letters*, vol. 13, pp. 1517–1520, 2014.
- [23] A. Iqbal, O. A. Saraereh, A. W. Ahmad, and S. Bashir, "Mutual Coupling Reduction Using F-Shaped Stubs in UWB-MIMO Antenna," *IEEE Access*, 2017.

Research Article

Tunable Platform Tolerant Antenna Design for RFID and IoT Applications Using Characteristic Mode Analysis

Abubakar Sharif ¹, Jun Ouyang ¹, Feng Yang,¹
Rui Long,¹ and Muhammad Kamran Ishfaq²

¹*School of Electronic Science and Engineering, University of Electronic Science and Technology of China (UESTC), Chengdu, China*

²*Wireless Communication Centre, Universiti Teknologi Malaysia, Johor Bahru, Malaysia*

Correspondence should be addressed to Jun Ouyang; yjou@uestc.edu.cn

Received 2 February 2018; Accepted 4 March 2018; Published 10 May 2018

Academic Editor: Masood Ur-Rahman

Copyright © 2018 Abubakar Sharif et al. This is an open access article distributed under the Creative Commons Attribution License, which permits unrestricted use, distribution, and reproduction in any medium, provided the original work is properly cited.

Radio frequency identification (RFID) is a key technology to realize IoT (Internet of Things) dreams. RFID technology has been emerging in sensing, identification, tracking, and localization of goods. In order to tag a huge number of things, it is cost-effective to use one RFID antenna for tagging different things. Therefore, in this paper a platform tolerant RFID tag antenna with tunable capability is proposed. The proposed tag antenna is designed and optimized using characteristic mode analysis (CMA). Moreover, this tag antenna consists of a folded patch wrapped around FR 4 substrate and a feeding loop element printed on a paper substrate. The inductive feeding loop is stacked over folded patch and it provides impedance match with RFID chip. Because of separate radiating and feeding element, this tag antenna has a versatility of impedance matching with any RFID chip. Furthermore, this tag is able to cover American RFID band (902–928 MHz) and can be tuned to European RFID band (865–868 MHz) by adding tunable strips. In order to demonstrate platform tolerant operation, the read range of RFID tag is measured by mounting it on different materials. The maximum read range of RFID tag is 4.5 m in free space or on dielectrics and 6.5 m above 200 × 200 mm² metal plate, respectively.

1. Introduction

The modern wireless technologies are driving this world towards a new paradigm which includes Internet of Things (IoT) and Internet of Everything (IoE). In IoT world, everything will have its own unique identity. The Internet of Things (IoT) will provide an emerging integrated wireless platform, where physical and virtual things can be uniquely identified on a global scale and are connected with a global network. IoT becomes prevalent in both research and industries due to its unique emerging applications like smart cities [1, 2], connected vehicles [2], healthcare monitoring [3–5], and so on [2]. Radio frequency identification (RFID) is one of the vital technologies of IoT since it enables a device (object) not only to share its unique digital code across a network wirelessly, but also to capture its physical status for localization on a global scale [6]. RFID in combination with IoT has opened a new paradigm and new era of applications [7]. A descriptive

modal to enable an IoT network integrated with RFID technology is shown in Figure 1.

The thing's basic information will be stored in electronic RFID tag in form of electronic product code (EPC) or universal identification (UID) and this information can be read by wireless RFID reader, which can be accessed from anywhere through Internet [8–10].

Passive ultrahigh (UHF) RFID tags are more attractive for most of applications because of their long-read range and high data rate capabilities. Moreover, the low cost, easily printable structure of UHF RFID tags enables them to integrate or embed inside tagged objects, to give them a unique attribute. However, UHF RFID tags are much more sensitive towards host tagging objects such as metals, wood, and glass. This sensitivity, on one side, is good for exploiting UHF RFID tags as sensing device. On the other hand, this sensitivity towards different surfaces requires a separate UHF RFID

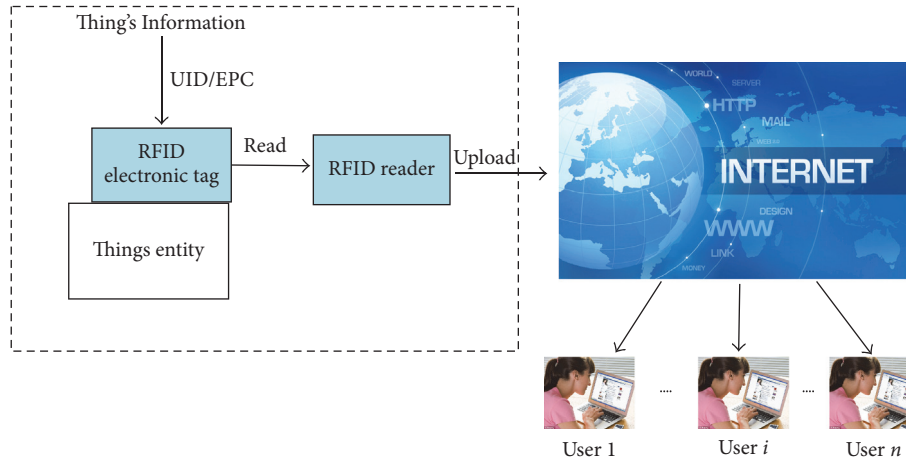


FIGURE 1: IoT descriptive modal integrated with RFID.

tag design for each tagged entity [7, 11]. Therefore, it is advantageous and cost-effective to design one low cost, platform tolerant antenna solution to tag most of the things.

In literature, there are many solutions available to solve this problem of platform tolerant UHF RFID tag especially for counter metallic surface effects [12, 13]. In [14], a dual layer PIFA antenna was introduced for platform tolerant applications. However, the performance of this design is highly depending on location of vias. Also, the dual layer structure with introduction of vias makes it a costly solution. A single layer coupled loop based antenna fabricated on 3 mm thick FR 4 substrate was proposed in [15], for tagging metal and low permittivity dielectric materials. Although this proposed antenna works on metal with read range of 6 m, its major drawback is substrate thickness. In [16], a stepped impedance coupled patch antenna was designed on a thin substrate. However, this coupled patch has small bandwidth especially on metallic surfaces. Another folded patch antenna with digital edge serration was designed in [17], for tagging metallic objects. This antenna was wrapped around 3 mm thick substrate with RFID chip mounted on vertical edge, which leads to a structure which is expensive and difficult to fabricate. Also, the vertical chip mounting configuration is more vulnerable to damage. Another solution was proposed in [18] by employing a hybrid dual port tag antenna, which consists of a dipole embedded with a patch antenna. This design has large size with 3.2 mm substrate thickness.

There are many techniques to design an efficient platform tolerant antenna such as impedance analysis, employing metamaterials (electromagnetic bandgap (EBG), artificial magnetic conductance (AMC)), and circuit analysis.

Characteristic mode analysis (CMA) in combination with theory of characteristic modes (TCM) is becoming a prevalent systematic tool to design efficient terminal antennas. The use of TCM in antenna design was not new topic. It was first proposed by Garbacz and later redefined by Harrington and Mautz [19]. However, in some recent years, TCM was revisited to get physical insight into antenna designing. TCM is more attractive and systematic approach because of its following features [19, 20]. (1) It provides a more systematic

design approach rather than a brute-force. (2) It also allows designer to get physical insight into antenna's operation. (3) It can help to find resonance frequency of specific mode. (4) It also allows finding the optimum feed arrangement to excite these specific modes. Moreover, there are very few designs available using CMA for RFID [21, 22] and IoT applications [23].

In this paper, a tunable platform tolerant folded patch antenna is proposed for UHF RFID and IoT applications using characteristic mode analysis. This antenna consists of a folded patch (wrapped around FR 4 substrate) and a small inductive feeding loop. The feeding loop printed on a paper substrate is stacked over folded patch configuration. The proposed folded patch is optimized using CMA to resonate at 915 MHz. The small feeding loop is connected with RFID chip to provide a conjugate impedance match.

Because of separate radiating and feeding element, the proposed tag antenna has a versatility of impedance matching with any RFID chip. Furthermore, this tag is able to cover US RFID band and can be tuned to European RFID band by adding tunable strips. In order to validate platform tolerant operation, the read range of RFID tag is measured by mounting it on different materials. The maximum read range of RFID tag is 4.5 m in free space or on dielectrics and 6.5 m above $200 \times 200 \text{ mm}^2$ metal plate, respectively. Moreover, this tag can also be equipped with IoT based sensors to sense environmental effects and processes, thanks to its platform tolerant capability. The low cost, tunable, and platform tolerant feature of this antenna makes it suitable for RFID and IoT applications.

2. Characteristic Mode Analysis

2.1. Theory of Characteristic Modes (TCM). Characteristic modes can be defined as orthogonal surface current modes of an arbitrary shaped conducting body, which totally depend on its shape and size and are independent of any feed source.

Moreover, characteristic modes (CM) can be derived by solving eigenvalue equations, obtained from Method of Moments (MoM) based impedance matrix as follows:

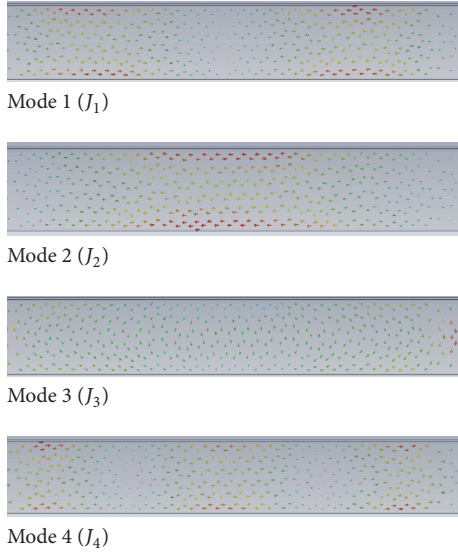


FIGURE 2: Normalized current distribution at 915 MHz of first four associated modes of $160 \times 25 \text{ mm}^2$ rectangular plate.

$$[X][J]_n = \lambda_n [R][J]_n, \quad (1)$$

where R and X are real and imaginary components of MoM impedance matrix; J_n are eigencurrents and λ_n are eigenvalues:

$$\begin{aligned} R &= \frac{Z + Z^*}{2}, \\ X &= \frac{Z - Z^*}{2j}. \end{aligned} \quad (2)$$

Furthermore, because of the orthogonality of characteristics modes, they can be used to derive total surface current J of an antenna as follows:

$$J = \sum_n \frac{V_n^i J_n}{1 + \lambda_n}, \quad (3)$$

where V_n^i is model excitation coefficient and it can be obtained as expressed by

$$V_n^i = \iint_S J_n \cdot E^i ds. \quad (4)$$

The product $V_n^i J_n$ determines the coupling between n th mode and excitation. It also provides information about which mode of antenna is excited by feed or incident electric field (E^i).

2.2. Characteristic Mode Analysis for Rectangular Plate. The theory of characteristic modes (TCM) has been employed to calculate characteristic modes of a rectangular plate ($160 \times 25 \text{ mm}^2$) mounted on a FR 4 (2 mm thick, loss less) substrate. The multilayer solver of CST Microwave studio has been used for modal analysis.

Figure 2 shows the normalized current distribution (at 915 MHz) of first four associated characteristic modes of

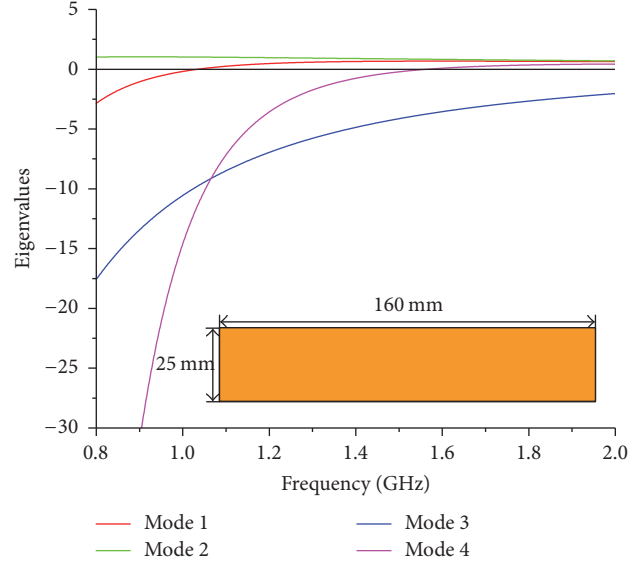


FIGURE 3: Eigenvalues of typical rectangular plate in free space.

rectangular plate (as shown in subset of Figure 3). In order to understand behavior of these modes, eigenvalues will be used in combination with normalized current distributions. The eigenvalue associated with resonating modes is zero; it is concluded that the smaller the eigenvalue associated with a mode is, the more efficiently it will contribute to radiation. Moreover, the sign of eigenvalue determines whether a mode is storing electrical energy ($\lambda_n < 0$) or magnetic energy ($\lambda_n > 0$). The eigenvalues associated with aforementioned modes of rectangular plate in free space are shown in Figure 3. The mode J_1 resonates near 1.1 GHz as eigenvalue is zero near 1.1 GHz. Because of symmetry, the mode J_1 will propagate even if we use half of the length of rectangular plate. As can be seen from Figure 2, the mode J_2 behaves like an inductive mode; it can also be confirmed from its associated eigenvalue ($\lambda_n > 0$). Furthermore, mode J_3 represents capacitor like current distribution with eigenvalue ($\lambda_n < 0$). Mode J_4 is a resonating mode at 1.6 GHz.

Another parameter known as modal significance is also very useful in determining how efficiently a mode resonates. Also, with the application of external excitation source, modal significance determines the contribution of particular mode to total radiation. The modal significance associated with characteristic modes of $160 \times 25 \text{ mm}^2$ rectangular plate is shown in Figure 4.

Mode 1 and Mode 4 are resonating modes and will contribute to radiation, when excited by a source, since their modal significance approaches 1 (as shown in Figure 4).

Modal significance can be defined as follows:

$$MS_n = \frac{1}{|1 + j\lambda_n|}. \quad (5)$$

Additionally, characteristic angle computed from eigenvalues as expressed by (6) is also very useful in determining exact resonance frequencies especially where more than one mode needs to be excited (e.g., circular polarized antenna design).

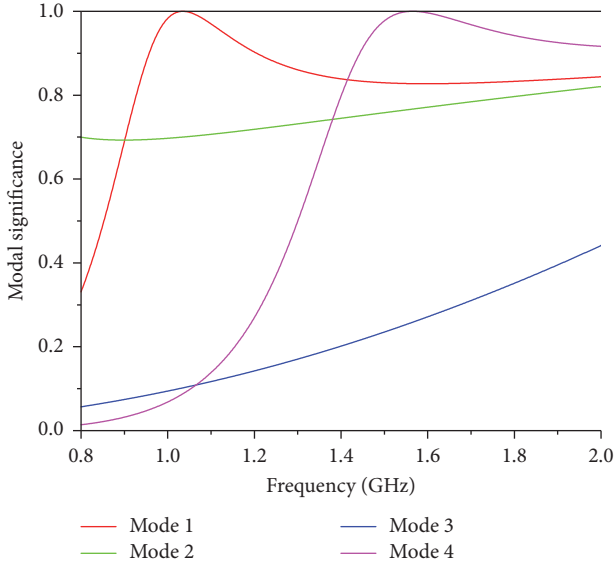


FIGURE 4: Modal significance of first four modes of $160 \times 25 \text{ mm}^2$ rectangular plate.

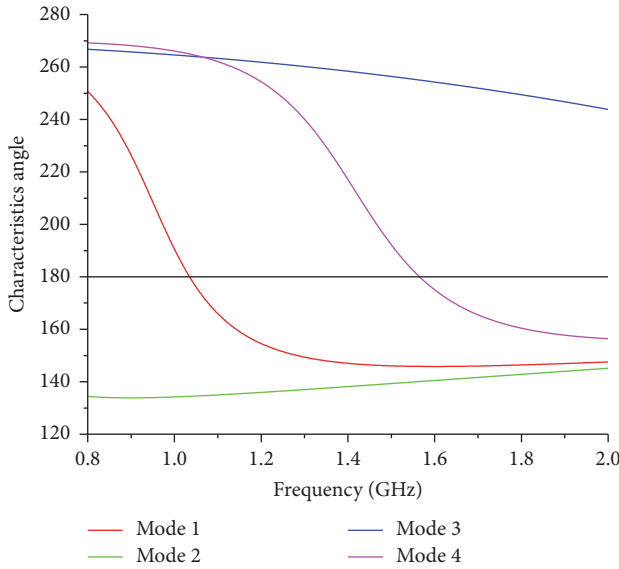


FIGURE 5: Characteristic angle of first four modes of $160 \times 25 \text{ mm}^2$ rectangular plate.

The characteristic angle associated with first four modes of $160 \times 25 \text{ mm}^2$ rectangular plate are presented in Figure 5. For resonating modes $\alpha_n = 180^\circ$, therefore, Mode 1 and Mode 4 are resonating modes at 1.1 GHz and 1.6 GHz, respectively.

$$\alpha_n = 180^\circ - \tan^{-1} \lambda_n. \quad (6)$$

3. RFID Tag Antenna Design Using CMA

3.1. CMA of Dipole Patch. Start from Mode 2 (J_2) of aforementioned rectangular plate ($160 \times 25 \text{ mm}^2$). As discussed earlier Mode 2 is an inductive mode. In order to make it as a resonating mode, a small slot (corresponding to adding

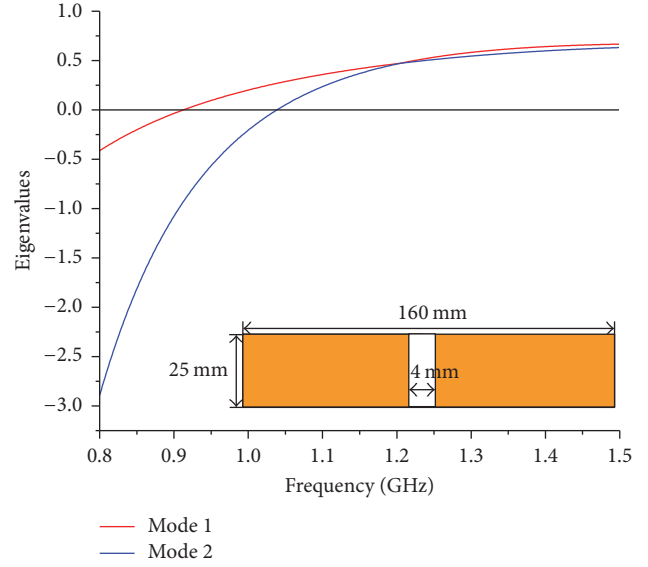


FIGURE 6: Eigenvalues of dipole patch in free space.

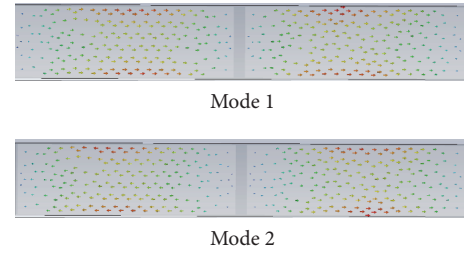


FIGURE 7: Normalized current distribution at 915 MHz of two associated resonating modes of dipole patch.

a capacitance) is created and it becomes dipole like patch as shown in subset of Figure 6. As can be seen from Figure 7, the two modes are resonating at 920 MHz and 1.1 GHz, respectively. Furthermore, it can be inferred from normalized current distribution (shown in Figures 2 and 7) that Mode 1 of rectangular plate and Mode 2 of dipole patch are same. It means that the introduction of slot has no effect on this mode.

Inductive Mode 2 of rectangular plate becomes a resonating mode with introduction of capacitance introduced by small slot.

3.2. CMA of Proposed Folded Patch. The dipole patch is working at 920 MHz (US RFID bands 902 MHz to 928 MHz); however its length is more in order to use it as RFID tag. Due to symmetry, Mode 1 (resonating at 920 MHz) of dipole patch will still resonate, even if half of the dipole patch is used (80 mm). In order to reduce the length further the patch is folded with same length on FR 4 substrate as shown in subset of Figure 8. The eigenvalue plot of resulting folded patch antenna is illustrated in Figure 8. To confirm its operation as platform tolerant design, the eigenvalue plot of one resonating mode is depicted in Figure 8, after placing this folded patch in free space and above a finite perfect electric conductor (PEC) boundary. It can be observed from eigenvalue plot

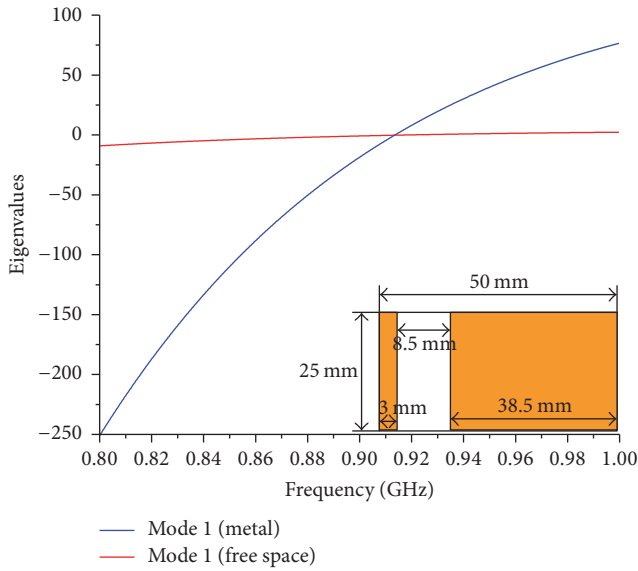


FIGURE 8: Eigenvalues of folded patch in free space and above metal plate.

that the resonance frequency of Mode 1 is almost same for both in free space and above PEC boundary conditions.

However, the slope of eigenvalue plot of Mode 1 is different for two different boundary conditions. Moreover, Mode 1 of folded patch has a steep slope, above metal plate as compared with free space, which means that folded patch has more bandwidth in free space as compared with above metal.

3.3. CMA of Proposed Folded Patch with Tunable Strips. As can be seen from normalized current distribution of folded patch antenna expressed in Figure 9, since the current in Mode 1 is maximum near folded end and decreases towards the slot, it behaves like cavity backed slot antenna. The effective length of current path can be increased by adding two tunable strips on both sides of folded patch near the slot as depicted in subset of Figure 10. Hence, the antenna can be tuned to European RFID band (866 MHz–868 MHz). The tuning of folded patch to European RFID band can also be confirmed from eigenvalue and modal significance plot (Figure 10) of this folded patch after adding tuning strips.

4. Simulation Results

In order to realize an RFID tag antenna, a feeding strategy should be proposed for the folded patch obtained after characteristic mode analysis. Since most of RFID tag chips have capacitive impedance, requiring the tag impedance to be inductive for conjugate match, therefore, inductive coupled loop is a good option to feed this antenna. Besides, the conjugate matching, a separate coupled inductive loop, also provides a versatility of impedance matching with any RFID chip, just by altering loop parameter, without any change in main radiator (folded patch).

The complete antenna geometry of proposed folded patch RFID tag is shown in Figure 11. Finally, the proposed design

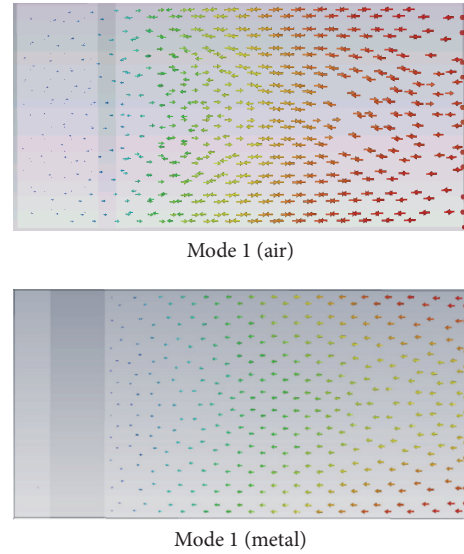


FIGURE 9: Normalized current distribution at 915 MHz of folded patch.

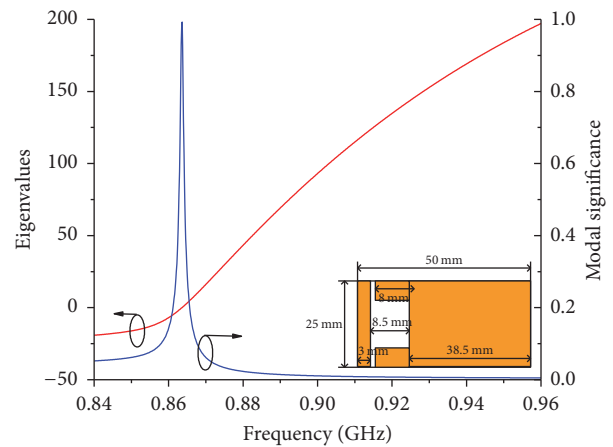


FIGURE 10: Eigenvalue and modal significance of folded patch (with tunable strips) above metal plate.

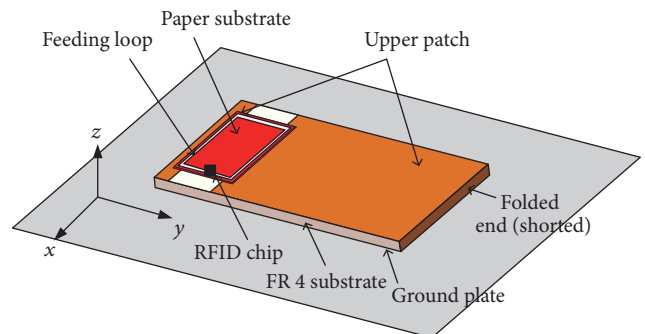


FIGURE 11: Geometry of proposed folded patch RFID tag antenna.

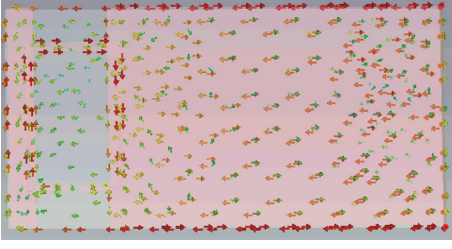


FIGURE 12: Normalized surface current distribution of proposed folded patch RFID tag with feeding loop.

TABLE 1: Parameters of the antenna (mm).

L_s	W_s	L_1	L_2	L_3	L_p	W_p	L_t	h_1	h_2
50	25	38.55	8.5	3	11	17	8	2	0.3

consists of a folded patch as main radiator and a small inductive feeding loop in order to match with RFID chip.

Furthermore, Figure 12 shows the surface current distribution after placing the inductive feeding loop above folded patch; it is clear from Figure 12 that the feed loop excites the same mode as expressed in characteristics mode analysis of folded patch antenna (Figure 9). The proposed folded patch is wrapped around a low cost FR 4 substrate ($\epsilon_r = 4.3$, $\delta = 0.025$). Furthermore, the inductive feeding loop is printed on a 0.25 mm thick paper substrate.

The detailed dimensions of proposed design are illustrated in Figure 13. Antenna design parameters involved in simulation are optimized further using frequency domain solver of CST microwave studio and are listed in Table 1. Moreover, Alien Higgs H3 has been used as RFID chip with impedance (30–201j) computed from equivalent circuit of parallel 1500 ohms resistance and 0.85 pF capacitance.

As shown in Figure 14, the simulated input impedance plot of this tag design confirms the working antenna in American RFID band (US) without tunable strips and can be tuned to European RFID (EU) band with tuning strips. The real and imaginary impedance of antenna is ranging from 30 to 40 Ohms and 180 to 205 Ohms, respectively, in required RFID bands, which is best matched with Alien Higgs-3 RFID chip.

To verify antenna performance as platform tolerant design, for simulation purpose, the antenna is placed on two different materials: (1) a 200×200 mm² plate with relative permittivity $\epsilon_r = 4$, representing a low permittivity dielectric; (2) a 200×200 mm² metal plate. For both cases, the power reflection corresponding to conjugate match of this proposed design is shown in Figure 15. The 3 dB bandwidth of antenna is more than 40 MHz for both cases in US band, with a little bit shift in center frequency for metal case. However, the bandwidth of antenna is enough to protect it from detuning. Moreover, the antenna also provides 3 dB bandwidth of 30 MHz in EU band. Also, in this case, there is a small shift in center frequency as compared with metal and dielectric case.

Furthermore, the directivity of this tag antenna is 5.87 dBi, after mounting it on a 200×200 mm² metal plate as depicted in Figure 16.

5. Measurement and Discussion

A prototype of proposed RFID tag was fabricated on a ground substrate with one shorted end as shown in Figure 17. Alien Higgs H3 RFID chip is connected with small feeding loop printed on a paper substrate. This paper substrate containing feed loop is then pasted on slot of folded patch.

To validate the performance of antenna on different materials, the input impedance of this tag was measured using Agilent E8363B vector network analyzer by following the procedure expressed in [24].

The impedance measurement setup is depicted in the inset of Figure 18. The outer coats of two coaxial cables were soldered together, while the single end of each cable was attached with open ends of feeding loop. The return loss of antenna was computed by formula given in [24] using parameter measured from this setup.

As compared with simulated results (Figure 18), a better impedance match was observed for 865 to 868 MHz band, whereas the value of measured return loss is more for 902 to 928 MHz band. Overall, the measured results show a good agreement with simulation results with a little reduction in bandwidth. This may be due to some fabrication error or cable loss. Moreover, the measurement procedure also introduces some discrepancies.

Furthermore, the glue used to paste the feeding loop also introduces some change in permittivity and thickness of substrate.

The theoretical read range of RFID tag can be estimated using Friis equation as follows:

$$R_{\text{tag}} = \frac{\lambda}{4} \sqrt{\frac{P_r G_r G_a \tau}{P_{\text{th}}}}, \quad (7)$$

where P_r , G_r are transmitted power and gain of RFID reader, G_a is gain of tag antenna, and P_{th} is minimum threshold power of chip.

However, another better and more practical approach to estimate maximum read range with maximum permitted EIRP is to calculate read range first for small value of EIRP with a fixed distance as expressed by

$$R_{\text{max}} = R_{\text{ref}} \sqrt{\frac{\text{EIRP}_{\text{max}}}{\text{EIRP}_{\text{ref}}}}. \quad (8)$$

where R_{max} is maximum read range of the tag, R_{ref} is reference fixed distance measured in lab, EIRP_{max} is maximum permitted EIRP = 4 Watts for most of the regions, and EIRP_{ref} is reference EIRP of range measuring equipment. A Tagformance Pro device (from Voyantic Company) based setup was employed to measure maximum read range in lab as illustrated in Figure 19. A frequency sweep is run by the Tagformance with a fixed distance (R_{ref}) provided by foam spacer. The theoretical read range is estimated by system software using formula expressed by (8). The measured read range of proposed tag above 200×200 mm² metal plate using Tagformance setup is shown in Figure 20. As is clear from Figure 20, the measured read range of proposed tag is 6.2 m on 200×200 mm² metal plate.

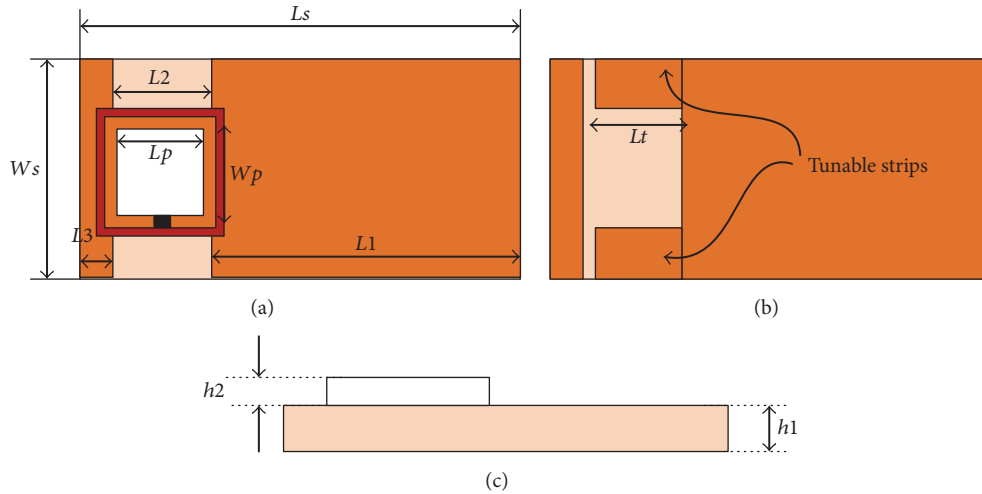


FIGURE 13: Dimension of proposed folded patch RFID tag. (a) Front view; (b) front view with tuning strips; (c) side view.

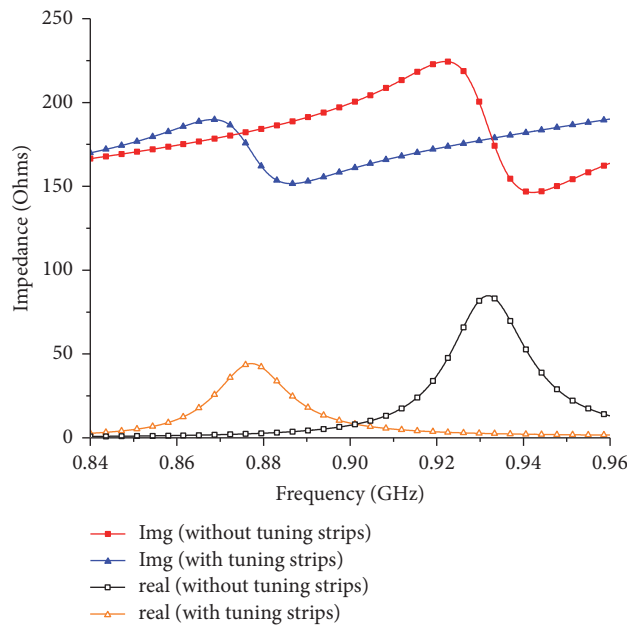


FIGURE 14: Simulated impedance of proposed folded patch RFID tag.

To verify the robustness of this tag solution, the read range of RFID tag was measured after mounting on different materials in outdoor and indoor lab environments with 4 W EIRP. The measurement setup includes a laptop, Impinj R420 reader, and a circular polarized reader antenna. The read range measurements are carried out at 920 MHz.

Furthermore, the different mounting materials used in range measurement were of plastic, wood, glass, and book ($200 \times 200 \text{ mm}^2$). The maximum measured read range on aforementioned materials is illustrated in Figure 21. Moreover, the maximum read measured on metal plate is 6.5 m,

while the measured read range on all other materials is more than 4.5 m in indoor environment. However, there is a small reduction in read range observed in outdoor environment.

Moreover, the measured read range pattern of this tag design is shown in Figure 22. A good unidirectional read range pattern with maximum read distance of 6.5 m is acquired in xz -plane. Also, it can be observed from Figure 22 that the maximum read angle is tilted since the surface current distribution is more near folded edge.

The comparison of proposed design with some other RFID tags in terms of size and performance is listed in Table 2.

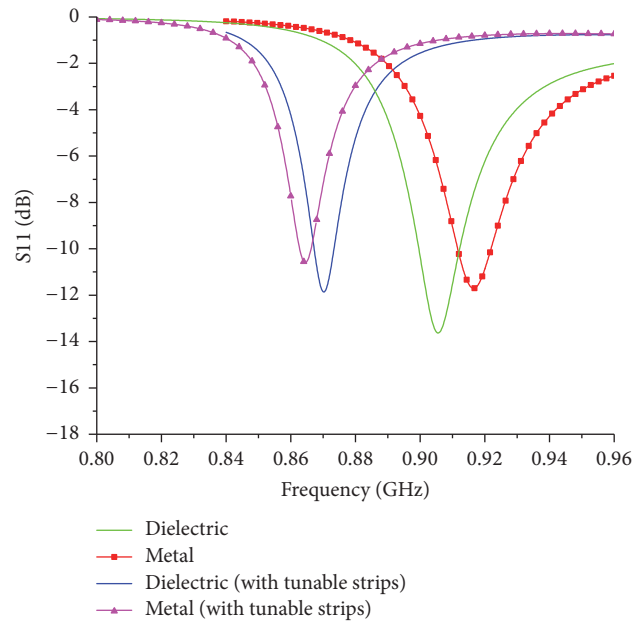


FIGURE 15: Simulated return loss of proposed RFID tag on $200 \times 200 \text{ mm}^2$ dielectric and metal plate.

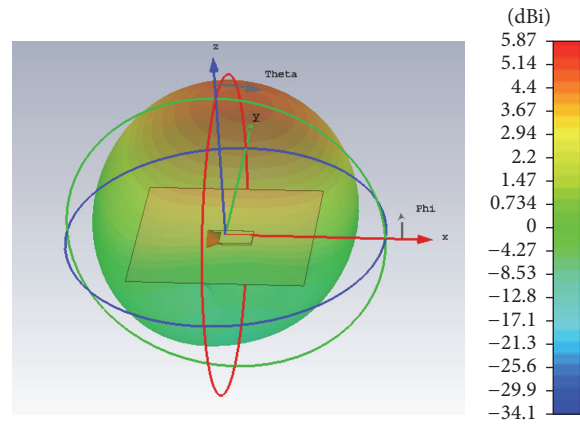


FIGURE 16: Radiation pattern of tag on $200 \times 200 \text{ mm}^2$ metal plate.

TABLE 2: Comparison of proposed antenna with other several designs.

Reference	Size (mm^3)	Metal plate size (mm^2)	Read range (m) (metal/dielectric)	Tunable
This work	$50 \times 25 \times 2$	200×200	6.5/4.5	Yes
[14]	$56 \times 25 \times 3.5$	500×500	4/-	No
[15]	$55 \times 41.5 \times 3$	200×200	6.1/14	No
[16]	$88 \times 60 \times 0.76$	150×150	5.4/5.7 (body)	No
[17]	$30 \times 30 \times 3$	200×200	7/3.5	No
[18]	$84 \times 41 \times 3.2$	200×200	5.6/8	No

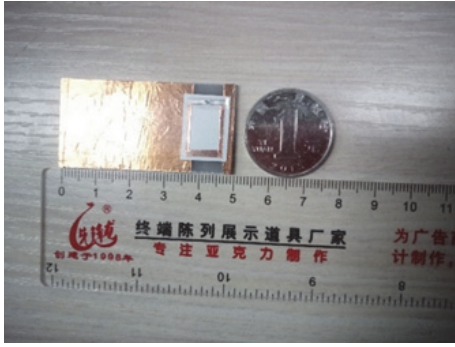


FIGURE 17: Fabricated prototype of proposed RFID tag antenna.

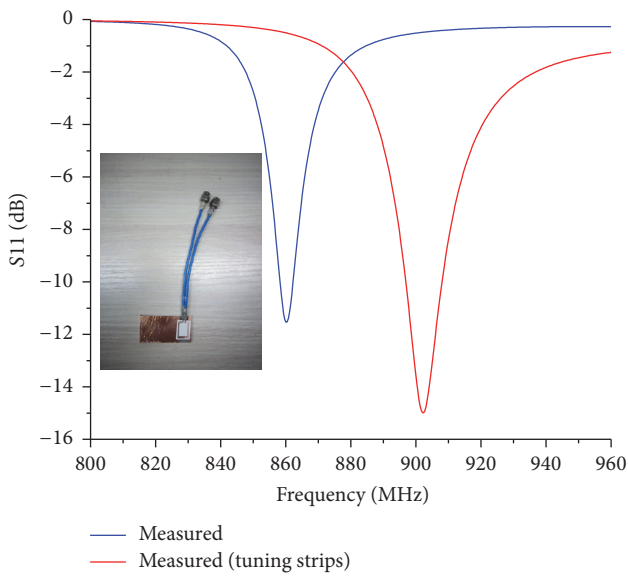


FIGURE 18: Measured return loss of proposed RFID tag on $200 \times 200 \text{ mm}^2$ metal plate.

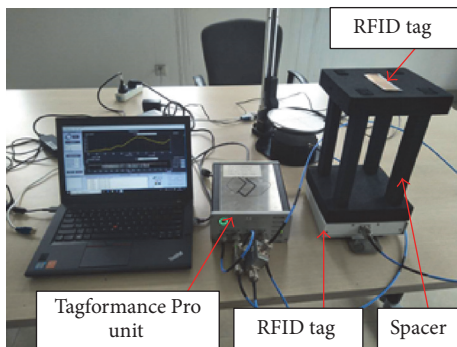


FIGURE 19: Tagformance based read range measuring setup.

6. Conclusion

In Internet of Things (IoT), every object can be connected to Internet through a unique digital code to identify it on global scale. RFID in combination with IoT has opened a new paradigm and era of applications. In order to tag a huge number

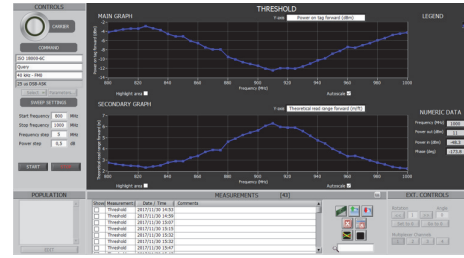


FIGURE 20: Theoretical read range proposed RFID tag on $200 \times 200 \text{ mm}^2$ metal plate using Tagformance.

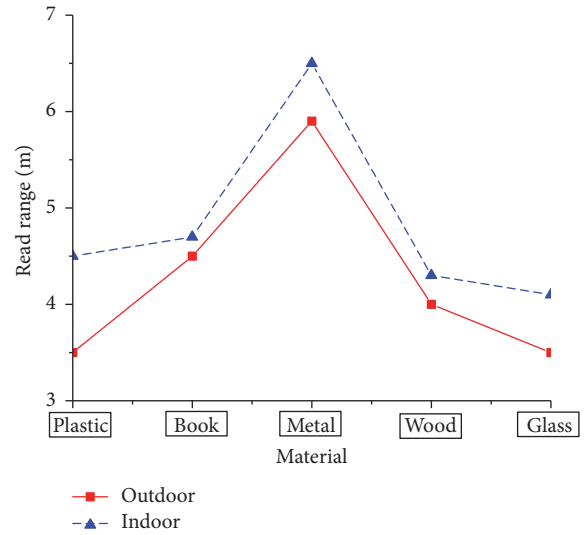


FIGURE 21: Measured read range of proposed RFID tag on block of different materials ($200 \times 200 \text{ mm}^2$).

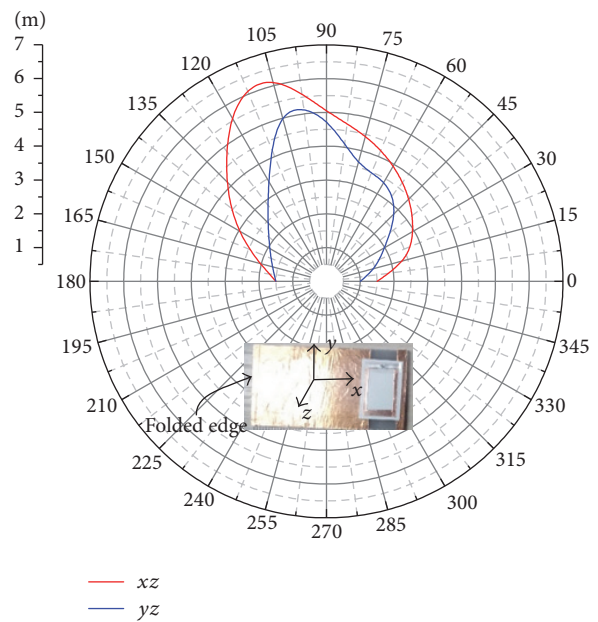


FIGURE 22: Measured read range pattern of proposed RFID tag on $200 \times 200 \text{ mm}^2$ metal plate.

of things, it is cost-effective to use one RFID tag antenna for different things. Therefore, in this paper, a platform tolerant folded patch antenna with tunable capability is proposed for UHF RFID and IoT applications using characteristic mode analysis. The proposed design consists of a folded patch wrapped around FR 4 substrate and a small inductive feeding loop printed on a paper substrate. The proposed folded patch is optimized using CMA to resonate at 915 MHz. Since this tag has a separate radiating and feeding element, therefore it can be reusable and has a versatility of impedance matching with any RFID chip. Furthermore, in order to prove platform tolerant capability of proposed RFID tag, its read range is measured after mounting on different material. The maximum read range of RFID tag is 4.5 m in free space or on dielectrics and 6.5 m above $200 \times 200 \text{ mm}^2$ metal plate, respectively. The platform tolerant capability of this antenna makes it favorable for integration with IoT sensors, which can be used to sense environmental effects and processes. Moreover, the low cost and tunable features of this antenna make it suitable candidate for RFID and IoT applications.

Conflicts of Interest

The authors declare that there are no conflicts of interest regarding the publication of this paper.

References

- [1] A. Zanella, N. Bui, A. P. Castellani, L. Vangelista, and M. Zorzi, "Internet of things for smart cities," *IEEE Internet of Things Journal*, vol. 1, no. 1, pp. 22–32, 2014.
- [2] D. Pugh, "The Internet of Things About IDTechEx IDTechEx provides clarity on emerging technologies".
- [3] S. M. Riazul Islam, D. Kwak, M. Humaun Kabir, M. Hossain, and K.-S. Kwak, "The internet of things for health care: a comprehensive survey," *IEEE Access*, vol. 3, pp. 678–708, 2015.
- [4] L. Catarinucci, D. de Donno, L. Mainetti et al., "An IoT-aware architecture for smart healthcare systems," *IEEE Internet of Things Journal*, vol. 2, no. 6, pp. 515–526, 2015.
- [5] M. Alhussein, "Monitoring Parkinson's Disease in Smart Cities," *IEEE Access*, vol. 5, pp. 19835–19841, 2017.
- [6] G. Marrocco, "RFID & IoT: a Synergic Pair," *IEEE RFID Virtual Journal*, vol. 8, pp. 1–21, 2015.
- [7] D. M. Dobkin, *The RF in RFID. UHF RFID in Practice*, Elsevier, Newnes, MA, USA, 2nd edition, 2013.
- [8] Y. Huang and G. Li, "Descriptive models for Internet of things," in *Proceedings of the 2010 International Conference on Intelligent Control and Information Processing, ICICIP 2010*, pp. 483–486, China, August 2010.
- [9] T. Yan and Q. Wen, "A secure mobile RFID architecture for the Internet of Things," in *Proceedings of the 2010 IEEE International Conference on Information Theory and Information Security, ICITIS 2010*, pp. 616–619, China, December 2010.
- [10] N. Vikram and K. R. Kashwan, "Design of ISM band RFID reader antenna for IoT applications," in *Proceedings of the 2016 IEEE International Conference on Wireless Communications, Signal Processing and Networking, WiSPNET 2016*, pp. 1818–1821, India, March 2016.
- [11] E. Perret, S. Tedjini, and R. S. Nair, "Design of antennas for UHF RFID tags," *Proceedings of the IEEE*, vol. 100, no. 7, pp. 2330–2340, 2012.
- [12] A. Hamani, M. C. E. Yagoub, T.-P. Vuong, and R. Touhami, "A novel broadband antenna design for UHF RFID tags on metallic surface environments," *IEEE Antennas and Wireless Propagation Letters*, vol. 16, pp. 91–94, 2017.
- [13] H.-D. Chen, C.-Y. Sim, C.-H. Tsai, and C. Kuo, "Compact Circularly Polarized Meandered-Loop Antenna for UHF-Band RFID Tag," *IEEE Antennas and Wireless Propagation Letters*, vol. 15, pp. 1602–1605, 2016.
- [14] J. Zhang and Y. Long, "A dual-layer broadband compact UHF RFID tag antenna for platform tolerant application," *IEEE Transactions on Antennas and Propagation*, vol. 61, no. 9, pp. 4447–4455, 2013.
- [15] H. Li, J. Zhu, and Y. Yu, "Compact Single-Layer RFID Tag Antenna Tolerant to Background Materials," *IEEE Access*, vol. 5, pp. 21070–21079, 2017.
- [16] M. Polivka and M. Svanda, "Stepped impedance coupled-patches tag antenna for platform-tolerant UHF RFID applications," *Institute of Electrical and Electronics Engineers. Transactions on Antennas and Propagation*, vol. 63, no. 9, pp. 3791–3797, 2015.
- [17] F.-L. Bong, E.-H. Lim, and F.-L. Lo, "Flexible Folded-Patch Antenna with Serrated Edges for Metal-Mountable UHF RFID Tag," *IEEE Transactions on Antennas and Propagation*, vol. 65, no. 2, pp. 873–877, 2017.
- [18] A. P. Sohrab, Y. Huang, M. N. Hussein, and P. Carter, "A Hybrid UHF RFID Tag Robust to Host Material," *IEEE Journal of Radio Frequency Identification*, vol. 1, no. 2, pp. 163–169, 2017.
- [19] M. Cabedo-Fabres, E. Antonino-Daviu, A. Valero-Nogueira, and M. F. Bataller, "The theory of characteristic modes revisited: a contribution to the design of antennas for modern applications," *IEEE Antennas and Propagation Magazine*, vol. 49, no. 5, pp. 52–68, 2007.
- [20] E. Antonino-Daviu, M. Cabedo-Fabrés, M. Ferrando-Bataller, and M. Gallo, "Design of a multimode MIMO antenna using the theory of characteristic modes," *Radioengineering*, vol. 18, no. 4, pp. 425–430, 2009.
- [21] E. A. Elghannai and R. G. Rojas, "Modal-based approach to tune and enhance the frequency and dielectric bandwidth of a UHF-RFID tag antenna mounted on a dielectric substrate," in *Proceedings of the IEEE Antennas and Propagation Society International Symposium, APS 2015*, pp. 161–162, Canada, July 2015.
- [22] Z. Liang, J. Ouyang, M. Gao, and X. Cui, "A small RFID tag antenna for metallic object using characteristic mode," in *Proceedings of the 2017 IEEE International Symposium on Antennas and Propagation & USNC/URSI National Radio Science Meeting*, pp. 533–534, San Diego, CA, USA, July 2017.
- [23] Y. Gao, R. Ma, Q. Zhang, and C. Parini, "Design of very-low-profile circular UHF small antenna using characteristic mode analysis," *IET Microwaves, Antennas & Propagation*, vol. 11, no. 8, pp. 1113–1120, 2017.
- [24] X. Qing, C. K. Goh, and Z. N. Chen, "Impedance characterization of rfid tag antennas and application in tag co-design," *IEEE Transactions on Microwave Theory and Techniques*, vol. 57, no. 5, pp. 1268–1274, 2009.

Research Article

A Novel Dual Ultrawideband CPW-Fed Printed Antenna for Internet of Things (IoT) Applications

Qasim Awais,¹ Hassan Tariq Chattha ,² Mohsin Jamil ,^{2,3} Yang Jin,¹ Farooq Ahmad Tahir ,³ and Masood Ur Rehman ⁴

¹Department of Optoelectronic Engineering, Chongqing University, Chongqing, China

²Department of Electrical Engineering, Faculty of Engineering, Islamic University of Madinah, Al-Madinah, Saudi Arabia

³National University of Sciences and Technology (NUST), Islamabad, Pakistan

⁴Department of Computer Science and Technology, University of Bedfordshire, Luton, UK

Correspondence should be addressed to Hassan Tariq Chattha; chattha43@hotmail.com

Received 30 November 2017; Accepted 12 February 2018; Published 28 March 2018

Academic Editor: Luca Reggiani

Copyright © 2018 Qasim Awais et al. This is an open access article distributed under the Creative Commons Attribution License, which permits unrestricted use, distribution, and reproduction in any medium, provided the original work is properly cited.

This paper presents a dual-band coplanar waveguide (CPW) fed printed antenna with rectangular shape design blocks having ultrawideband characteristics, proposed and implemented on an FR4 substrate. The size of the proposed antenna is just 25 mm × 35 mm. A novel rounded corners technique is used to enhance not only the impedance bandwidth but also the gain of the antenna. The proposed antenna design covers two ultrawide bands which include 1.1–2.7 GHz and 3.15–3.65 GHz, thus covering 2.4 GHz Bluetooth/Wi-Fi band and most of the bands of 3G, 4G, and a future expected 5G band, that is, 3.4–3.6 GHz. Being a very low-profile antenna makes it very suitable for the future 5G Internet of Things (IoT) portable applications. A step-by-step design process is carried out to obtain an optimized design for good impedance matching in the two bands. The current densities and the reflection coefficients at different stages of the design process are plotted and discussed to get a good insight into the final proposed antenna design. This antenna exhibits stable radiation patterns on both planes, having low cross polarization and low back lobes with a maximum gain of 8.9 dB. The measurements are found to be in good accordance with the simulated results.

1. Introduction

Internet of Things (IoT) applications incorporate major advancements of computer networking, microelectronics and modern communication system. This technology enables physical sensing and actuating devices to be controlled remotely over the Internet. To attain reliable communication, these devices are required to be compact, cost-effective, and energy efficient to operate on multibands for LTE, WLAN (IEEE 802.11 a/b/g/n), WiMAX (IEEE 802.16), ZigBee (IEEE 802.15.4), GSM (800 MHz, 850 MHz, and 1900 MHz), and so on. Scope for Internet of Things (IoT) operating on these bands can be seen as in 2003; the world population was 6.3 billion and connected devices per person were 0.0793%, while with population grown to 7.2 billion in 2015, revolutionized connected devices per person increased to 3.4%. This trend is expected to grow exponentially so the demand for smaller

devices along with the better antenna module will grow as well. Due to miniaturization of embedded systems, multiple modules can be assembled on these small gadgets to improve efficiency, reliability, and robustness for various scenarios of environmental monitoring, smart cities, smart healthcare, smart grid, military/defense, and so on [1, 2].

Apart from the many advantages of power options, flexibility, ease of installation, and replacement there are numerous challenges of scalability, fault tolerance, energy harvesting, and security issues which need to be addressed for worldwide acceptability [3]. The antenna system, being the front end of all hand-held communication devices is expected to cover all major frequency bands of IEEE 802.11 (2.4–2.48 GHz) and IEEE 802.15.4 (2.5–2.69 GHz/3.4–3.69 GHz/5.25–5.85 GHz) with acceptable gain and radiation pattern for multiple integrated services. Further, it is anticipated that modern antenna design should be flexible

TABLE 1: Comparison between different existing CPW designs and our proposed work.

References	Type	Total area (mm ²)	Bandwidth	Peak gain (dBi)
[12]	Dual-band	1020	2.3–2.5 and 2.9–15.0 GHz	2.5
[13]	Dual-band	900	1.86–1.97 and 3.0–12.0 GHz	3.0
[14]	Dual-band	1250	3.4–3.6 and 8–15 GHz	-----
[15]	Tri-band	1600	2.28–2.58, 3.38–3.66, and 5.07–5.86 GHz	3.3
[16]	Tri-band	839.5	2.33–2.76, 3.05–3.88, and 5.57–5.88 GHz	2.8
[17]	Dual-band	2700	2.26–2.57 and 4.81–6.56 GHz	3.2
[18]	Dual-band	1500	2386–2510 and 4878–6002 MHz	2.6
[19]	Tri-band	896	2.3–2.8, 3.1–4.0 and 4.6–5.3 GHz	3.0
[20]	Dual-band	1400	2.2–2.55 and 3.0–5.6 GHz	2.0
	Proposed work	875	1.1 GHz–2.7 GHz and 3.15–3.65 GHz	8.9 dB

enough to regulate impedance bandwidth for various center frequencies independently [4].

Some well-known techniques such as slots in the radiating patch, defected ground structures (DGS), engraving strips on antenna, and the induction of band notched structures in the designs have been adopted to satisfy the abovementioned characteristics [4, 5]. Apart from these orthodox methods, the use of metamaterials and complementary split ring resonator (CSRR) techniques are employed in literature for getting higher gain in order to reduce cross frequency interference. Ahmed et al. implemented a magneto-electric (ME) dipole antenna that showed wide impedance bandwidth, better gain, and matching radiation patterns on both E-plane and H-plane [6]. But such cross-magneto-electric structures are not suitable for mass production in Internet of Things (IoT) due to the large size and sensitive design parameters. On the other hand, the coplanar waveguide method has advantages such as wide bandwidth, uniplanar design and ease of installation with MMIC, and active components, making it more suitable for targeted IoT applications.

Various CPW-fed antennas have been reported in literature such as multiband [3–8], CPW antennas with added strip for WLAN [9–11], and asymmetric coplanar strip antennas [12–20]. However, majority of these designs have large antenna dimensions and do not cover all the major bands of WLAN/WiMAX/LTE [13–16, 18]. Dual-band antenna in [21] with an average gain of 2.5 dB having dimensions 25 mm × 25 mm being compact in size operates only in WLAN band. Further, in some other designs, the antenna gains and reflection coefficient parameters are not impressive compared to the antenna dimensions [15–20, 22–25]. In [26], a CPW-fed multiband antenna having dimension 70.4 mm × 45 mm is implemented having an impedance bandwidth of 127 MHz for WiMAX band only. Similarly, a 70 mm × 70 mm CPW-fed WLAN antenna implemented in [27] operating at 2.4 GHz with peak gain of 6.5 dB has a very low impedance bandwidth. The rounded corners concept is found in literature to enhance the overall gain, with stable radiation patterns [22–25]. Moreover, frequency dispersion is reduced and current is uniformly distributed on radiation surface corners using this procedure. Adjustable strips in our design enabled CPW design to improve bandwidth over higher frequency bands

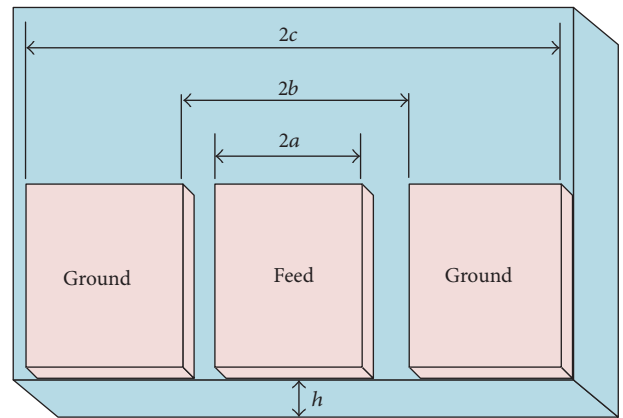


FIGURE 1: Feed line calculation in CPW design.

without compromising the overall size of 875 mm². In order to reduce size and avoid the complexity, major overlapped slots have been introduced in the proposed antenna design along with two strips above and below the main radiating patch. Compact ground plane length ratio to the overall length of the antenna is optimized to achieve 50 Ohm impedance matching by adjusting the microstrip width and gap between the microstrip and the sides of the ground plane [6, 8, 24]. In Table 1, a comparison is made between different existing CPW designs found in literature and our proposed work. Design working principle and antenna dimensions are explained in the following sections along with the detailed simulated and experimental results.

2. Design Specifications

The feed line calculation in CPW design is depicted in Figure 1, whereas the detailed geometry of the proposed antenna is shown in Figure 2. The antenna is fabricated on an FR4 substrate with relative permittivity of 4.4 having a standard thickness of 1.6 mm. The length, width, and the wavelength of the main rectangular patch is calculated and gradually modified by calculating the resonant frequencies

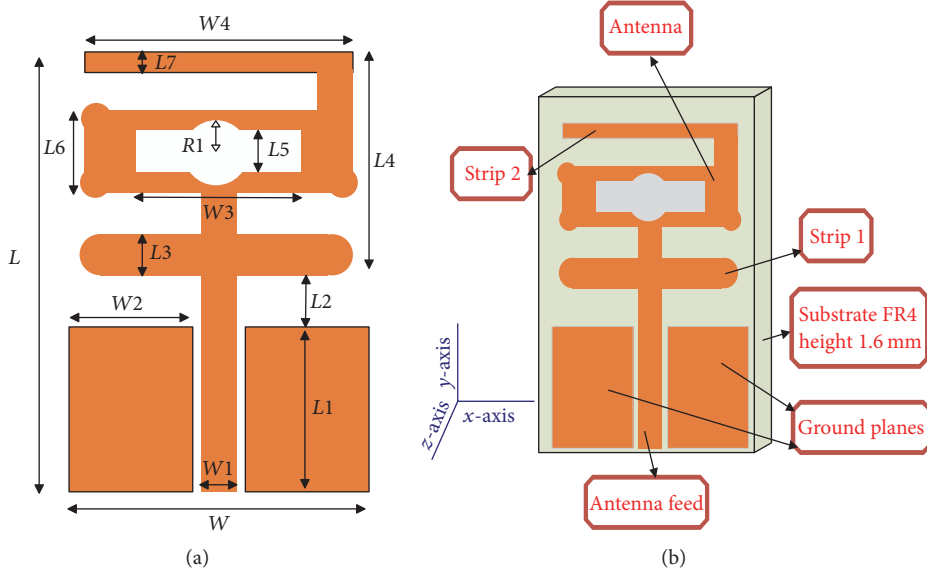


FIGURE 2: Geometry of the proposed antenna: (a) parametric details and (b) major components of proposed antenna.

TABLE 2: Proposed CPW antenna design parameters values.

Parameter	L	W	$L1$	$W1$	$L2$	$W2$	$L3$	$W3$
Value/mm	35	25	14.8	2	3.7	10.5	2	13
Parameter	$L4$	$W4$	$L5$	$L6$	$R1$	$L7$	h	g
Value/mm	14.3	17	3	7	2.5	0.5	1.6	1

for first and second resonance bands using the following expressions for coplanar waveguide design.

$$L4 = \frac{c}{4f_{\min} \sqrt{\epsilon_{r,\text{eff}}}} \quad (1)$$

$$L2 = \frac{c}{4f_{\max} \sqrt{\epsilon_{r,\text{eff}}}} \quad (2)$$

$$f1 = \frac{c}{4Y_g \sqrt{\epsilon_{r,\text{eff}}}} \quad (3)$$

$$\epsilon_{r,\text{eff}} = \frac{\epsilon_r + 1}{2}, \quad (4)$$

where “ c ” is the speed of light, $\epsilon_{r,\text{eff}}$ is the effective relative permittivity of substrate which is equal to 2.7, and “ Y_g ” is the guided wavelength which depends on the length of upper and lower strips for both bands. Characteristics impedance of the feed line having finite width ground planes on each side of FR4 substrate is given by Van Caekenbergh et al. [28].

$$Z_0 = \frac{30\pi}{2\sqrt{\epsilon_{r,\text{eff}}}} \frac{K(k)}{K(k')}, \quad (5)$$

where “ K ” is complete elliptic integral of first iteration and “ k ” and “ k' ” are CPW line dependent variables. These two parameters are calculated as follows:

$$k = \frac{c}{b} \sqrt{\frac{b^2 - a^2}{c^2 - a^2}} \quad (6)$$

$$k' = \sqrt{1 - k^2} = \frac{a}{b} \sqrt{\frac{c^2 - b^2}{c^2 - a^2}}.$$

Center frequencies f_1 and f_2 are calculated from (3) and optimized using Ansoft's High Frequency Structure Simulator (HFSS) software package.

The strip lengths $L4$ and $L2$ are optimized close to a quarter wavelength of center frequency considering f_{\min} around 2.1 GHz and f_{\max} at 3.6 GHz. The gap between the ground and feed elements “ g ” is 1 mm and the length of the feed line is 18.7 mm, while the radius of small rounded corners on the main antenna segment is 1.4 mm. The detailed antenna design parameters values are illustrated in Table 2. The gap between the one of the ground planes and feed line is optimized through simulation software to be 1 mm. Band stop function is realized by adding overlapped rectangular and circular slot in the main rectangular radiator. This reduces

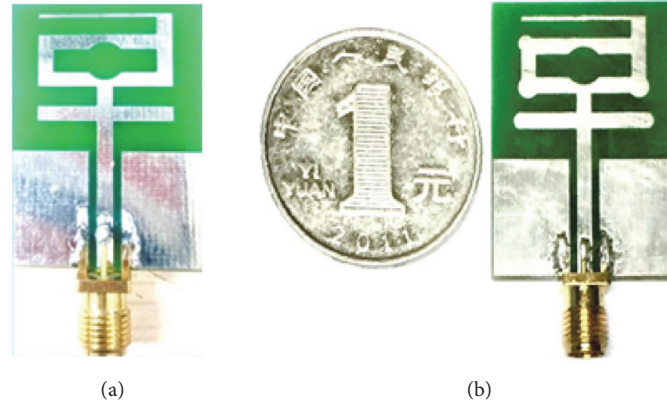


FIGURE 3: Fabricated antenna prototypes of (a) evolved antenna design and (b) proposed CPW antenna.

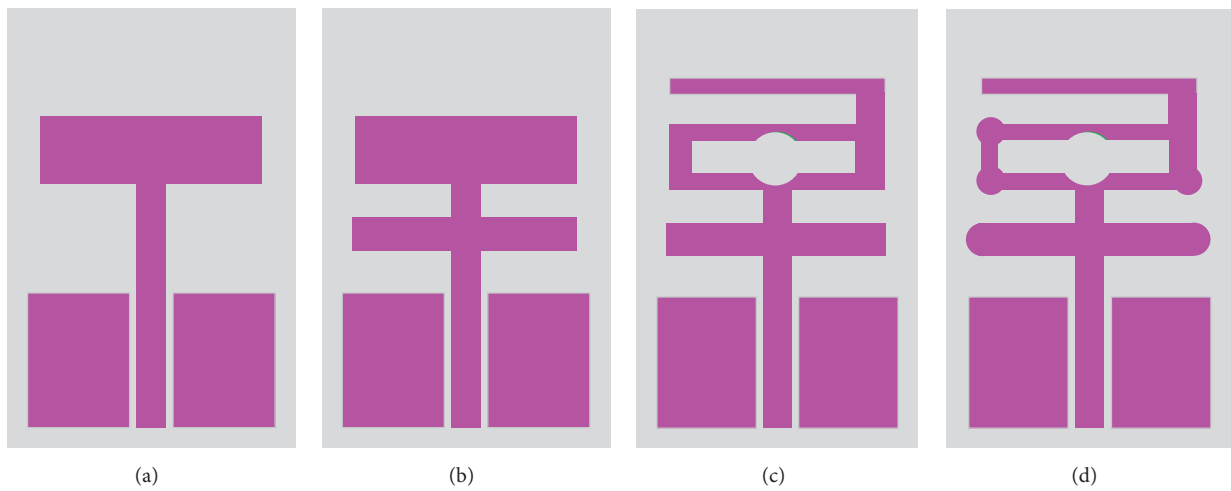


FIGURE 4: Evolution process of antenna: (a) Antenna 1, (b) Antenna 2, (c) Antenna 3, and (d) final proposed antenna.

the interference and creates notched frequencies between 2.4 GHz and 3.4 GHz bands. Similar kind of reactively loaded CPW antenna in [29] shows promising results with y-shaped and u-shaped slots in rectangular patch. In literature, various shapes of the slots are used to enhance the bandwidth of CPW designs including square wavelength line slot, fractal shaped slots, asymmetrical CPW slots, and circular slots [25–27, 29–32]. Square shaped slot implemented in [33] showed ultrawideband bandwidth and reduced overall antenna size effectively.

The method of overlapped symmetrical rectangular and circular slots is embedded in our proposed antenna to reduce interference of adjacent frequency bands to obtain efficient antenna parameters. To determine a good impedance matching, the electrical wavelength of the top and bottom strips is kept close to the quarter wavelength along with wideband microstrip coplanar strip line to couple the electromagnetic energy for better radiation efficiency. Similar kinds of small slit loaded antennas in [31, 32, 34] use series inductive slits and rectangular and circular shaped slots for impedance bandwidth improvement. Through iterative simulations, it is experienced that wider overlapped circular and rectangular

slots are more productive in widening the impedance bandwidth and improving antenna gain.

3. Antenna Performance

The fabricated prototypes of the two final designs are shown in Figure 3. The simulations are performed in Ansoft's HFSS and the reflection coefficients of the proposed antenna are measured using a Vector Network Analyzer (E5072A). An SMA connector is carefully coupled with ground and feed structures to obtain measurements.

3.1. Antenna Evolution. The evolution process of final antenna is shown in Figures 4(a)–4(d). Simulated reflection coefficient results for all antenna design steps/types are depicted in Figure 5. The antenna design process is started from a coplanar waveguide fed printed antenna by attaching a rectangular patch with feed line that attains a very broad fractional impedance bandwidth of more than 100% (1.1 GHz–3.9) GHz for $S_{11} < -10$ dB threshold without having second resonant band. However, our design goal is to make a dual-band antenna in which each band tuned/modified

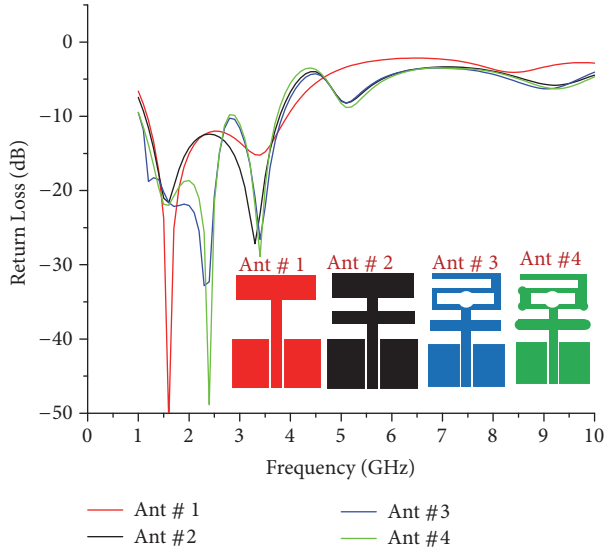


FIGURE 5: Simulated reflection coefficients of the four antennas.

comparatively independently without significantly affecting the other band as per our design needs. The 2nd design goal is to increase the gain of the antenna as CPW-fed printed antennas are generally omnidirectional antennas. In order to achieve these design goals, Antenna 1 is modified by adding an additional rectangular strip that creates a second resonance around 3.4 GHz as shown in Figure 4(b). Antenna 3 is created by adding another top strip and etching overlapped slots in first rectangular patch that shows first resonance at 2.4 GHz with impedance bandwidth from 1.0 GHz to 2.7 GHz and a second resonance at 3.4 GHz with impedance bandwidth from around 3.1 GHz to 3.7 GHz. Finally, Antenna 4 (proposed) is simulated and fabricated with imbedded rounded corners technique for improved performance in terms of reflection coefficient and gain. This design attains dual bands with a simulated result of around 80% fractional bandwidth (1.1 GHz–2.8 GHz) in the first band and around 23% fractional impedance bandwidth (3.0 GHz–3.75 GHz) in the second resonance band. This is worth mentioning that S_{11} has shown better notched frequency characteristic between the two bands. On the other hand, it is noted that introducing rounded corners has a very low effect on the resonant frequencies, but it has effectively improved the fractional impedance bandwidth and the gain of the final antenna design. Detailed parametric studies have been carried out including all the major lengths, widths, feed lines, and positions of rectangular strips to achieve higher gain of the proposed design.

3.2. Current Distribution and Impedance Matching Analysis.

Figure 6 shows the current distribution on the antenna at 2.4 GHz and 3.4 GHz to get a better insight of the antenna design which depicts that the current varies along the antenna x -axis dimension with minimum current at the ends due to the reduced “end effect.” As a matter of fact antenna radiates energy because of radiation resistance. Loss resistance of the antenna is small compared to radiation resistance that is

usually considered negligible in measurements. Input pulse and corresponding electric field intensity are calculated by the following expression:

$$FF = \frac{\max}{\tau} \left\{ \frac{\int S_T(t) S_R(t - \tau) dt}{\sqrt{S_T^2(t) dt} \sqrt{S_R^2(t) dt}} \right\}, \quad (7)$$

where “ S_T ” is the input signal and “ S_R ” is the received signal in the antenna far-field. Using Ansoft’s HFSS, full-wave time domain results are studied. Maximum current at top strip is obtained on both frequencies which have 90-degree phase shift that justifies the inductance of top cladding strip. The rounded corner concept serves well as it reflected more and more energy to the metal strips at resonant bands. Nevertheless, consistent large current density is concentrated on top strip for both frequency bands as common characteristics.

Figure 7 show the real and imaginary components of the input impedance of final two designs. Rounded corners model is tightly aligned to 50 Ω line in real part and has less tolerance in case of imaginary part. Overall better impedance matching is achieved by rounded corners design for both first and second resonance bands.

3.3. Results and Parametric Study. Figure 8 shows the simulated and measured results of reflection coefficients S_{11} [dB] versus frequency of the final proposed CPW antenna. It is shown that the antenna covers two ultrawide bands which include 1.1 GHz–2.7 GHz and 3.15–3.65 GHz, thus covering 2.4 GHz Bluetooth/Wi-Fi band (IEEE 802.11, 2.4–2.48 GHz) and most of the bands of 3G, 4G such as IEEE 802.15.4 (2.5–2.69 GHz, 3.4–3.69 GHz), WiMAX (IEEE 802.16), Zig-Bee (IEEE 802.15.4), DCS (1800), PCS (1900 MHz), Extended IMT (2100 MHz), and LTE (1700, 1900 MHz), and a future expected 5G band, that is, 3.4–3.6 GHz. There is generally a good agreement between simulated and measured results where differences between simulated and measured results can be attributed to factors such as small antenna size, SMA connector quality, soldering effect, and uncertainties in substrate dielectric constant. Major rectangular/circular slot size and lengths/widths of both top and bottom strips are optimized during designing process. The effects of variations in the width of bottom strip on the reflection coefficient S_{11} are plotted in Figure 9. It is experienced that the first resonance frequency increases with the decrease in the width of bottom strip and has negligible effect on second band, while variation of top strip controls the 3.4 GHz resonance frequency (second resonance band) that makes it simple and easy to reconfigure design for other adjacent frequencies if needed. The gains of the antennas with and without rounded edges/circular slot in dB versus frequency are shown in Figure 10. Comparing Antenna 3 and Antenna 4, the value of peak gain is subsequently improved from 6.2 dB to 8.9 dB. This shows that the gain is reasonably increased when the bottom strip edges are rounded and circular slot are overlapped on some of the corners of the upper strip which depicts the variation in gain between 6.2 dB and 8.9 dB in the range of interest.

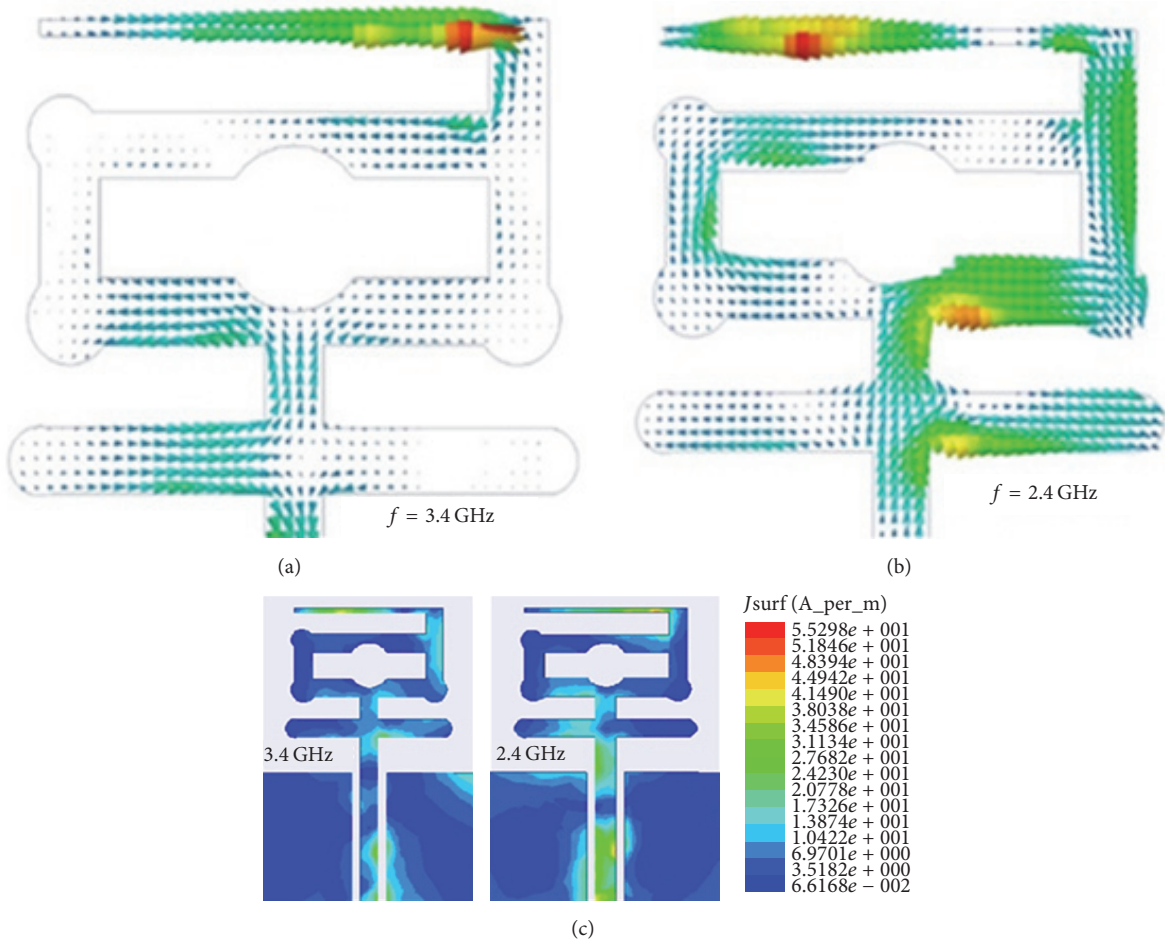


FIGURE 6: Current distribution on the proposed antenna: (a) vector current distribution at 3.4 GHz, (b) Vector current distribution at 2.4 GHz, and (c) Current densities at 2.4 GHz and 3.4 GHz.

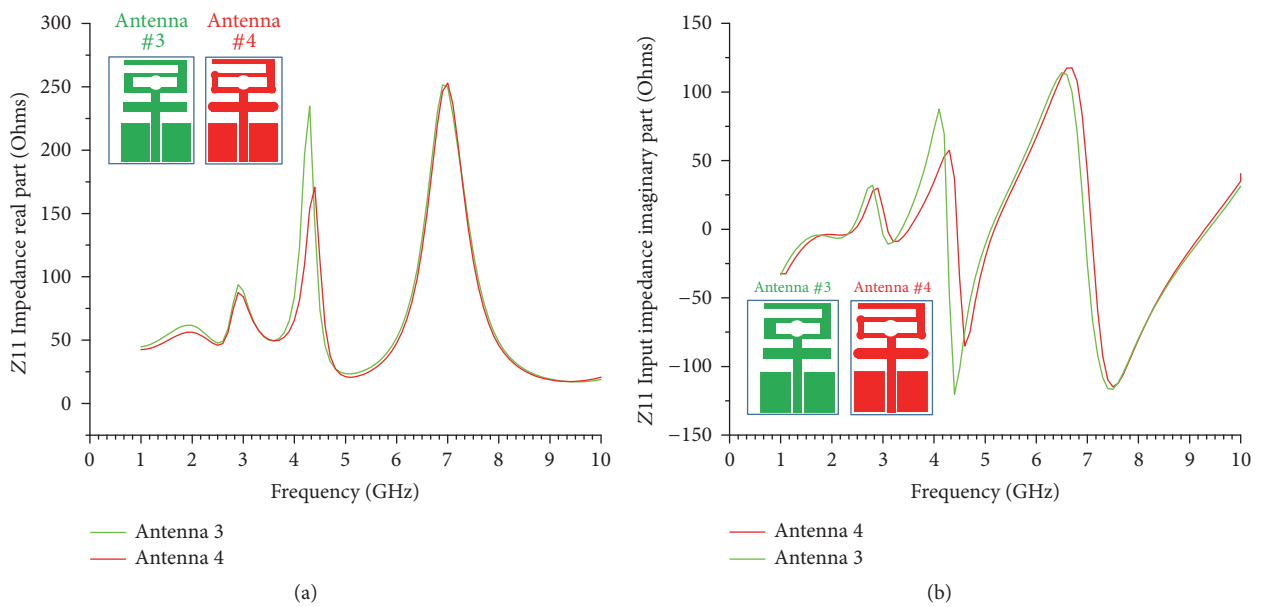


FIGURE 7: Input impedance of the final two designs: (a) real part (b) imaginary part.

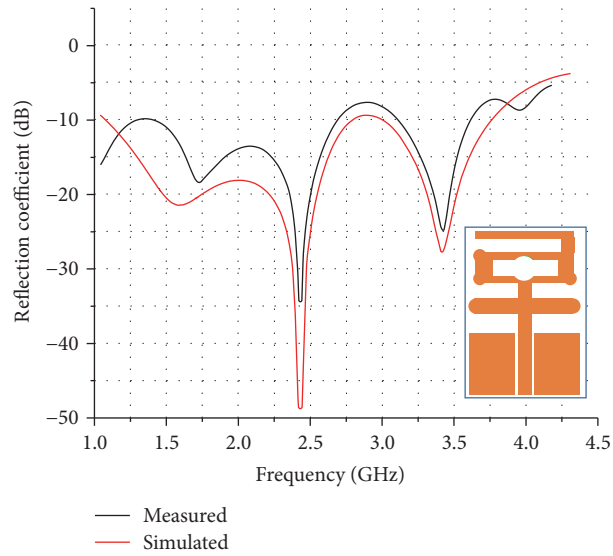


FIGURE 8: The simulated and measured reflection coefficients S_{11} [dB] versus frequency [GHz] of the proposed antenna.

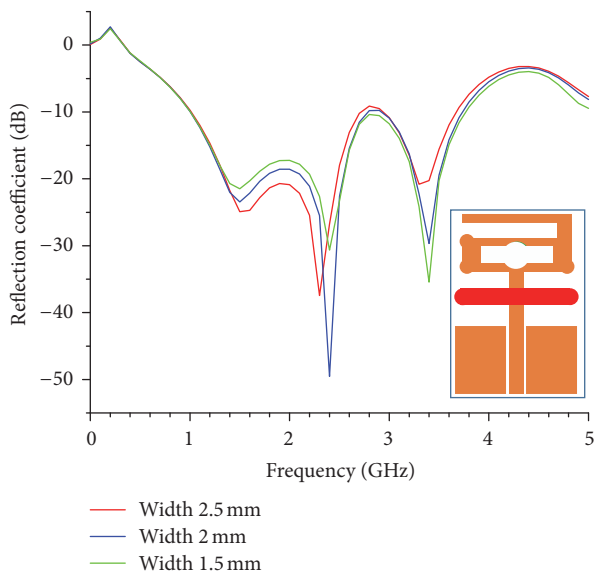


FIGURE 9: Reflection coefficient S_{11} in [dB] versus frequency in GHz for variations in the width of the lower strip.

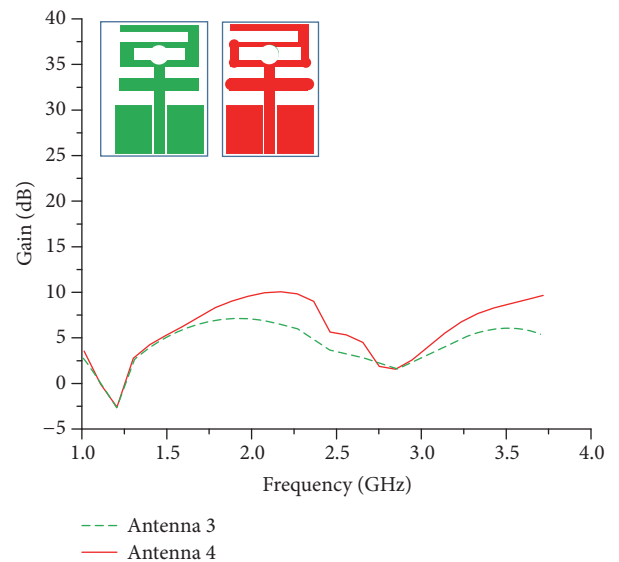


FIGURE 10: The gains of the antennas with and without the rounded edges/circular slot in dB versus frequency in GHz.

The radiation patterns of this dual-band antenna at first and second resonance bands are illustrated in Figure 11 for both E - and H -planes. High order modes are responsible to generate distribution effect at higher frequencies. It is clearly evident from the 2D patterns that the antenna performs as a directional radiator at E -plane and quite close to bidirectional in H -plane. These characteristics make this novel design a strong candidate and effectively suitable for profound Internet of Things (IoT) applications.

4. Conclusion

In this article, a novel rectangular shape CPW antenna with overlapped circular slots and rounded edges is proposed

and implemented. Top strip and bottom strips effectively control 2.4 GHz and 3.4 GHz resonance bands. Rounded corners technique is used to attain ultrawide bandwidth of 1.1 GHz–2.71 GHz at first resonance band and 3.15–3.65 GHz for second resonance band and to improve antenna gain. Each of these bands can be individually tuned through variation of top and bottom strip dimensions. The proposed antenna shows directional radiation pattern, good return loss, and better gain with acceptable radiation efficiency. The proposed design is very small in size (875 mm^2) which makes it a suitable contender for different portable and handheld IoT applications.

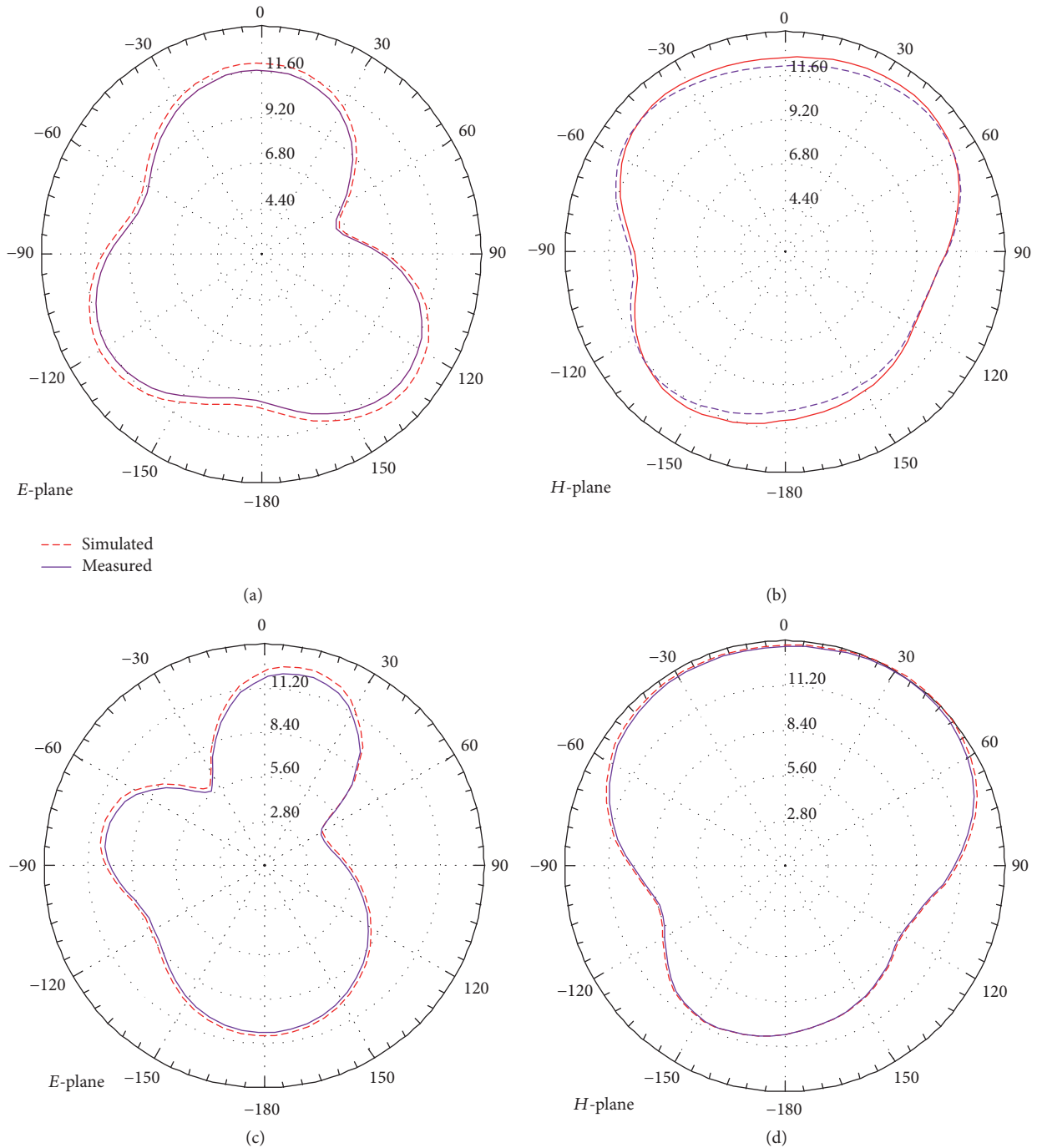


FIGURE 11: 2D radiation patterns of the proposed antenna: (a) *E*-plane at 2.4 GHz, (b) *H*-plane at 2.4 GHz, (c) *E*-plane at 3.4 GHz, and (d) *H*-plane at 3.4 GHz.

Conflicts of Interest

The authors declare that there are no conflicts of interest regarding the publication of this paper.

References

- [1] D. Acharjya and M. K. Geetha, "Internet of Things: Novel Advances and Envisioned Applications," in *Internet of Things: Novel Advances and Envisioned Applications*, Springer, 2017.
- [2] S. C. Mukhopadhyay and N. K. Suryadevara, "Internet of things: Challenges and opportunities," *Smart Sensors, Measurement and Instrumentation*, vol. 9, pp. 1–17, 2014.
- [3] G. J. Jo, S. M. Mun, D. S. Im, G. R. Kim, Y. G. Choi, and J. H. Yoon, "Novel design of a CPW-FED monopole antenna with three arc-shaped strips for WLAN/WiMAX operations," *Microwave and Optical Technology Letters*, vol. 57, no. 2, pp. 268–273, 2015.
- [4] A. Z. Manouare, S. Ibnyaich, A. El Idrissi, and A. Ghammaz, "Miniaturized triple wideband CPW-fed patch antenna with a

- defected ground structure for WLAN/WiMAX applications,” *Journal of Microwaves, Optoelectronics and Electromagnetic Applications*, vol. 15, no. 3, pp. 157–169, 2016.
- [5] T. Naeem, F. A. Tahir, and A. I. Najam, “UWB antenna with notches at WLAN bands,” in *Proceedings of the 11th International Conference on Frontiers of Information Technology, FIT 2013*, pp. 172–176, Pakistan, December 2013.
 - [6] S. Ahmed, F. A. Tahir, A. Shamim, and H. M. Cheema, “A compact kapton-based inkjet-printed multiband antenna for flexible wireless devices,” *IEEE Antennas and Wireless Propagation Letters*, vol. 14, pp. 1802–1805, 2015.
 - [7] A. Moradhesari, M. Naser-Moghadasi, and F. G. Gharakhili, “Design of compact CPW-FED monopole antenna for WLAN/WiMAX applications using a pair of F-shaped slits on the patch,” *Microwave and Optical Technology Letters*, vol. 55, no. 10, pp. 2337–2340, 2013.
 - [8] V. A. Shameena, S. Mridula, A. Pradeep, S. Jacob, A. O. Lindo, and P. Mohanan, “A compact CPW fed slot antenna for ultra wide band applications,” *AEU - International Journal of Electronics and Communications*, vol. 66, no. 3, pp. 189–194, 2012.
 - [9] T. H. Kim and D. C. Park, “CPW-fed compact monopole antenna for dual-band WLAN applications,” *IEEE Electronics Letters*, vol. 41, no. 6, pp. 291–293, 2005.
 - [10] J. H. Yoon, “Fabrication and measurement of rectangular ring with open-ended CPW-fed monopole antenna for 2.4/5.2-GHz WLAN operation,” *Microwave and Optical Technology Letters*, vol. 48, no. 8, pp. 1480–1483, 2006.
 - [11] L. Chen, Y.-F. Liu, and X.-L. Ma, “Compact ACS-Fed circular-ARC-shaped stepped monopole antenna for tri-band WLAN/WiMAX applications,” *Progress in Electromagnetics Research C*, vol. 51, pp. 131–137, 2014.
 - [12] L. Chen, Y.-L. Luo, and Y. Zhang, “Compact tri-band planar monopole antenna with ACS-fed structure,” *Progress in Electromagnetics Research Letters*, vol. 49, pp. 45–51, 2014.
 - [13] V. Deepu, R. Sujith, S. Mridula, C. K. Aanandan, K. Vasudevan, and P. Mohanan, “ACS FED printed F-shaped uniplanar antenna for dual band WLAN applications,” *Microwave and Optical Technology Letters*, vol. 51, no. 8, pp. 1852–1856, 2009.
 - [14] B. Li, Z. Yan, and T. Zhang, “Triple-band slot antenna with U-shaped open stub fed by asymmetric coplanar strip for WLAN/WiMAX applications,” *Progress in Electromagnetics Research Letters*, vol. 37, pp. 123–131, 2013.
 - [15] X. Li, X.-W. Shi, W. Hu, P. Fei, and J.-F. Yu, “Compact triband ACS-Fed monopole antenna employing open-ended slots for wireless communication,” *IEEE Antennas and Wireless Propagation Letters*, vol. 12, pp. 388–391, 2013.
 - [16] Y. Li, W. Li, and R. Mittra, “A compact ACS-FED dual-band meandered monopole antenna for WLAN and WiMAX applications,” *Microwave and Optical Technology Letters*, vol. 55, no. 10, pp. 2370–2373, 2013.
 - [17] Y.-F. Liu, P. Wang, and H. Qin, “A compact triband ACS-fed monopole antenna employing inverted-L branches for WLAN/WiMAX applications,” *Progress in Electromagnetics Research C*, vol. 47, pp. 131–138, 2014.
 - [18] P. V. Naidu and R. Kumar, “Design of a compact ACS-Fed dual band antenna for bluetooth/WLAN and WiMAX applications,” *Progress in Electromagnetics Research C*, vol. 55, pp. 63–72, 2014.
 - [19] Y. Song, Y. C. Jiao, X. M. Wang, Z. B. Weng, and F. S. Zhang, “Compact coplanar slot antenna fed by asymmetric coplanar strip for 2.4/5 GHz WLAN operations,” *Microwave and Optical Technology Letters*, vol. 50, no. 12, pp. 3080–3083, 2008.
 - [20] X. L. Sun, S. W. Cheung, and T. I. Yuk, “A compact monopole antenna for WLAN applications,” *Microwave and Optical Technology Letters*, vol. 56, no. 2, pp. 469–475, 2014.
 - [21] C.-K. Ham, J.-W. Baik, and Y.-S. Kim, “CPW-FED compact meander and L-shape monopole antenna for dual-band WLAN applications,” *Microwave and Optical Technology Letters*, vol. 50, no. 12, pp. 3147–3149, 2008.
 - [22] I. Zahraoui, J. Zbitou, A. Errkik et al., “A novel design of a low cost CPW fed multiband printed antenna,” *Lecture Notes in Electrical Engineering*, vol. 380, pp. 3–8, 2016.
 - [23] S. Ashok Kumar, T. Shanmugantham, and D. Dileepan, “Design and development of CPW fed monopole antenna at 2.45 GHz and 5.5 GHz for wireless applications,” *Alexandria Engineering Journal*, vol. 56, no. 2, pp. 231–234, 2017.
 - [24] Y. M. Madany and H. Elkamchouchi, “Analysis of high gain multiband rounded corners dashed rectangular spiral microstrip patch antenna,” in *Proceedings of the 2005 IEEE Antennas and Propagation Society International Symposium and USNC/URSI Meeting*, pp. 313–316, USA, July 2005.
 - [25] P. V. Naidu and R. Kumar, “A very small asymmetric coplanar strip fed multi-band antenna for wireless communication applications,” *Microsystem Technologies*, vol. 22, no. 9, pp. 2193–2200, 2016.
 - [26] S. W. Qu and C. L. Ruan, “Effect of round corners on bowtie antennas,” *Progress in Electromagnetics Research*, vol. 57, pp. 179–195, 2006.
 - [27] J. J. Tiang, M. T. Islam, N. Misran, and J. S. Mandeep, “A rounded corner triangular patch antenna for dual-frequency application,” *Microwave and Optical Technology Letters*, vol. 56, no. 1, pp. 69–72, 2014.
 - [28] K. Van Caekenberghe, N. Behdad, K. M. Brakora, and K. Sarabandi, “A 2.45-GHz electrically small slot antenna,” *IEEE Antennas and Wireless Propagation Letters*, vol. 7, pp. 346–348, 2008.
 - [29] P. K. Bharti, H. Singh, G. Pandey, and M. Meshram, “Slot loaded microstrip antenna for GPS, Wi-Fi, and WiMAX applications survey,” *International Journal of Microwaves Applications*, vol. 2, 2013.
 - [30] K. Vyas, G. Sanyal, A. K. Sharma, and P. K. Singhal, “Gain enhancement over a wideband in CPW-fed compact circular patch antenna,” *International Journal of Microwave and Wireless Technologies*, vol. 6, no. 5, pp. 497–503, 2014.
 - [31] S. I. Latif, L. Shafai, and S. K. Sharma, “Bandwidth enhancement and size reduction of microstrip slot antennas,” *IEEE Transactions on Antennas and Propagation*, vol. 53, no. 3, pp. 994–1003, 2005.
 - [32] P. V. Naidu, “Design, Simulation of a Compact Triangular Shaped Dual-Band Microstrip Antenna for 2.4 GHz Bluetooth/WLAN and UWB Applications,” *Wireless Personal Communications*, vol. 95, no. 2, pp. 783–794, 2017.
 - [33] M. M. M. Rahman, *Design and performance analysis of u-slot, y-slot and uy slot microstrip patch antenna for wireless applications*, Daffodil International University, 2016.
 - [34] M. Kumar and K. Ray, “Design and Performance of a compact broadband circularly polarized rectangular ring antenna,” *International Journal of Electromagnetics and Applications*, vol. 4, pp. 49–55.

Research Article

Effect of Randomness in Element Position on Performance of Communication Array Antennas in Internet of Things

Congsi Wang ^{1,2}, Yan Wang ¹, Xiaodong Yang ³, Wei Gao,² Chao Jiang,⁴ Lu Wang,⁵ Yiqun Zhang,⁶ and Meng Wang ⁷

¹Key Laboratory of Electronic Equipment Structure Design, Ministry of Education, Xidian University, Xi'an 710071, China

²School of Civil and Environmental Engineering, University of New South Wales, Sydney, NSW 2052, Australia

³School of Electronic Engineering, Xidian University, Xi'an 710071, China

⁴State Key Laboratory of Advanced Design and Manufacturing for Vehicle Body, College of Mechanical and Vehicle Engineering, Hunan University, Changsha 410082, China

⁵CETC No. 38 Research Institute, Hefei 230088, China

⁶Nanjing Research Institute of Electronics Technology, Nanjing 210039, China

⁷Research Institute of Shaanxi Huanghe Group Co., Ltd., Xi'an 710043, China

Correspondence should be addressed to Yan Wang; wangyan5169@163.com

Received 30 October 2017; Revised 7 January 2018; Accepted 29 January 2018; Published 21 March 2018

Academic Editor: Hassan T. Chattha

Copyright © 2018 Congsi Wang et al. This is an open access article distributed under the Creative Commons Attribution License, which permits unrestricted use, distribution, and reproduction in any medium, provided the original work is properly cited.

As a critical component for wireless communication, active phased array antennas face the restrictions of creating effective performance with the effect of randomness in the position of the array element, which are inevitably produced in the manufacturing and operating process of antenna. A new method for efficiently and effectively evaluating the statistic performance of antenna is presented, with consideration of randomness in element position. A coupled structural-electromagnetic statistic model for array antenna is proposed from the viewpoint of electromechanical coupling. Lastly, a 12×12 planar array is illustrated to evaluate the performance of antenna with the saddle-shaped distortion and random position error. The results show that the presented model can obtain the antenna performance quickly and effectively, providing an advantageous guidance for structural design and performance optimization for array antennas in wireless application.

1. Introduction

The application of wireless communication promotes the realization and development of physical things in our daily life exchanging information from a network, which is called the Internet of Things (IoT) [1–3]. In the wireless communication, the choice of antenna is a critical component. Active phased array antennas have such significant advantages, including rapid reconfiguration or revisit rate, multibeam, shaped beams, sidelobe control, and high reliability over other types of antennas, and there has been an increased interest in their use for a wide variety of communication and remote-sensing applications, such as serving as the ground station terminal to track the satellite for IOT data connection [4]. In the working process, however, the manufacturing and processing of the antenna, any movement of the carrier

platform, and the external environment load could lead to the structure errors, including both the random position error and systematic error. The combination of the random position error and systematic distortion finally results in the randomness in element position. Finally, the electromagnetic performance of array antenna could be degraded, such as the gain loss, sidelobe level (SLL) rising, beam width broadening, and pointing error [5–9]. As a result, the communication distance will be shortened and the resistance to interference will be reduced, which seriously restricts the realization of high performance of array antenna. The antenna faces the restrictions of creating effective performance under structure errors. Therefore, it is necessary to explore deeply the coupling relationship between structure error and electromagnetic performance for active phased array antenna with the effect of randomness in element position [10–12].

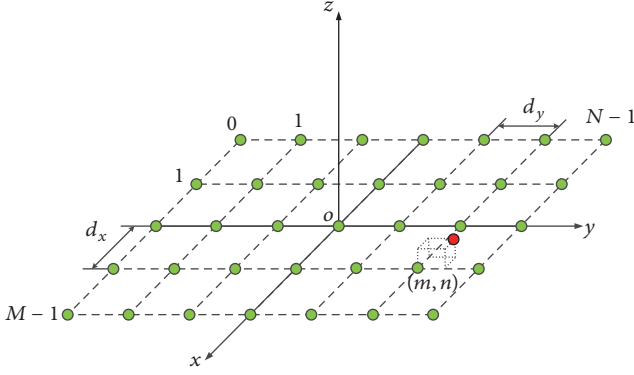


FIGURE 1: Element configuration of planar array antenna.

The present works for analyzing the effect of structure error on electromagnetic performance of array antenna are carried out mainly from the following three aspects. Firstly, assuming that the systematic distortion of antenna is a certain shape and that the influence of only systematic error on performance is analyzed, [13] studied the effect of symmetrical and unsymmetrical bend of array plane on the performance of planar antenna. Reference [14] discussed the influence of four array plane distortions including the sag, potato chip, and sinusoidal and Bessel character for array antenna. The above works in [13, 14] consider only the systematic error without considering the random position errors which are also produced inevitably during the manufacturing and working process. Secondly, some works are focusing on the analysis of the effect of random error uncertainty. Reference [15] explored the influence of random errors on the performance of hexagonal active phased array antenna and achieved some instructive conclusions. But there are no discussions on the systematic distortion. Furthermore, there is research indicating that the effect of random errors could be equivalent to the influence of excitation current errors, and the performances of antenna with random current errors are studied [16, 17]. However, there is lack of direct relationship of random position error with the antenna performance. In addition, [18] investigated the subarray position error and its influence on antenna performance by using the probability statistical theory. But the method requires lots of repeated calculations to get the statistical performance of antenna. Thirdly, some works introduced the linear combination of random error and systematic distortion to analyze their effect on antenna performance. In [19, 20], the sum of random error and systematic error was regarded as the structure error item, used to analyze the performance of distorted array antenna. However, in practice the degrees of random error and systematic error show great differences; the linear combination could mitigate the effect of random error when there is big difference between the degrees of random and systematic errors. Moreover, systematic error is supposed to be deterministic but random error is stochastic; the combination errors could result in the randomness of electromagnetic performance. So it is more accurate to estimate the electromagnetic performance from the perspective of statistic property when random error exists.

Therefore, this paper presents a new method for efficiently and effectively evaluating the statistic performance of active phased array antenna, with consideration of randomness in the position of the array element. A coupled structural-electromagnetic statistic model is proposed, from the viewpoint of electromechanical coupling. The method provides an advantageous guidance for structural design and performance optimization for array antennas in wireless application.

2. Coupled Structure-Electromagnetic Statistic Model with Randomness in Element Position

As shown in Figure 1, the array radiation elements are assembled with an equal interval, whose numbers are $M \times N$. The intervals of the array elements along x and y directions are d_x and d_y , respectively.

(θ, ϕ) is the direction of the far-field target relative to the coordinate system $Oxyz$ as shown in Figure 2, whose direction cosine is $(\cos \alpha_x, \cos \alpha_y, \cos \alpha_z)$ [21].

The manufacturing and working process of antenna lead to the structure errors, including the random error and systematic distortion. Suppose the random error of element (m, n) ($0 \leq m \leq M-1, 0 \leq n \leq N-1$) is $(\Delta x_{mn}^r, \Delta y_{mn}^r, \Delta z_{mn}^r)$; the phase difference $\Delta \Phi_{mn}^r$ in regard to the coordinate origin in Figure 1 is given as follows.

$$\Delta \Phi_{mn}^r = k (\Delta x_{mn}^r \sin \theta \cos \phi + \Delta y_{mn}^r \sin \theta \sin \phi + \Delta z_{mn}^r \cos \theta). \quad (1)$$

Next, suppose the systematic distortion of element (m, n) is $(\Delta x_{mn}^s, \Delta y_{mn}^s, \Delta z_{mn}^s)$; the phase difference $\Delta \Phi_{mn}^s$ in regard to the coordinate origin in Figure 1 is given as follows.

$$\Delta \Phi_{mn}^s = k (\Delta x_{mn}^s \sin \theta \cos \phi + \Delta y_{mn}^s \sin \theta \sin \phi + \Delta z_{mn}^s \cos \theta). \quad (2)$$

According to the superposition principle of the array antenna without element coupling, the filed density pattern function for planar rectangular active phased array antenna with systematic distortion and random position error is developed as follows.

$$E_{sr}(\theta, \phi) = f_e(\theta, \phi) \sum_{m=0}^{M-1} \sum_{n=0}^{N-1} I_{mn} \cdot e^{j(\Delta \Phi_{mn} + \Delta \Phi_{mn}^r + \Delta \Phi_{mn}^s + \varphi_{mnB})}, \quad (3)$$

where $f_e(\theta, \phi)$ is the pattern function of element in free space, I_{mn} is the amplitude of excitation current of element (m, n) , φ_{mnB} is the array's inherent phase difference determined by phase shifter, and $\Delta \Phi_{mn} = kmd_x \sin \theta \cos \phi + knd_y \sin \theta \sin \phi$ is the initial spatial phase distribution.

In practice, random position errors of elements are probabilistic variables; it is necessary to analyze the statistic property of electromagnetic performance for array antenna with random error included. Suppose the random position

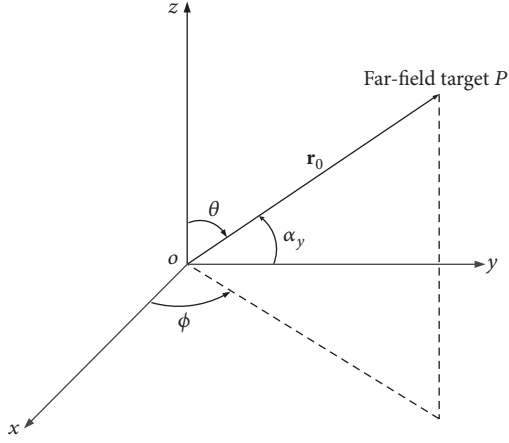


FIGURE 2: Space geometrical relationship of far-field target.

errors along x , y , and z directions are Δx_{mn}^r , Δy_{mn}^r , and Δz_{mn}^r , which are subjected to the normal distribution, with means of zero and variances of σ_x^2 , σ_y^2 , and σ_z^2 , respectively. Then phase difference $\Delta\Phi_{mn}^r$ in (1) is also normally distributed, and the variance is obtained as follows.

$$\sigma_{\Phi_r}^2 = k^2 \left[\sigma_x^2 (\sin \theta \cos \phi)^2 + \sigma_y^2 (\sin \theta \sin \phi)^2 + \sigma_z^2 (\cos \theta)^2 \right]. \quad (4)$$

For any random variable with normal distribution, expressed as $x \sim N(0, \sigma_x)$, the function relations $\overline{\cos x}$ and $\overline{\sin x}$ can be obtained from [22]. Applying the function relations, the mean of exponential function is $\overline{e^{jx}} = e^{-\sigma_x^2/2}$. Therefore, the mean of the field density pattern function $E_{sr}(\theta, \phi)$ in (3) is deduced as follows.

$$\begin{aligned} \overline{E_{sr}(\theta, \phi)} &= f_e(\theta, \phi) \sum_{m=0}^{M-1} \sum_{n=0}^{N-1} I_{mn} \cdot e^{j(\Delta\Phi_{mn} + \Delta\Phi_{mn}^s + \varphi_{mnB})} \cdot \overline{e^{j\Delta\Phi_{mn}^r}} \quad (5) \\ &= E_s(\theta, \phi) \cdot e^{-(1/2)\sigma_{\Phi_r}^2}, \end{aligned}$$

where $E_s(\theta, \phi)$ is the field density pattern function with only the systematic distortion existing.

Then the mean of the power pattern function for array antenna is deduced according to the property of variance $\sigma_{E_{sr}}^2 = \overline{E_{sr}(\theta, \phi) \cdot E_{sr}^*(\theta, \phi)} - \overline{E_{sr}(\theta, \phi)} \cdot \overline{E_{sr}^*(\theta, \phi)}$ as follows.

$$\begin{aligned} \overline{P_{sr}(\theta, \phi)} &= \overline{E_{sr}(\theta, \phi) \cdot E_{sr}^*(\theta, \phi)} \quad (6) \\ &= \sigma_{E_{sr}}^2 + \overline{E_{sr}(\theta, \phi)} \cdot \overline{E_{sr}^*(\theta, \phi)}. \end{aligned}$$

Substituting the function $\overline{E_{sr}(\theta, \phi)}$ into (6), the mean of power pattern function is expressed as follows.

$$\overline{P_{sr}(\theta, \phi)} = \sigma_{E_{sr}}^2 + |E_s(\theta, \phi)|^2 \cdot e^{-\sigma_{\Phi_r}^2}, \quad (7)$$

where $\sigma_{E_{sr}}^2$ is the variance of function $E_{sr}(\theta, \phi)$. The expression of the variance $\sigma_{E_{sr}}^2$ is presented as follows.

Firstly, as a vector quantity, $E_{sr}(\theta, \phi)$ can be represented as the combination of the real part and imaginary part [23]. Assume $X = \sum_{m=0}^{M-1} \sum_{n=0}^{N-1} X_{mn}$ and $Y = \sum_{m=0}^{M-1} \sum_{n=0}^{N-1} Y_{mn}$ are the real and imaginary parts, respectively. The expressions of X_{mn} and Y_{mn} are $X_{mn} = f_e(\theta, \phi) \cdot I_{mn} \cdot \cos(\Delta\Phi_{mn} + \Delta\Phi_{mn}^r + \Delta\Phi_{mn}^s + \varphi_{mnB})$ and $Y_{mn} = f_e(\theta, \phi) \cdot I_{mn} \cdot \sin(\Delta\Phi_{mn} + \Delta\Phi_{mn}^r + \Delta\Phi_{mn}^s + \varphi_{mnB})$, respectively.

Next, the variance $\sigma_{E_{sr}}^2$ is deduced as follows.

$$\sigma_{E_{sr}}^2 = \sigma_X^2 + \sigma_Y^2 = \sum_{m=0}^{M-1} \sum_{n=0}^{N-1} \sigma_{X_{mn}}^2 + \sum_{m=0}^{M-1} \sum_{n=0}^{N-1} \sigma_{Y_{mn}}^2, \quad (8)$$

where $\sigma_{X_{mn}}^2 = \overline{X_{mn}^2} - \overline{X_{mn}}^2$ and $\sigma_{Y_{mn}}^2 = \overline{Y_{mn}^2} - \overline{Y_{mn}}^2$.

Since the function $\overline{\cos(\Delta\Phi_{mn} + \Delta\Phi_{mn}^r + \Delta\Phi_{mn}^s + \varphi_{mnB})}$ is equal to $\overline{\cos(\Delta\Phi_{mn} + \Delta\Phi_{mn}^s + \varphi_{mnB})} e^{-(1/2)\sigma_{\Phi_r}^2}$, then

$$\begin{aligned} \overline{X_{mn}} &= f_e(\theta, \phi) \cdot I_{mn} \\ &\quad \cdot \overline{\cos(\Delta\Phi_{mn} + \Delta\Phi_{mn}^s + \varphi_{mnB})} e^{-(1/2)\sigma_{\Phi_r}^2} \quad (9) \\ \overline{X_{mn}^2} &= |f_e(\theta, \phi)|^2 \cdot I_{mn}^2 \\ &\quad \cdot \overline{\frac{1 + \cos(2\Delta\Phi_{mn} + 2\Delta\Phi_{mn}^s + 2\varphi_{mnB})}{2}} e^{-2\sigma_{\Phi_r}^2}. \end{aligned}$$

Therefore, the variance $\sigma_{X_{mn}}^2$ is deduced as follows.

$$\begin{aligned} \sigma_{X_{mn}}^2 &= |f_e(\theta, \phi)|^2 \cdot I_{mn}^2 \\ &\quad \cdot \left(\frac{1 + \cos(2\Delta\Phi_{mn} + 2\Delta\Phi_{mn}^s + 2\varphi_{mnB})}{2} e^{-2\sigma_{\Phi_r}^2} \right. \quad (10) \\ &\quad \left. - \frac{1 + \cos(2\Delta\Phi_{mn} + 2\Delta\Phi_{mn}^s + 2\varphi_{mnB})}{2} e^{-\sigma_{\Phi_r}^2} \right). \end{aligned}$$

Since the function $\overline{\sin(\Delta\Phi_{mn} + \Delta\Phi_{mn}^r + \Delta\Phi_{mn}^s + \varphi_{mnB})}$ is equal to $\overline{\sin(\Delta\Phi_{mn} + \Delta\Phi_{mn}^s + \varphi_{mnB})} e^{-(1/2)\sigma_{\Phi_r}^2}$, then

$$\begin{aligned} \overline{Y_{mn}} &= f_e(\theta, \phi) \cdot I_{mn} \cdot \overline{\sin(2\Delta\Phi_{mn} + 2\Delta\Phi_{mn}^s + 2\varphi_{mnB})} \\ &\quad \cdot e^{-(1/2)\sigma_{\Phi_r}^2} \quad (11) \end{aligned}$$

$$\begin{aligned} \overline{Y_{mn}^2} &= |f_e(\theta, \phi)|^2 \cdot I_{mn}^2 \\ &\quad \cdot \overline{\frac{1 - \cos(2\Delta\Phi_{mn} + 2\Delta\Phi_{mn}^s + 2\varphi_{mnB})}{2}} e^{-2\sigma_{\Phi_r}^2} \quad (12) \end{aligned}$$

$$\sigma_{Y_{mn}}^2 = |f_e(\theta, \phi)|^2 I_{mn}^2 \cdot \left(\frac{1 - \cos(2\Delta\Phi_{mn} + 2\Delta\Phi_{mn}^s + 2\varphi_{mnB}) e^{-2\sigma_{\phi_r}^2}}{2} - \frac{1 - \cos(2\Delta\Phi_{mn} + 2\Delta\Phi_{mn}^s + 2\varphi_{mnB}) e^{-\sigma_{\phi_r}^2}}{2} \right). \quad (13)$$

The variance $\sigma_{E_{sr}}^2$ then is deduced by substituting (10) and (13) into (8) as follows.

$$\begin{aligned} \sigma_{E_{sr}}^2 &= \sum_{m=0}^{M-1} \sum_{n=0}^{N-1} \sigma_{X_{mn}}^2 + \sum_{m=0}^{M-1} \sum_{n=0}^{N-1} \sigma_{Y_{mn}}^2 \\ &= |f_e(\theta, \phi)|^2 \left(1 - e^{-\sigma_{\phi_r}^2} \right) \sum_{m=0}^{M-1} \sum_{n=0}^{N-1} I_{mn}^2. \end{aligned} \quad (14)$$

Finally, the mean of power pattern function with randomness in element position, which is also called the coupled structure-electromagnetic statistic model, is developed as follows.

$$\begin{aligned} \overline{P_{sr}(\theta, \phi)} &= |E_s(\theta, \phi)|^2 e^{-\sigma_{\phi_r}^2} + |f_e(\theta, \phi)|^2 \left(1 - e^{-\sigma_{\phi_r}^2} \right) \\ &\cdot \sum_{m=0}^{M-1} \sum_{n=0}^{N-1} I_{mn}^2 = |E_s(\theta, \phi)|^2 \\ &\cdot e^{-k^2[\sigma_x^2(\sin\theta\cos\phi)^2 + \sigma_y^2(\sin\theta\sin\phi)^2 + \sigma_z^2(\cos\theta)^2]} \\ &+ |f_e(\theta, \phi)|^2 \\ &\cdot \left\{ 1 - e^{-k^2[\sigma_x^2(\sin\theta\cos\phi)^2 + \sigma_y^2(\sin\theta\sin\phi)^2 + \sigma_z^2(\cos\theta)^2]} \right\} \\ &\cdot \sum_{m=0}^{M-1} \sum_{n=0}^{N-1} I_{mn}^2. \end{aligned} \quad (15)$$

3. Verification of Coupled Structure-Electromagnetic Statistic Model

In order to illustrate the effectiveness of the developed model, the coupled structure-electromagnetic statistic model is verified by simulations with HFSS software, which can provide stable and accurate solutions at even high frequencies and has been widely used by engineers to design reliable products [24].

In consideration of the array antennas in wireless applications, an 8×8 patch array antenna is illustrated [25], with the intervals along x and y directions being both 0.75λ , as shown in Figure 3. The frequency of the patch array antenna is 30 GHz. The physical size of the patch array antenna is $60 \text{ mm} \times 60 \text{ mm}$. For each patch antenna, the length and width are $L = 3.953 \text{ mm}$ and $W = 3.160 \text{ mm}$, respectively. The initial excitation current is equal in amplitude and phase. Saddle-shaped distortion with the maximum displacement in z direction of $\lambda/6$ is assumed as the systematic distortion, and the random position errors in x , y , and z directions are all

TABLE 1: Parameters of HFSS-based and coupled model-based results.

Performance	HFSS-based result	Coupled model-based result
Gain/dB	60.12	60.12
First SLL/dB		
in $\phi = 0^\circ$ plane	50.17	50.17
in $\phi = 90^\circ$ plane	49.87	49.96
Second SLL/dB		
in $\phi = 0^\circ$ plane	44.15	44.52
in $\phi = 90^\circ$ plane	43.88	44.07
Third SLL/dB		
in $\phi = 0^\circ$ plane	41.34	41.61
in $\phi = 90^\circ$ plane	40.28	40.61
Fourth SLL/dB		
in $\phi = 0^\circ$ plane	39.23	39.66
in $\phi = 90^\circ$ plane	37.46	37.85
Fifth SLL/dB		
in $\phi = 0^\circ$ plane	37.44	37.84
in $\phi = 90^\circ$ plane	33.71	34.19
Beam width/ $^\circ$		
in $\phi = 0^\circ$ plane	8.80	8.80
in $\phi = 90^\circ$ plane	8.79	8.79
Boresight pointing/ $^\circ$		
in $\phi = 0^\circ$ plane	0.15	0.15
in $\phi = 90^\circ$ plane	0.13	0.13

Note. Every SLL is the right SLL.

assumed to satisfy the normal distribution with mean of 0 and variance of $\lambda/30$.

Firstly, random samples of structure errors are generated by adding the specific saddle-shaped distortion with each random position error sample produced according to the normal distribution. Then the antenna performance with every structure error sample is simulated separately with HFSS software without consideration of element coupling. Lastly the mean of the antenna performance is calculated by averaging the sum of the performances obtained from all the structure error samples. Here simulations with 1000 structure error samples are taken because the mean of antenna performance with greater than 1000 samples results in no further change. The comparison with the performance calculated by the developed model is shown in Figure 4 and the corresponding parameters are listed in Table 1.

As shown in Figure 4 and Table 1, the coupled model-based and HFSS-based results show good consistency in both the main lobe area and sidelobe area. The gain, beam width, and boresight pointing are the same in both $\phi = 0^\circ$ and $\phi = 90^\circ$ planes, which indicate that the main lobe areas are the same obtained by the coupled model and HFSS, respectively. The differences of the first sidelobes in absolute values are 0 dB and 0.09 dB in $\phi = 0^\circ$ and $\phi = 90^\circ$ planes, respectively. For the second, third, fourth, and fifth sidelobes, the maximum differences in absolute values are 0.43 dB and

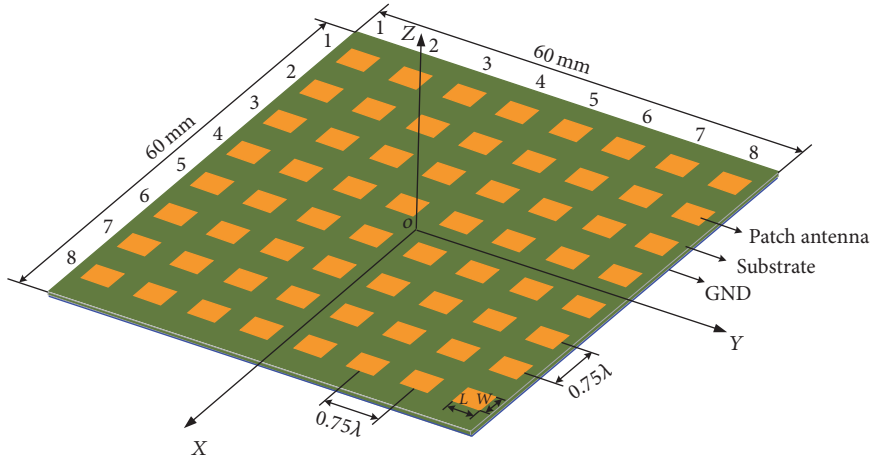


FIGURE 3: Patch array antenna model.

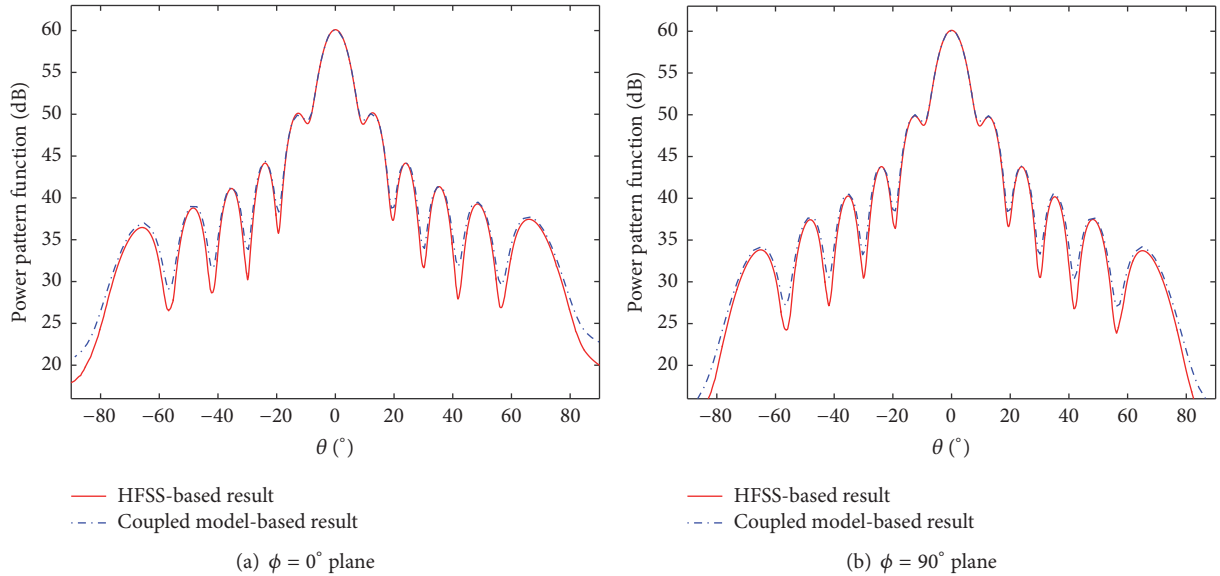


FIGURE 4: HFSS-based and coupled model-based results comparison.

0.48 dB in $\phi = 0^\circ$ and $\phi = 90^\circ$ planes, respectively. Therefore, the results above prove that the proposed coupled model is effective for analyzing the effect of randomness in element position on electromagnetic performance for array antennas.

4. Simulation and Discussion

For active phased array antenna, both the random position error and systematic distortion consist of the structure deformation for antenna in practice. Random position error appears as the random variable.

In engineering, the antenna array region is generally distorted into a representative saddle shape. Based on the mathematical features of the surface, the z -coordinate of the

phase centre of array element (m, n) in saddle shape is given as follows.

$$\Delta z_{mn} = \Delta z_{\max} \left(\frac{x_{mn}^2}{x_{\max}^2} - \frac{y_{mn}^2}{y_{\max}^2} \right), \quad (16)$$

where x_{\max} and y_{\max} are the half-length and width of the array aperture size, respectively, and Δz_{\max} is the maximum displacement of the array elements in z direction that belongs to the systematic error.

Therefore, the planar array antenna with both the saddle-shaped distortion and element random position error is discussed as follows. A 12×12 planar rectangular array is illustrated, with the intervals of array elements in x and y directions being both $\lambda/2$. The frequency is 9.375 GHz

TABLE 2: Parameters variations with systematic distortion and different random errors.

Performance	Random sample 1	Random sample 2	Random sample 3	Random sample 4	Statistic random error
Gain loss/dB	-2.00	-2.53	-1.89	-2.22	-2.23
First SLL change/dB					
in $\phi = 0^\circ$ plane	+0.40	+0.41	+0.56	+0.72	+0.53
in $\phi = 90^\circ$ plane	+1.65	+2.09	+0.64	+2.10	+1.53
Second SLL change/dB					
in $\phi = 0^\circ$ plane	-1.32	-0.14	-0.52	-0.39	-0.01
in $\phi = 90^\circ$ plane	-0.16	-1.47	+0.93	-1.40	-0.01
Third SLL change/dB					
in $\phi = 0^\circ$ plane	-4.91	+1.26	+0.63	+0.79	-0.31
in $\phi = 90^\circ$ plane	+0.28	+0.66	-1.40	+0.29	-0.31
Fourth SLL change/dB					
in $\phi = 0^\circ$ plane	-0.34	-5.45	+1.74	+0.59	-0.25
in $\phi = 90^\circ$ plane	+1.26	-0.52	-0.92	-1.25	-0.25
Fifth SLL change/dB					
in $\phi = 0^\circ$ plane	-0.54	+0.56	-0.87	-2.36	-0.09
in $\phi = 90^\circ$ plane	-2.89	+1.21	-2.81	-0.28	-0.09
Beam width change/ $^\circ$					
in $\phi = 0^\circ$ plane	+0.30	+0.34	+0.23	+0.28	+0.29
in $\phi = 90^\circ$ plane	+0.40	+0.34	+0.28	+0.34	+0.35
Boresight pointing/ $^\circ$					
in $\phi = 0^\circ$ plane	+0.34	-0.31	+0.12	-0.14	+0.28
in $\phi = 90^\circ$ plane	+0.33	+0.30	-0.31	+0.16	+0.19

Note. Every SLL is the right SLL, + indicates upgrade and right side of $\theta = 0^\circ$, and - indicates decrease and left side of $\theta = 0^\circ$.

and the initial excitation current is equal in amplitude and phase. After analysis suppose the random errors along x , y , and z directions are subjected to the normal distribution, with mean of zero and the same variance of $\lambda/20$, and the maximum displacement of the saddle shape in z direction is selected as $\lambda/5$. The presented statistic model is applied to evaluate the statistic performance of distorted array antenna. In addition, the comparison with the existing linearly combination of systematic distortion and different random distributions of random errors is also discussed, where the used power pattern function is $P_{sr}(\theta, \phi) = E_{sr}(\theta, \phi) \cdot E_{sr}^*(\theta, \phi)$ and $E_{sr}(\theta, \phi)$ is the field density in (3). The systematic distortion is taken as the same saddle shape. Meanwhile, four random samples from sample 1 to sample 4 are generated according to the same normal distribution, taken as the random errors along x , y , and z directions. The comparison results are shown in Figure 5 and the corresponding parameters are listed in Table 2.

As shown in Figure 5 and Table 2, it follows that

(1) the gain decreases greatly when saddle shape and random error coexist, with the maximum gain loss being -2.53 dB. The gain loss obtained from the statistic random error, which is directly substituting the variances of the random errors and systematic distortion into the presented

statistic model, shows a little difference from the values calculated by the four random samples, which are obtained by, respectively, adding each random sample with the systematic distortion as the whole structure error. The maximum difference is 0.34 dB, which indicates that the change of gain depends mainly on the systematic distortion.

(2) the sidelobe levels change differently with the four random samples in both $\phi = 0^\circ$ and $\phi = 90^\circ$ planes. From the first to the fifth sidelobe level, the maximum change is -5.45 dB, which indicates that the sidelobe level is closely related to the distribution of random error. Large performance errors will be produced when evaluating from any random distribution. Thus the effect of statistics of random error must be considered. The sidelobe levels from the statistic model could be regarded as the evaluation values for they are given from the mean of power pattern function.

(3) the beam width changes in small scales with different random samples, and the values are almost the same with the statistic random error. The maximum variations in $\phi = 0^\circ$ and $\phi = 90^\circ$ planes are 0.06° and 0.07° , respectively. It shows that the beam width is influenced mainly by the systematic distortion.

(4) for the saddle shape is symmetry without influence on the pointing direction, the boresight pointing changes mainly

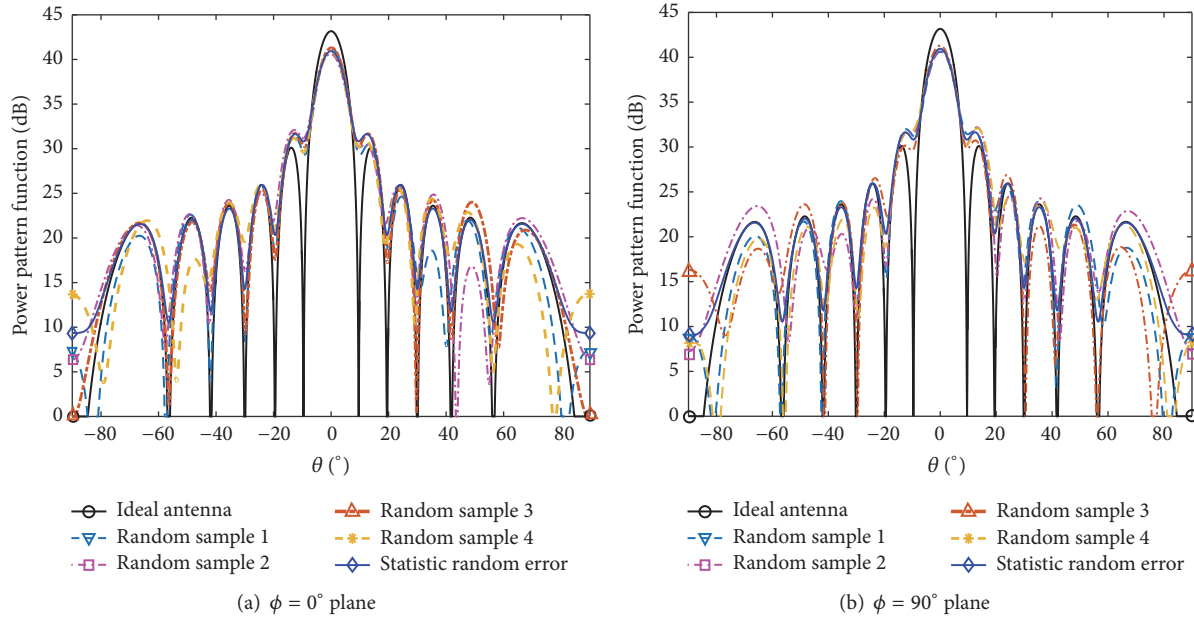


FIGURE 5: Performance with systematic distortion and random error.

from the different random error distribution. So it is more precise to extract from the statistic performance than from the performance calculated by adding a random sample with systematic distortion.

In addition, the performance obtained from the presented statistic model is further verified especially on the sidelobe level and boresight pointing. Firstly the above four random samples are increased to one thousand samples with the same normal distribution. Next the mean of power pattern function is calculated by averaging the sum of performances obtained from all the samples. After one thousand times of calculations for all the samples, the average gain loss is -2.23 dB, which is the same value from the statistic model. The first sidelobe levels increase by 0.52 dB and 1.54 dB in $\phi = 0^\circ$ and $\phi = 90^\circ$ planes, respectively. The absolute errors are only 0.01 dB in both the two planes. The beam width changes by 0.29° and 0.34° , respectively, and the boresight pointing varies by 0.28° and 0.19° , respectively, which are almost the same values as obtained from the presented static model.

Therefore, the presented coupled structure-electromagnetic statistic model can evaluate the antenna performance quickly and effectively with the effect of randomness in element position.

5. Conclusion

Aimed at the restrictions of creating effective performance under the effect of randomness in the position of the array element, a coupled structural-electromagnetic statistic model for active phased array antenna is presented. The effect of randomness in element position on antenna performance is analyzed, compared with the electrical parameters obtained from the random sample errors combined with systematic distortion. The results show that random errors lead to the randomness of electromechanical performance of antenna,

especially on the sidelobe levels compared to the gain and the beam width. The electrical parameters obtained from the statistic model are more accurate than from any random sample errors. The performance got from the statistic model is almost the same with the average of the sum of performances from a large amount of random samples. Thus the presented method can evaluate the antenna performance quickly and effectively. It provides an advantageous guidance for structural design and performance optimization for array antennas in wireless application. In addition, it can effectively reduce the repeated design time of antennas to achieve the objective of lower development cost and time.

Conflicts of Interest

The authors declare that there are no conflicts of interest regarding the publication of this paper.

Acknowledgments

This work was supported by the National Natural Science Foundation of China under Grant nos. 51522507 and 51475349, the National 973 Program under Grant no. 2015CB857100, Youth Science and Technology Star Project of Shaanxi Province under Grant no. 2016KJXX-06, and the Fundamental Research Funds for the Central Universities under Grant nos. JBG150409, KJXX1603, and 7214479606.

References

- [1] K. Yelamarthi, M. S. Aman, and A. Abdelgawad, "An application-driven modular IoT architecture," *Wireless Communications and Mobile Computing*, vol. 2017, Article ID 1350929, 16 pages, 2017.
- [2] G. Vlasyuk, O. Starkova, K. Herasymenko, Y. Kravchenko, and A. Polianytsia, "Implementation of the Internet of things

- concept for remote power management,” in *Proceedings of the 2nd International Conference on Advanced Information and Communication Technologies, AICT 2017*, pp. 26–30, Ukraine, July 2017.
- [3] A. Abdelgawad and K. Yelamarthi, “Internet of things (IoT) platform for structure health monitoring,” *Wireless Communications and Mobile Computing*, vol. 2017, Article ID 6560797, 2017.
 - [4] R. L. Sturdivant and E. K. P. Chong, “Systems Engineering of a Terabit Elliptic Orbit Satellite and Phased Array Ground Station for IoT Connectivity and Consumer Internet Access,” *IEEE Access*, vol. 4, pp. 9941–9957, 2016.
 - [5] J. Laskar, S. Pinel, S. Sarkar et al., “On the development of CMOS mm W and sub-THz phased array technology for communication/sensing nodes,” in *Proceedings of the 2010 IEEE MTT-S International Microwave Symposium, MTT 2010*, pp. 1312–1315, USA, May 2010.
 - [6] Z.-Y. Zhang, S. Li, S.-L. Zuo, J.-Y. Zhao, X.-D. Yang, and G. Fu, “Dual-polarized crossed bowtie dipole array for wireless communication applications,” *International Journal of Antennas and Propagation*, vol. 2014, Article ID 349516, 8 pages, 2014.
 - [7] G. Li, B. Ai, D. He, Z. Zhong, B. Hui, and J. Kim, “On the feasibility of high speed railway mmWave channels in tunnel scenario,” *Wireless Communications and Mobile Computing*, vol. 2017, 17 pages, 2017.
 - [8] T. Takahashi, N. Nakamoto, M. Ohtsuka et al., “On-board calibration methods for mechanical distortions of satellite phased array antennas,” *IEEE Transactions on Antennas and Propagation*, vol. 60, no. 3, pp. 1362–1372, 2012.
 - [9] H. Kamoda, J. Tsumochi, T. Kuki, and F. Suginoshta, “A study on antenna gain degradation due to digital phase shifter in phased array antennas,” *Microwave and Optical Technology Letters*, vol. 53, no. 8, pp. 1743–1746, 2011.
 - [10] C. Wang, Y. Wang, W. Wang, J. Zhou, M. Wang, and Z. Wang, “Electromechanical coupling based influence of structural error on radiation and scattering performance of array antennas,” *IEEE Electronics Letters*, vol. 53, no. 14, pp. 904–906, 2017.
 - [11] A. Canclini, F. Antonacci, A. Sarti, and S. Tubaro, “Distributed 3D Source Localization from 2D DOA Measurements Using Multiple Linear Arrays,” *Wireless Communications and Mobile Computing*, vol. 2017, 11 pages, 2017.
 - [12] C. Wang, M. Kang, W. Wang et al., “Electromechanical coupling based performance evaluation of distorted phased array antennas with random position errors,” *International Journal of Applied Electromagnetics and Mechanics*, vol. 51, no. 3, pp. 285–295, 2016.
 - [13] A. Ossowska, J. H. Kim, and W. Wiesbeck, “Influence of mechanical antenna distortions on the performance of the HRWS SAR system,” in *Proceedings of the 2007 IEEE International Geoscience and Remote Sensing Symposium, IGARSS 2007*, pp. 2152–2155, Spain, June 2007.
 - [14] E. Zaitsev and J. Hoffman, “Phased array flatness effects on antenna system performance,” in *Proceedings of the 4th IEEE International Symposium on Phased Array Systems and Technology, Array 2010*, pp. 121–125, Waltham, Mass, USA, 2010.
 - [15] C. Wang, M. Kang, Y. Wang, W. Wang, and J. Du, “Coupled structural-electromagnetic modeling and analysis of hexagonal active phased array antennas with random errors,” *AEÜ - International Journal of Electronics and Communications*, vol. 70, no. 5, pp. 592–598, 2016.
 - [16] M. Lange, “Impact of statistical errors on active phased-array antenna performance,” in *Proceedings of the Military Communications Conference, MILCOM 2007*, USA, October 2007.
 - [17] S. W. Schediwy, D. Price, F. Dulwich, and B. Mort, “A quantitative analysis of how phase errors affect the beam quality of phased arrays,” in *Proceedings of the 4th IEEE International Symposium on Phased Array Systems and Technology, Array 2010*, pp. 256–260, USA, October 2010.
 - [18] M. Lanne, “Design aspects and pattern prediction for phased arrays with subarray position errors,” in *Proceedings of the 4th IEEE International Symposium on Phased Array Systems and Technology, Array 2010*, pp. 440–446, Waltham, MA, USA, October 2010.
 - [19] C. Wang, M. Kang, W. Wang, B. Duan, L. Lin, and L. Ping, “On the performance of array antennas with mechanical distortion errors considering element numbers,” *International Journal of Electronics*, vol. 104, no. 3, pp. 462–484, 2017.
 - [20] M. K. Kang, Y. Wang, L. Yin et al., “Performance prediction for array antennas with element position error based on coupled structural-electromagnetic model,” in *Proceedings of the fifth Asia International Symposium on Mechatronics*, pp. 34–38, Guilin, China, 2015.
 - [21] C. S. Wang, B. Y. Duan, F. S. Zhang et al., “Coupled structural-electromagnetic-thermal modelling and analysis of active phased array antennas,” *IET Microwaves, Antennas & Propagation*, vol. 4, no. 2, pp. 247–257, 2010.
 - [22] J. Ruze, “The effect of aperture errors on the antenna radiation pattern,” *Il Nuovo Cimento*, vol. 9, no. 3, pp. 364–380, 1952.
 - [23] D. J. Goodman and A. J. Viterbi, *Wireless Personal Communications*, Wesley, Addison Longman Incorporated, 1997.
 - [24] Z. Cendes, “The development of HFSS,” in *Proceedings of the 2016 USNC-URSI Radio Science Meeting (Joint with AP-S Symposium), USNC-URSI 2016*, pp. 39–40, Puerto Rico, July 2016.
 - [25] W. Roh, J.-Y. Seol, J. Park et al., “Millimeter-wave beamforming as an enabling technology for 5G cellular communications: theoretical feasibility and prototype results,” *IEEE Communications Magazine*, vol. 52, no. 2, pp. 106–113, 2014.

Research Article

Position Tolerance Design Method for Array Antenna in Internet of Things

Congsi Wang ^{1,2}, Shuai Yuan ¹, Xiaodong Yang ³, Wei Gao,² Cheng Zhu,⁴
Zhihai Wang,⁵ Shaoxi Wang ⁶, and Xuelin Peng⁷

¹Key Laboratory of Electronic Equipment Structure Design, Ministry of Education, Xidian University, Xi'an 710071, China

²School of Civil and Environmental Engineering, University of New South Wales, Sydney, NSW 2052, Australia

³School of Electronic Engineering, Xidian University, Xi'an 710071, China

⁴National Key Laboratory of Antennas and Microwave Technology, Xidian University, Xi'an 710071, China

⁵CETC No. 38 Research Institute, Hefei 230088, China

⁶School of Software and Microelectronics, Northwestern Polytechnical University, Xi'an 710072, China

⁷Nanjing Research Institute of Electronics Technology, Nanjing 210039, China

Correspondence should be addressed to Shuai Yuan; xduyuanshuai@126.com

Received 27 October 2017; Accepted 4 January 2018; Published 12 February 2018

Academic Editor: Farooq A. Tahir

Copyright © 2018 Congsi Wang et al. This is an open access article distributed under the Creative Commons Attribution License, which permits unrestricted use, distribution, and reproduction in any medium, provided the original work is properly cited.

The position error of array antenna significantly deteriorates the gain and sidelobe of the array, which seriously hinders the realization of high performance of communication antenna for Internet of Things (IoT). Based on the sensitivity analysis theory, the sensitivity of the array radiation field with respect to the position of the antenna element is derived. Besides, a novel design method of position tolerance for array antenna is proposed and applied to a 20×20 planar array. Compared with the array designed by traditional method, the gain loss is basically the same (being 0.5 dB), while the peak sidelobe level is lowered by 1.937 dB ($\varphi = 0^\circ$)/1.586 dB ($\varphi = 90^\circ$). Besides, the uncertainty analysis results show that the newly designed array has a much higher chance to achieve the desired performance, which fully demonstrates the innovation and effectiveness of the new method.

1. Introduction

The Internet of Things (IoT) has received considerable attention in many areas like smart cities [1], health care [2], and so on [3–6]. The array antenna is a key component to acquire the target information in the Internet of Things [7]. In the complicated electromagnetic jamming condition caused by a large number of other objects, the high gain and low sidelobe of array antenna are crucial parameters for the accurate acquisition of the targets' state [8, 9]. However, affected by the fabrication accuracy and temperature load, the actual position of array element is inevitably deviated from its nominal position, resulting in a significant decrease in the gain and a severe increase in the side lobes [10–16]. This paper focusses on the design method of the position tolerance of antenna element.

There have been a large number of studies focusing on the tolerance design of antenna element. The tolerance of the amplitude and phase error of the excitation is first studied. Ruze [17] first studied the effect of random amplitude and phase error on the mean value of gain and sidelobe level (SLL) from the statistical point of view. Hsiao [18] made a further step and studied the effect of random amplitude error on the peak sidelobe level (PSLL). Besides, the interval method is adopted to analyze the effect of random amplitude/phase error whose probability distribution is unknown [19, 20]. Besides, with the development of the studies on the position tolerance of amplitude and phase error, the tolerance of the position error of antenna element also receives a lot of attention. Bailin and Ehrlich [21] studied the effect of errors in slot lengths and position on the performance of the slot array. Wang [22] deduced the relationship between

the position tolerance of antenna element and the gain loss of the array. Elliott [23] proposed the method to design the position tolerance according to the allowable PSLI increase. Lanne [24] studied the influence of the position error tolerance of subarray. Besides, the effect of random and deterministic position error on the performance of the array is also analyzed [25, 26]. One thing in common with these tolerance design methods is that in order to meet the requirements of array performance, the tolerance of all elements should be less than the same standard, called the “traditional method” in this paper. However, it is obvious from the qualitative theoretical analysis that the influence of an array element on the electrical performance of array varies from others. If the tolerance of array elements which have larger influence is strictly controlled and that of the array elements which have small influence is reasonably increased, then the performance of the array should be more easier to be satisfied than the “traditional method.” Therefore, in order to provide the position tolerance design method of antenna element, how to assess the influence of the position of antenna element on the array performance becomes a crucial problem, which is not yet seen in the public literature.

In this paper, the sensitivity of the main lobe of the array radiation field to the position of antenna element is taken as the parameter to evaluate the influence of the gain on the position of the array, and the corresponding computational model is derived. Besides, the position tolerance of a 20×20 planar array is designed based on the positional sensitivity. The results show that compared with the array designed by the “traditional method” the gain loss of the newly designed array is basically the same as the “traditional” one, whereas the PSLI is much lower, which proves the validity and innovation of the new method.

2. Mathematical Derivation of the Sensitivity Model

The sensitivity analysis can be used to evaluate the influence of independent variables on dependent variable [27] and has been widely used in various fields [28–30], but its application in array antenna design is not found in the public literature. Therefore, it is necessary to derive the sensitivity of the array radiation field to the element position. For a planar array as is shown in Figure 1, the radiation field is E as follows:

$$E = \sum_{m=0}^{M-1} \sum_{n=0}^{N-1} I_{mn} \cdot \exp \left[jk (md_x \mu + nd_y \nu + z_{mn} \omega) \right]. \quad (1)$$

The sensitivity S_{mn} of the array radiation field E to the position of the antenna element (m, n) is in fact calculated by the partial derivative. The greater the modulus of the partial derivative, the higher the position sensitivity of the element (m, n) , so the position tolerance of the element should be smaller. Besides, it is obvious that (1) satisfies the conditions of derivable function [31]. In addition, it has been proved that compared to the position error in x, y direction the position error in z direction causes a much larger gain loss and sidelobe level [26]. Therefore, the sensitivity of the array radiation field to the position error in z direction is

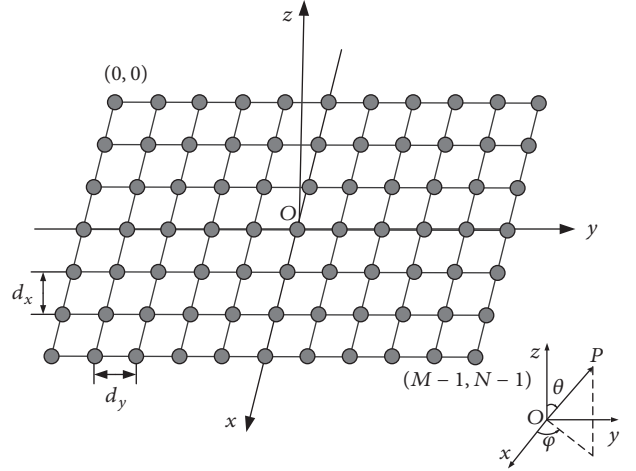


FIGURE 1: Spatial geometric distribution of array antennas.

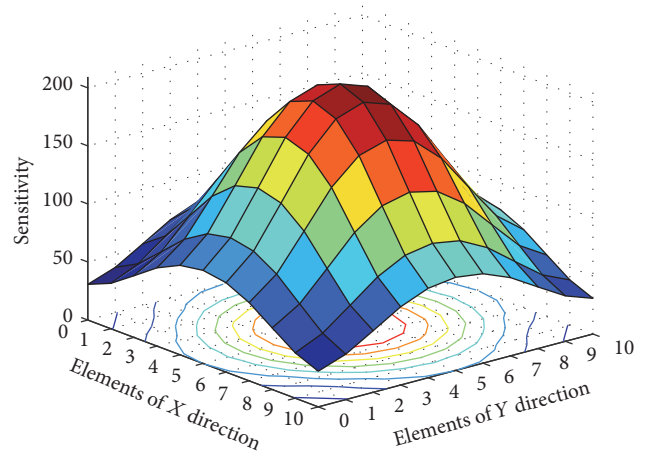


FIGURE 2: Position sensitivity distribution of array elements.

TABLE 1: Parameters of the array.

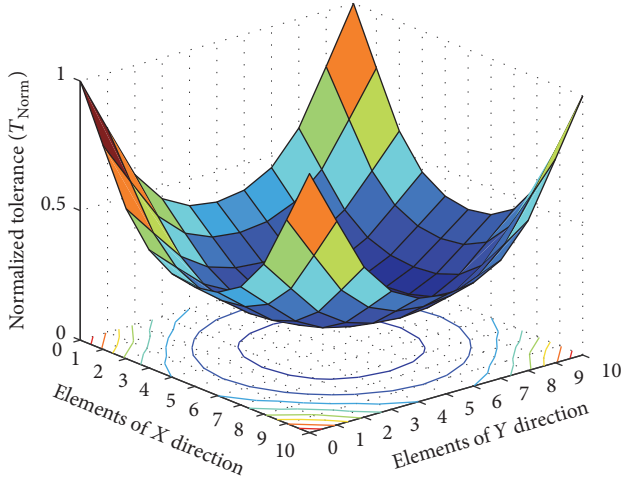
M	N	Freq	d_x	d_y	Weight
11	11	10 GHz	0.65λ	0.65λ	Taylor (-25 dB)

analyzed in this paper, and the result can be easily extended to the analysis of positions in x, y direction. The S_{mn} can be calculated by the following equation:

$$\begin{aligned} S_{mn} &= \frac{\partial E}{\partial z_{mn}} \\ &= jk\omega \cdot I_{mn} \exp \left[jk (md_x \mu + nd_y \nu + z_{mn} \omega) \right]. \end{aligned} \quad (2)$$

Taking a 11×11 planar array as an example, the sensitivity S_{mn} is calculated and is shown in Figure 2. The structural and electrical parameters of the array are shown in Table 1.

It can be seen from Figure 2 that the highest position sensitivity is located in the central region of the array, and the lowest is located in the edge region. Based on the previous analysis, in order to meet the performance requirements, the


 FIGURE 3: Normalized position tolerance distribution T_{norm} .

higher the position sensitivity is, the smaller the position tolerance should be. Therefore, it is assumed that the position tolerance of each antenna element is positively linearly correlated to the reciprocal of the corresponding sensitivity. Here T_{norm} is defined as the normalized position tolerance distribution and calculated as follows:

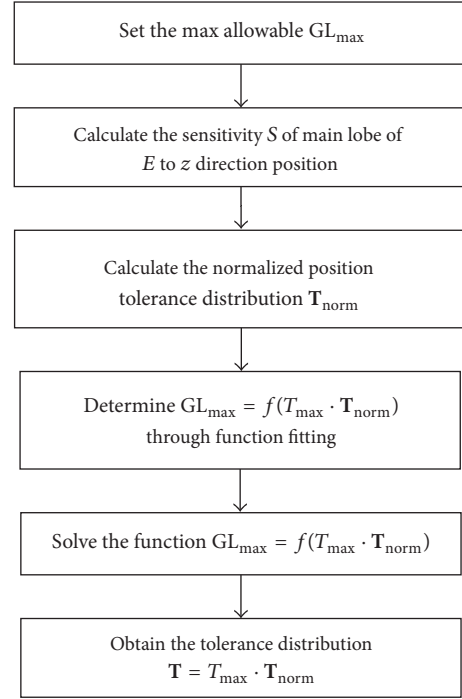
$$T_{\text{norm}}^{mn} = \frac{(1/S_{mn})}{\max(1/S_{ij})} \quad (3)$$

$$(i = 0, 1, \dots, M-1; j = 0, 1, \dots, N-1).$$

In this case, the normalized position tolerance distribution T_{norm} is shown in Figure 3. Then the position tolerance distribution of the array can be written as $\mathbf{T} = T_{\text{max}} \cdot \mathbf{T}_{\text{norm}}$, where T_{max} is the maximum position tolerance of all the array elements. Suppose the acceptable gain loss caused by the random position error is GL_{max} , then how to determine T_{max} according to GL_{max} becomes a critical issue, which is studied in the next section.

3. Position Tolerance Design Method and Verification

3.1. Process for Position Tolerance Design. The very first point that needs to be noted here is that the position tolerance T_{max} is a definite value, whereas the position error of antenna element is randomly distributed within the tolerance zone \mathbf{T} , so the gain loss of the array under \mathbf{T} is uncertain, too. In order to quantitatively evaluate the gain loss caused by the position errors that submitted to T , the reliable gain loss (R-GL) is defined, which means there is a very small possibility that the gain loss under T is greater than R-GL. Exactly speaking, suppose X groups of position error samples are generated under T and there are X gain losses accordingly. Then R-GL is the smallest gain loss of those that ranks in the top 5% of all gain loss. The definition is also suitable for reliable PSLL (R-PSLL). It is important to note that both R-GL and R-PSLL are directly related to the groups of position


 FIGURE 4: Flow chart for determining the tolerance distribution T .

error samples generated, that is, X . The bigger X , the smaller the variation range of R-GL/R-PSLL. When the variation range of R-GL/R-PSLL is within an acceptable precision, X is acceptable and called the reliable group number X_r .

Meanwhile, it is known from previous studies that there exists a certain functional relation between the reliable gain loss R-GL [15] and the position tolerance distribution T . Suppose $GL_{\text{max}} = 0.5$ dB, then the maximum position tolerance T_{max} can be obtained by directly solving the function $GL_{\text{max}} = f(T_{\text{max}} \cdot \mathbf{T}_{\text{norm}})$. Therefore, in order to obtain T_{max} , it is necessary to find the functional relationship f , which can be carried out through the following steps:

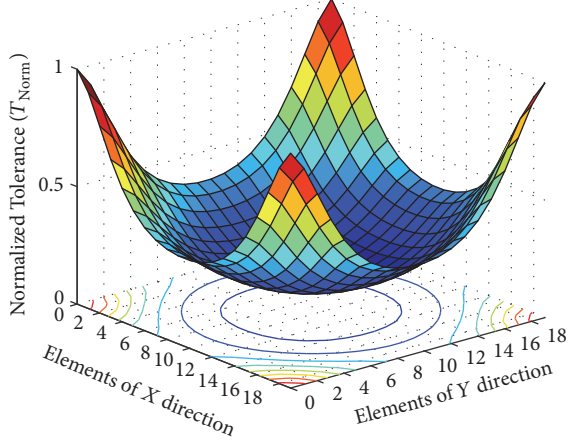
- Calculate the normalized position tolerance distribution T_{norm} through (3).
- Generate a series of tolerances T_{max}^t randomly and calculate RGL_t accordingly.
- Select the fitting function according to the distribution trend of RGL_t relative to T_{max}^t .
- Perform the function fitting in MATLAB to get the function $RGL = f(T_{\text{max}} \cdot \mathbf{T}_{\text{norm}})$.
- Solve the function $GL_{\text{max}} = f(T_{\text{max}} \cdot \mathbf{T}_{\text{norm}})$; then the corresponding maximum position tolerance T_{max} is obtained.

In summary, the position tolerance allocation of array antenna is determined as shown in Figure 4.

3.2. Verification of Design Method. In order to embody the advantage of the position tolerance design method in this paper, it is necessary to compare the electrical performance parameters like gain loss and sidelobe level of array designed by the method proposed in this paper and that of the array designed by the “traditional method.” For the convenience of

TABLE 2: Parameters of the array.

M	N	Freq	d_x	d_y	Weight
20	20	10 GHz	0.65λ	0.65λ	Taylor (-25 dB)

FIGURE 5: Normalized position tolerance distribution T_{norm} .

narration, the previous array is denoted as SA and the latter one as UA.

The following are the verification process and parameter settings. In order to meet the requirements for antielectromagnetic interference capability of most IoT array antennas, a 20×20 planar array is taken as an example to illustrate the comparison. The structural parameters and electrical parameters are shown in Table 2, and the normalized position tolerance distribution T_{norm} is shown in Figure 5. The performance of SA and UA is compared under the same allowable requirements. Specifically speaking, the relationship between the GL and the position tolerance T for SA is obtained through the new method ($GL^S = f(T)$), and the relationship for UA ($GL^U = g(T)$) is obtained from Wang [22] that is frequently cited by relevant researchers. Then suppose the allowable gain loss for SA and UA both is $GL_a^S = GL_a^U = 0.5$ dB. The position tolerance for SA (T_a^S) and UA (T_a^U) is obtained through $GL_a^S = f(T)$ and $GL_a^U = g(T)$, respectively. Finally 10^4 sets of position error samples of antenna element are generated under T_a^S and T_a^U , respectively. The corresponding R-GL and R-PSLL of SA and UA are calculated based on these position error samples. Besides, the uncertainty analysis based on the tolerance distribution of SA and UA is also performed for the comprehensive view of the result. The mean and the standard deviation of the corresponding electrical performance are calculated. What is more, the ratio of the gain loss that is less than 0.5 dB ($GL \leq 0.5$ dB) and the ratio of the $\Delta PSLL$ that is less than 1 dB ($\Delta PSLL \leq 1$ dB) are counted. The reliable group number X_r is obtained through the theory of minimum sample size in mathematics of statistics [32] and numerical simulation. When the variation range of R-GL is 0.05 dB, the reliable group number is $X_r = 100$. Furthermore, the uncertainty of

TABLE 3: Comparison of electrical performance parameters between UA and SA (unit: dB).

	R-GL	R-PSLL ($\varphi = 0^\circ$)	R-PSLL ($\varphi = 90^\circ$)	Tolerance
SA	0.502	-24.442	-24.328	$0.023\lambda \sim 0.163\lambda$
UA (Ref. [22])	0.491	-22.505	-22.742	0.053λ
Difference	-0.011	-1.937	-1.586	/

Here the difference is the parameter of SA minus that of UA.

TABLE 4: Uncertainty analysis of SA and UA under the precondition of equal gain loss.

		Mean	Std.	Ratio
Gain loss	SA	0.433	0.034	97.2%
	UA (Ref. [22])	0.414	0.028	99.8%
PSLL ($\varphi = 0^\circ$)	SA	-25.616	0.697	96.0%
	UA (Ref. [22])	-24.214	0.721	49.5%
PSLL ($\varphi = 90^\circ$)	SA	-25.607	0.6974	95.9%
	UA (Ref. [22])	-24.201	0.721	49.0%

the result is also analyzed. The single run time of the program is 58 minutes and 36 seconds. The results are shown in Tables 3 and 4.

It can be seen from Tables 3 and 4 that for the SA and UA that are designed under the precondition of equal gain loss, the R-PSLL is 1.937 dB ($\varphi = 0^\circ$ plane)/1.586 dB ($\varphi = 90^\circ$ plane) lower than that of UA. Besides, the average PSLL of SA is 1.402 dB ($\varphi = 0^\circ$)/1.406 dB ($\varphi = 90^\circ$) lower than that of UA. What is more, the ratio of $\Delta PSLL \leq 1$ dB of SA is very close to 100% and is almost twice that of UA, which indicates that the position tolerance of SA basically guarantees the requirements for the gain and the PSLL of SA.

Besides, another verification work is done in order to give a comprehensive view of the new method. Suppose the requirement for the array is the allowable increase of the peak sidelobe level $\Delta PSLL_a \leq 1$ dB, then the preset requirement of SA and UA is $\Delta PSLL_a^S = \Delta PSLL_a^U = 1$ dB and the R-GL of SA and UA is compared. Here the way to obtain the relationship $\Delta PSLL = f(T)$ for SA is similar to the way to obtain $GL = f(T)$ that is shown in Figure 4, except that the position tolerance T_a^S is obtained based on the preset requirements for $\Delta PSLL_a$ while the latter is based on the preset requirements for GL. The UA is designed by the method proposed by Elliott [23] who deduced relationship between the PSLL and the position tolerance T_a^U . The reliable group number $X_r = 5000$ when the variation range of $\Delta PSLL$ is 0.1 dB. The result is shown in Tables 5 and 6.

It can be seen from Tables 5 and 6 that the mean PSLL of SA is 0.749 dB ($\varphi = 0^\circ$)/0.726 dB ($\varphi = 90^\circ$) lower than that of UA. Besides, although the R-GL and the mean gain loss are 0.285 dB and 0.252 dB higher than those of UA, respectively, the mean position tolerance of UA (0.025λ) is

TABLE 5: Comparison of electrical performance parameters between UA and SA (unit: dB).

	R-GL	R-PSLL ($\varphi = 0^\circ$)	R-PSLL ($\varphi = 90^\circ$)	Tolerance
SA	0.421	-24.452	-24.436	$0.021\lambda \sim 0.150\lambda$
UA (Ref. [23])	0.136	-24.255	-24.372	0.025λ
Difference	0.285	-0.197	-0.064	/

Here the difference is the parameter of SA minus that of UA.

TABLE 6: Uncertainty analysis of SA and UA under the precondition of equal PSSL.

		Mean	Std.	Ratio
PSSL ($\varphi = 0^\circ$)	SA	-25.609	0.655	96.6%
	UA (Ref. [23])	-24.860	0.474	87.2%
PSSL ($\varphi = 90^\circ$)	SA	-25.607	0.654	96.5%
	UA (Ref. [23])	-24.881	0.477	87.7%
Gain loss	SA	0.441	0.029	97.5%
	UA (Ref. [23])	0.189	0.010	100.0%

much lower than that of SA (0.073λ), which indicates that the small gain loss of UA is achieved by greatly improving the position accuracy of all antenna elements. What is more, it can be seen from Tables 5 and 6 that the gain loss of SA has met the restriction for the requirements of $GL \leq 0.5$ dB. Therefore, the SA designed through the new method is able to realize the desired performance through a more economic way. The above results fully demonstrate the effectiveness and the novelty of the new method proposed in this paper.

4. Conclusion

The high performance of array antenna guarantees the effective communication and accurate acquisition of target information in the Internet of Things. The position tolerance design of array antenna is one of the important research areas. In this paper, the sensitivity model of the array radiation field to antenna element position is derived, and a novel method for array tolerance design is proposed based on the position sensitivity. Compared with the array designed by the "traditional method," the desired electrical performance of the newly designed array can be better achieved through a more economic way, which demonstrated the innovation and effectiveness of the new method. Besides, the sensitivity model can also be used for the theoretical basis of structural strength design. In a word, the study in this paper provides theoretical guidance for the implementation of Internet of Things.

Conflicts of Interest

The authors declare that they have no conflicts of interest.

Acknowledgments

This work was supported by the National Natural Science Foundation of China under Grant nos. 51522507 and 51475349, the National 973 Program under Grant no. 2015CB857100, Youth Science and Technology Star Project of Shaanxi Province under Grant no. 2016KJXX-06, the Fundamental Research Funds for the Central Universities under Grant nos. JBG150409, KJXX1603, and 7214479606.

References

- [1] V. Beltran, A. F. Skarmeta, and P. M. Ruiz, "An ARM-compliant architecture for user privacy in smart cities: SMARTIE-quality by design in the IoT," *Wireless Communications and Mobile Computing*, vol. 2017, Article ID 3859836, 13 pages, 2017.
- [2] D. Wang, H. Liu, X. Ma, J. Wang, Y. Peng, and Y. Wu, "Energy harvesting for internet of things with heterogeneous users," *Wireless Communications and Mobile Computing*, vol. 2017, Article ID 1858532, 15 pages, 2017.
- [3] L. Atzori, A. Iera, and G. Morabito, *The Internet of Things: A survey*, Elsevier North-Holland Inc, 2010.
- [4] S. Andreev, S. Balandin, and Y. Koucheryavy, *Internet of Things, Smart Spaces, and Next Generation Networks and Systems*, Springer, 2015.
- [5] K. Yelamarthi, M. S. Aman, and A. Abdelgawad, "An application-driven modular IoT architecture," *Wireless Communications and Mobile Computing*, vol. 2017, Article ID 1350929, 16 pages, 2017.
- [6] S. F. Fang, L. D. Xu, Y. Q. Zhu et al., "An integrated system for regional environmental monitoring and management based on internet of things," *IEEE Transactions on Industrial Informatics*, vol. 10, no. 2, pp. 1596–1605, 2014.
- [7] V. Mohanan, R. Budiarto, and I. Aldmour, *Powering the Internet of Things with 5G Networks*, IGI Global, 2017.
- [8] W. M. Ibrahim, N. A. Ali, H. S. Hassanein, and A.-E. M. Taha, "Characterizing multi-hop localization for Internet of things," *Wireless Communications and Mobile Computing*, vol. 2016, 16 pages, 2016.
- [9] R. Fan, H. Jiang, S. Wu, and N. Zhang, "Ranging error-tolerable localization in wireless sensor networks with inaccurately positioned anchor nodes," *Wireless Communications Mobile Computing*, vol. 9, 13 pages, 2009.
- [10] J. Bernhard, *Phased Array Antenna Handbook*, Artech House, 1994.
- [11] H. Schippers, G. Spalluto, and G. Vos, "Radiation analysis of conformal phased array antennas on distorted structures," in *Proceedings of the Twelfth International Conference on Antennas and Propagation (ICAP 2003)*, pp. 160–163, 2003.
- [12] C. S. Wang, B. Y. Duan, and Y. Y. Qiu, "On distorted surface analysis and multidisciplinary structural optimization of large reflector antennas," *Structural and Multidisciplinary Optimization*, vol. 33, no. 6, pp. 519–528, 2007.
- [13] J. Zhou, L. Song, J. Huang, and C. Wang, "Performance of structurally integrated antennas subjected to dynamical loads," *International Journal of Applied Electromagnetics and Mechanics*, vol. 48, no. 4, pp. 409–422, 2015.
- [14] C. S. Wang, B. Y. Duan, F. S. Zhang, and M. B. Zhu, "Coupled structural–electromagnetic–thermal modelling and analysis of active phased array antennas," *IET Microwaves, Antennas & Propagation*, vol. 4, no. 2, pp. 247–257, 2010.

- [15] E. Zaitsev and J. Hoffman, "Phased array flatness effects on antenna system performance," in *Proceedings of the 4th IEEE International Symposium on Phased Array Systems and Technology, Array 2010*, pp. 121–125, Waltham, MA, USA, October 2010.
- [16] B. Y. Duan and C. S. Wang, "Reflector antenna distortion analysis using MEFCM," *IEEE Transactions on Antennas and Propagation*, vol. 57, no. 10, pp. 3409–3413, 2009.
- [17] J. Ruze, "The effect of aperture errors on the antenna radiation pattern," *Il Nuovo Cimento*, vol. 9, no. 3, pp. 364–380, 1952.
- [18] J. K. Hsiao, "Array sidelobes, error tolerance, gain, and beamwidth," Tech. Rep. Nrl-8841, Naval Research Lab, Washington, DC, USA, 1984.
- [19] P. Rocca, L. Manica, N. Anselmi, and A. Massa, "Analysis of the pattern tolerances in linear arrays with arbitrary amplitude errors," *IEEE Antennas and Wireless Propagation Letters*, vol. 12, pp. 639–642, 2013.
- [20] L. Poli, P. Rocca, N. Anselmi, and A. Massa, "Dealing With Uncertainties on Phase Weighting of Linear Antenna Arrays by Means of Interval-Based Tolerance Analysis," *IEEE Transactions on Antennas and Propagation*, vol. 63, no. 7, pp. 3229–3234, 2015.
- [21] L. L. B. Bailin and M. J. Ehrlich, "Factors Affecting the Performance of Linear Arrays," *Proceedings of the IRE*, vol. 41, no. 2, pp. 235–241, 1953.
- [22] H. S. C. Wang, "Performance of Phased-Array Antennas with Mechanical Errors," *IEEE Transactions on Aerospace and Electronic Systems*, vol. 28, no. 2, pp. 535–545, 1992.
- [23] R. Elliott, "Mechanical and electrical tolerances for two-dimensional scanning antenna arrays," *IRE Transactions on Antennas Propagation*, vol. 6, no. 1, pp. 114–120, 1958.
- [24] M. Lanne, "Design aspects and pattern prediction for phased arrays with subarray position errors," in *Proceedings of the 4th IEEE International Symposium on Phased Array Systems and Technology, Array 2010*, pp. 440–446, Waltham, MA, USA, October 2010.
- [25] C. Wang, M. Kang, W. Wang et al., "Electromechanical coupling based performance evaluation of distorted phased array antennas with random position errors," *International Journal of Applied Electromagnetics and Mechanics*, vol. 51, no. 3, pp. 285–295, 2016.
- [26] C. Wang, M. Kang, W. Wang, B. Duan, L. Lin, and L. Ping, "On the performance of array antennas with mechanical distortion errors considering element numbers," *International Journal of Electronics*, vol. 104, no. 3, pp. 462–484, 2017.
- [27] A. Saltelli, *Global Sensitivity Analysis: The Primer*, 2008.
- [28] R. Levine and D. Renelt, "A sensitivity analysis of cross-country growth regressions," *American Economic Review*, vol. 82, no. 4, pp. 942–963, 1992.
- [29] V. Komkov, K. C. Kyung, and J. H. Edward, *Design Sensitivity Analysis of Structural Systems*, vol. 177, Academic press, 1986.
- [30] S. Zhang, B. Duan, H. Bao, and P. Lian, "Sensitivity analysis of reflector antennas and its application on shaped geo-truss unfurlable antennas," *IEEE Transactions on Antennas and Propagation*, vol. 61, no. 11, pp. 5402–5407, 2013.
- [31] G. F. Carrier, M. Krook, and C. E. Pearson, "Functions of a complex variable - theory and technique," *American Mathematical Monthly*, vol. 2, pp. 221–222, 2005.
- [32] J. F. Kenney, *Mathematics of Statistics*, New Delhi, India, D. Van Nostrand Company Inc, London, UK; Affiliated East-West Press Pvt-Ltd, 2013.